

Effects of Prepulse Radiation on Non-Thermal
(> 10 Kev/Z) Ions in Laser Produced Plasmas

Sanwal Prasad Sarraf
Ph.D. Thesis

Lab Report 197
May 1980

EFFECTS OF PREPULSE RADIATION ON
NON-THERMAL ($> 10 \text{ Kev/Z}$) IONS IN
LASER PRODUCED PLASMAS

by

Sanwal Prasad Sarraf

Submitted in Partial Fulfillment
of the
Requirements for the Degree
Doctor of Philosophy

Supervised by Professor Leonard M. Goldman

Department of Mechanical and Aerospace Sciences
College of Engineering and Applied Sciences

The University of Rochester
Rochester, New York

1980

VITAE

The author was born in Sabour, India. He graduated from Higher Secondary School, Sabour, India in 1968.

In November 1968, he joined the Bhagalpur College of Engineering, Bhagalpur (India), for the undergraduate study in Mechanical Engineering. He completed the five-year Bachelor of Science course in February 1974. During his undergraduate studies, he also received institute merit scholarship.

Before joining the graduate program in the Department of Mechanical and Aerospace Sciences at the University of Rochester in September 1974, the author was employed by Hindustan Motors Ltd. as an Executive Trainee Engineer from March 1974 to August 1974. The author received his Master of Science degree in May 1975 from University of Rochester. In 1975, he joined the Laboratory for Laser Energetics to continue his graduate study. During his graduate study, the author has been supported by department fellowship and Laboratory for Laser Energetics fellowship. He also held the position of teaching assistant in the Department of Mechanical and Aerospace Sciences for four semesters.

ACKNOWLEDGMENTS

The author is deeply grateful to Professor Leonard M. Goldman for his suggestions and guidance. His advice, encouragement and friendship throughout this endeavor is very much appreciated.

The author is indebted to his fellow graduate student John McAdoo for his valuable support. He would like to thank Messers. Bruce Flaherty and Terry Kessler for their help in the operation of the laser system and, Tom Boehly and Sam Letzring for their support during the experimentation. The author acknowledges useful discussions with Edward Williams, Mike True and Robert Short.

The author is very thankful to John Soures for many useful discussions and support throughout this project.

This project would not have been successful without the support and encouragement from the Director of the Laboratory for Laser Energetics, Professor Moshe J. Lubin. The author has been very fortunate to have conducted the thesis with a very dynamic group at the Laboratory for Laser Energetics.

The author is very grateful to Drs. F. Begay, A. Hauer, E. McCall and other staff members of the Los Alamos Scientific Laboratory for their valuable assistance in making possible the use of their facility for data reduction.

ABSTRACT

A group of non-thermal ions ($> 10 \text{ Kev/z}$) has been studied using a "Thomson Parabola" ion spectrometer. The ions are emitted from a laser produced plasma that is generated by igniting a glass microballoon target with a 50 psec, $1.06 \mu\text{m}$ Nd: glass laser pulse. The effect of prepulse radiation has been investigated, for various prepulse-main pulse timing delays and relative amplitudes. From our measurements of the ion density distribution it seems reasonable to assume an isothermal expansion of the plasma. The hot electron temperature that can then be deduced varies as $(I\lambda^2)^{0.32}$, however x-ray measurements done simultaneously show lower temperatures. "Ion front" (sheath) velocity is found to vary as $(I\lambda^2)^{0.25}$. Large amplitude, high frequency modulations have been observed in the ion density distribution. This feature has been explained using a model based on a two-stream ion-ion instability. Non-thermal ions of energy up to 50 KT_e have been detected. The results have been compared with existing theoretical models.

TABLE OF CONTENTS

VITAE	ii
ACKNOWLEDGMENTS	iii
ABSTRACT	iv
TABLE OF CONTENTS	v
LIST OF TABLES	vii
LIST OF FIGURES	viii
I. INTRODUCTION	1
II. THEORY OF HOT ELECTRONS AND ENERGETIC IONS	7
A. Generation Mechanism of Hot Electrons.....	8
B. Acceleration of Ions by Hot Electrons.....	14
C. Isothermal Expansion of Plasma	17
D. Maximum Expansion Velocity	27
E. Hot Electron Temperature	30
F. Multispecies Plasma Expansion	31
G. Total Number of Energetic Ions	33
H. Prepulse or Structured Pulse Effect	37
III. THEORY OF TWO STREAM ION-ION INSTABILITY IN PLASMA	40
A. Dispersion Relation	41
B. Growth Rates in Homogeneous Expanding Plasma	42
C. Application to Experimental Observation	43
IV. EXPERIMENTAL SYSTEMS AND INSTRUMENTS	59
A. Introduction	59
B. Glass Development Laser and Beta Target Chamber	61

C. Thomson Parabola	67
(a) Introduction	67
(b) Instrument description	76
(c) Resolution	84
(d) Sensitivity	90
(e) Data reduction	91
(f) Problems and Errors	99
V. EXPERIMENTAL RESULTS AND DISCUSSION	103
A. Asymptotic Ion Distribution Function	107
B. Hot Electron Temperature	110
C. Fraction of Target Mass in Energetic Ions	111
D. Fraction of Incident Energy in Energetic Ions	116
E. Maximum Expansion Velocity	120
F. Discussion	120
VI. COMMENTS AND SUMMARY	133
REFERENCES	136
APPENDIX	140
A. FORTRAN Program Used for Data Reduction	140

LIST OF TABLES

Table I. Total number of Target Shots catagorized for the type of Prepulse and Energy(in Joules) on the Target.

Table II. List of Target Shots, Intensity on the Target, derived Hot Electron Temperature, Fraction of the Incident Energy in Ions, Fraction of the Target Mass in Ions, 'Ion Front' velocity(V_T), 'Ion-sound' speed(C_s), and V_T/C_s .

LIST OF FIGURES

- Figure II.1 Geometry of oblique incidence onto a one dimensional density profile. The electric field vector \underline{E} lies in the plane of incidence and the vacuum wave vector makes an angle θ with the density gradient.
- Figure II.2 One dimensional geometry of plasma before expansion.
- Figure II.3 Variation of ion and electron densities at the front during plasma expansion.
- Figure II.4 Normalized electron and ion density versus position in Debye lengths with $\omega_{pi}t$ as a parameter. ω_{pi} is ion plasma frequency and t =time. (Reproduced from Ref. II.26).
- Figure II.5 Normalized ion velocity versus position in Debye lengths with $\omega_{pi}t$ as a parameter. (Reproduced from Ref. II.26).
- Figure III.1 Two stream threshold velocity as a function of Stream densities and Sound Speeds. $\psi = [(\xi-\eta)/(\xi+\eta)]^2$ and $\phi = \frac{V_{\text{THRESHOLD}}}{2\sqrt{\xi + \eta}}$
- Figure III.2 Growth rate versus relative velocity with density ratio of Species as parameter.

Figures (continued)

- Figure III.3 Asymptotic ion density distribution versus velocity measured by 'Thomson Parabola' ion analyser.
- Figure III.4 Density distribution of heavy ion Species (O^{+8} , O^{+7} etc.) mixture as a function of τ .
- Figure III.5 Density distribution of heavy-light ion species (O^{+8} , H^+ etc.) mixture as a function of τ .
- Figure III.6 Total growth 'G' of the wave packet as a function of τ for O^{+8} , O^{+7} and O^{+8} , H^+ ion mixture.
- Figure III.7 Normalized growth rate as a function of τ for O^{+8} , O^{+7} and O^{+8} , H^+ ion mixture.
- Figure III.8 Total growth 'G' of wave packet originating at different positions ($\tau_{initial}$) on stream density profile.
- Figure III.9 $K\lambda_D$ as a function of τ , for O^{+8} , O^{+7} and O^{+8} , H^+ ion mixture.
- Figure III.10 Net growth rate (after Landau damping) versus $K\lambda_D$, with T_e/T_i as a parameter.
- Figure IV.1 Schematic layout of the Glass Development Laser (GDL) at the Laboratory for Laser Energetics.

Figures (continued)

- Figure IV.2 Modifications made in the GDL layout to insert the prepulse.
- Figure IV.3 Oscilloscope trace of prepulse and main pulse measured by a photodiode.
- Figure IV.4 Layout of the "Beta" Target Experiment Area.
- Figure IV.5 X-ray photographs obtained from pinhole camera and their densitometer traces.
- Figure IV.6 Photographs obtained from infrared streak camera and their densitometer traces.
- Figure IV.7A Cross-Sectional view of 'Thomson Parabola'.
- Figure IV.7 Schematic diagram of 'Thomson Parabola'.
- Figure IV.8 Schematic view of 'Thomson Parabola'.
- Figure IV.9 Schematic view of 'Thomson Parabola'.
- Figure IV.10 Sketch of film plane of 'Thomson Parabola' with ion trajectory on it.
- Figure IV.11 Film showing raw data obtained from 'Thomson Parabola' instrument.

Figures (continued)

- Figure IV.12 Field of measurement obtained from "Omnicon Pattern Analyzer".
- Figure IV.13 Calibration of the field of measurement, Omnicon pattern analyser.
- Figure IV.14 Asymptotic ion density distribution versus velocity measured by 'Thomson Parabola' ion analyser.
- Figure V.1A Positions of charge collectors in the target chamber.
- Figure V.1B A typical oscilloscope trace of charge collector signal.
- Figure V.2 Asymptotic ion density distribution versus velocity measured by 'Thomson Parabola' ion analyser.
- Figure V.3 Hot electron temperature (T_{hot}) versus laser intensity (I) on the target (no prepulse case).
- Figure V.4 Hot electron temperature (T_{hot}) versus laser intensity (I) on the target (for prepulse case). Numerals next to data point indicate \log_{10} of prepulse to main pulse ratio.
- Figure V.5 Normalized hot electron temperature versus prepulse to main pulse to main pulse amplitude ratio. 10^{-7} is defined as no prepulse on the target.

Figures (continued)

- Figure V.6 Fraction of target mass in fast ions versus laser energy incident on the target. Numerals next to data point indicate \log_{10} of prepulse to main pulse ratio.
- Figure V.7 Fraction of target mass in fast ions versus prepulse to main pulse amplitude ratio (contrast ratio). 10^{-7} is defined as no prepulse on the target.
- Figure V.8 Fraction of incident energy in energetic ions versus laser intensity incident on the target. Numerals next data point indicate \log_{10} of prepulse to main pulse amplitude ratio.
- Figure V.9 Fraction of incident laser energy in fast ions versus prepulse to main pulse amplitude ratio. 10^{-7} is defined as no prepulse on the target.
- Figure V.10A 'Ion Front' velocity (V_T) versus laser intensity (I) on the target (no prepulse case).
- Figure V.10B 'Ion Front' velocity (V_T) versus laser intensity (I) on the target, (prepulse case). Numerals next to data point indicate \log_{10} of prepulse to main pulse amplitude ratio.
- Figure V.11 Ratio of 'ion front' velocity (V_T) to 'ion sound' speed (C_s) versus laser intensity II) on the target. Numerals next to data point indicate \log_{10} of prepulse to main pulse amplitude ratio.

Figures (continued)

- Figure V.12 Plot of absorption, resonant absorption, specular reflection and backscatter as a function of irradiance for short pulse Nd: Laser plasma. (Reproduced from Ref. V.8.)
- Figure V.13 Plot of absorption, resonant absorption and backscatter as a function of irradiance for a double structured pulse Nd: laser plasma. (Reproduced from Ref. V.8.)
- Figure V.14 Plot of absorption, resonant absorption, specular reflection and backscatter as a function of inner gradient scale length for a double structure Nd: laser produced plasma at irradiance $3 \times 10^{15} \text{ W/cm}^2$. (Reproduced from Ref. V.8.)

I. INTRODUCTION

The primary goal of the Laser Fusion Feasibility Program is to produce net energy yield from the thermonuclear reactions that are initiated in small pellets of thermonuclear fuel irradiated with intense laser beams. The interaction between the laser pulse and the target pellet has been described elsewhere (1-3) and may be summarized as follows. A fraction of the laser light incident upon the pellet is absorbed in the tenuous, hot, outer region of the plasma, called its "corona", through some combination of absorption mechanisms. This absorbed energy is then conducted inwards to the cooler dense "core" of the pellet via hot electrons from the corona. The heating of the core surface causes its outer layers to be blown off in the manner of a rocket exhaust, and the resulting reaction force drives the unablated portion of the core inwards and thereby compresses it to high density and temperature leading to the thermonuclear burn.

For an efficient ablation driven compression of the fuel, one would ideally desire that the total absorbed energy be shared by the bulk of the ablated mass, called the "thermal ions". This condition gives the maximum recoil momentum, thereby producing the maximum target compression. In practice, with 1.06 μm radiation the situation is far from this. Copious production of ions having supra-thermal velocities has been observed in a variety of laser-target interaction experiments. These non-thermal ions (also called energetic ions, fast ions etc.) usually comprise less than one percent of the total target mass, but can account for about half the total

absorbed energy.¹ For the present work we define non-thermal ions as those which have energies $>10 \text{ Kev/z}$.

It is not very difficult to understand why the role played by non-thermal ions in laser fusion experiments is an undesirable one. For example, in these experiments most of the absorbed energy is converted into the ion kinetic energy (E_i) of expansion, with the associated momentum transfer to the pellet being given by $2E_i/v$. For a fixed amount of laser energy and, therefore fixed E_i , the momentum transfer is increased as the velocity is lowered and the ablated mass increased. On the other hand, higher velocity associated with small ablated mass significantly reduces the recoil momentum available for an efficient pellet impulsion. Since there is no known effective use for these high energy ions, the current interest in the inertial fusion community is to minimize their production. Ideally, one would like them to be totally absent. This demands an extensive knowledge of the mechanism of their generation. Fast ions are produced by hot electrons. These electrons have energies much higher than the ion thermal energy and have temperatures of tens of Kev. Therefore, the production of energetic ions is closely related to the absorption and transport of the laser energy.

Many competitive absorption mechanisms have been suggested (Chapter II), but resonant absorption is believed to be the principal absorption mechanism in short pulse ($\sim 50 \text{ psec}$), high intensity ($> 10^{14} \text{ w/cm}^2$) experiments. The laser light can stimulate the growth of plasma waves at the critical surface (where plasma frequency equals

laser frequency); the energy in the plasma wave is then coupled to the electrons through Landau damping,⁵ and high energy electrons are generated. These electrons accelerate ions in the electric field generated by the charge separation. A detailed description of this process is given in Chapter II.

Most previous experimental study of non-thermal ions has concentrated on single beam irradiation of planar targets. The physics of the interaction of high power laser light with solid matter is interesting in its own right, but the basic motivation of the research effort in this field is the possibility of initiating a controlled thermonuclear fusion reaction on a laboratory scale. Recently, experiments on spherical targets have used relatively short, fast rising pulses of 30 to 100 psec duration. The thin shell of the target is rapidly heated and explodes, producing multi-kilovolt temperatures in the core. This type of target implosion is described as an "Explosive pusher" implosion. There is little underdense plasma present during the laser pulse. Only low core densities of 0.2 gm/cm^3 (liquid D-T) or less are attained. Moreover, large numbers of very energetic ions are generated.

Therefore, there has been growing interest in using long pulses, of 1 nsec or longer in duration, and structured or shaped pulses that rise gradually from a low intensity to a very high intensity. The purpose of these techniques, which might be used concurrently, is to ablate away the outside of the target without shock heating the fuel core. The fuel is compressed by the reaction force of the ablating plasma. This process is described

as an "Ablative pusher" implosion. These long and structured pulses may produce large amounts of underdense plasma.

The high energy ion production can be considered as an important loss mechanism for the absorbed laser energy because the energy expended in their production is not transported to the ablation surface. However, it should be noted that although high energy ions represent an important energy loss when short duration, high irradiance laser pulses are used, the physics is likely to be different when longer duration, structured pulses that have lower intensities are used. At present there is no generally agreed upon theoretical or numerical model to explain the behavior of non-thermal ions under the variety of plasma density profiles that are produced in experiments. They are instead limited to qualitative prediction of high energy ion behavior because of uncertainties in experimental data and the difficulties in modeling the ion expansion. We have chosen to investigate their behavior experimentally.

The most important result of this work is our measurement of the effect of a variety of plasma density profiles on the behavior of non-thermal ions ($> 10 \text{ Kev/z}$) and on hot electron temperatures. To produce the different plasma density profiles we have used prepulses, pulses that arrive ahead of the main pulse, and have varied the prepulse-main pulse relative amplitude and temporal separation.

Until recently, most experimental observations of non-thermal ions were of an indirect nature, with ion velocity

rather than ion energy being the quantity measured. The diagnostics most commonly used were charge collectors and electrostatic mass spectrometers. As we will see in Chapter IV, inherent problems associated with these devices allow only a low level of confidence in the quantitative evaluation of the data they generate. Both diagnostics measure the ion current intercepting the surface of a conductor placed at a distance far enough from the target so that the ion time of flight is much longer than the initial ion acceleration time. Both measure the asymptotic ion velocity distribution; the latter, however, also resolves the different ion species present in the plasma. The usefulness of these devices is limited at high ion energies ($> 10 \text{ Kev/z}$) because the low ion flux then reduces the sensitivity of the measurements. We chose the "Thomson Parabola" method of ion spectroscopy because of its high dynamic range (> 100), and its ability to analyze simultaneously the energy distribution of high energy ($> 10 \text{ Kev/z}$) ion species having a wide range of charge to mass ratios. Although different detection mediums can be employed with this device (see Chapter IV), we used a solid state track detector (CR-39) because of its ability to register individual ions in form of separate tracks, and because of its high sensitivity. The data generated by the device is very reliable, but the quantitative data reduction is very tedious, because it requires counting of the literally millions of tracks that are registered on the detector in a typical experiment. Others have attempted to obtain the quantitative information from the measurement using less direct methods, but have had little or no

success (see Chapter IV).

Our results support the theory that attributes the production of fast ions to resonantly heated electrons. Our observations indicate an isothermal expansion of the plasma. In the case of short single pulses, the hot electron temperature varies as $(I\lambda^2)^{0.32}$. The "ion front" velocity varies as $(I\lambda^2)^{0.25}$, but the number of non-thermal ions (> 10 Kev/z) generated remains constant in all cases. The energy contained in the non-thermal ions varies between 2.5% and 25% of the energy incident on the target, and increases as the incident energy is increased. With the introduction of prepulse on the other hand, the hot electron temperature, the energy contained in the non-thermal ions and the "ion front" velocity go down. The intensity power laws given above are no longer valid. Interestingly, at the high prepulse-main pulse amplitude ratio of 10^{-2} the hot electron temperature, the energy contained in the fast ions, and the "ion front" velocity become independent of the main pulse intensity. Our observations are consistent with the numerical fluid simulations of Colombant and Manheimer (Ref. 4). Non-thermal ions of energies up to $50 KT_e$ have been detected.

We have observed high frequency, large amplitude modulations in the asymptotic ion density distribution. We have proposed a model based on a two stream ion-ion instability to explain this behavior. The model is reviewed in Chapter III.

In Chapter II, we discuss the important physical processes involved in the generation of non-thermal ions. In Chapter IV, we describe our experimental system and the instruments used.

We present and discuss our results in Chapter V, and compare them with the theoretical models developed in Chapter II. We comment on our results and summarize them in Chapter VI and conclude that chapter with suggestions for future work.

II. THEORY OF HOT ELECTRONS AND ENERGETIC IONS

Production of energetic ions is closely related to the absorption and the transport of laser energy. In laser plasma interactions many competitive absorption mechanisms have been proposed. They include classical inverse bremsstrahlung (collisional) absorption,¹ resonance absorption,² parametric instabilities both near the critical density^{3,4,5} and near one fourth the critical density,⁶ and quasi-resonant coupling on ion-density fluctuations^{1,7} driven by subsidiary process such as two stream oscillatory instabilities in the plasma expansion. On the other hand, there is in general also stimulated scattering of the incident light in the plasma with density less than critical via the Raman and Brillouin instabilities.⁸

It is believed that incident radiation is absorbed through multiple effects. In the high or moderate intensity regime of interest, we believe laser light is absorbed by collisionless (resonant) absorption near critical surface (where plasma frequency equals the laser frequency), into so called hot electrons. These electrons have velocities much higher than the ion thermal velocities and have temperatures in tens of Kev. We assume these electrons to be isothermal during the laser pulse, isothermality is maintained by the high thermal conductivity of the hot electrons coupled with a heat reservoir supplied by the laser. These electrons produce two effects; they transport energy into the target, and they generate fast ion expansion via the ambipolar potential that is setup to keep the electrons from leaving the target. Therefore, the production of hot electrons by laser plasma interaction and the resulting emission of energetic ions

by coronal acceleration are related phenomena.

In this chapter we will first discuss the generation mechanisms of hot electrons. The mechanisms which enable these electrons to accelerate the ions will then be reviewed. Following sections will discuss the isothermal expansion of the plasma. We will end this chapter with an estimation of the total target mass and the fraction of incident energy carried away by these fast ions.

A. Generation Mechanism of Hot Electrons

The principal mechanisms suggested for the generation of hot electrons are (a) pondermotive force,⁹ (b) thermal flux inhibition to less than classical value¹⁰ and (c) resonant absorption, not necessarily in the same order of importance.

Pondermotive force (radiation pressure) is the slowly varying (dc) part of the electromagnetic field that tunnels through to the critical surface. In other words it is a time averaged Lorentz force on a single electron in the electromagnetic field of the incident laser light and is given by¹¹ $[F_{pe} = (-2\pi e^2)/(m_e \omega_0^2) \nabla (|E_0|^2)/8\pi]$. It is transmitted to the ions by the condition of charge neutrality. However, because of the uncertainties in the spatial and temporal distribution of the accelerating force field and the small number of particles involved, it is not clear whether or not the pondermotive force can significantly contribute to the production of energetic ions.¹²

Recently the experimental evidence has been accumulating that the

thermal conduction by the electrons from the critical surface to the core of the target is less than the classical value, i.e., free streaming. This is called flux inhibition. Ion acoustic turbulence has been suggested to be responsible for the electron thermal flux inhibition. The basic idea is very simple. As the hot electrons from the laser deposition region flow into the cool interior of the pellet, cold electrons from the interior of the pellet counter-stream to provide return current for maintaining the charge neutrality. When heat flow increases to the point where the electron drift speed is comparable to the ion-acoustic speed, the growth of ion-acoustic instability can be triggered. This inhibits the further increase of electron drift. The energy conduction speed to the core reduces to the characteristic hydrodynamic speed ($C_s = \sqrt{Z_i kT_e / M_i}$) from electron thermal speed ($v_T \sim \sqrt{kT_e / m_e}$). Calculations show that about two thirds of the electron energy can be lost to the fast ions. Although W. Manheimer (Ref. 13) has shown that by this process flux can be limited to as much as 10^{-2} of its free streaming value, there has been considerable controversy over whether ion-acoustic turbulence can be this effective, particularly for electrons of very high energy. Computer simulations¹⁴ have suggested that ion turbulence does not strongly limit the heat flux, but the issue is not well resolved. Perhaps the most important effect of this turbulence is to impede the cold electron current and bottle up the hot electrons indirectly via self-consistent electric field. Because these processes do not transfer significant amount of energy to electrons, we believe that resonant absorption is the main process responsible for the generation

of hot electrons.

When an electromagnetic wave is obliquely incident on an inhomogeneous plasma and polarized in the plane of incidence, it can be absorbed resonantly by linear mode conversion into an electron plasma wave. This process known as resonant absorption is a collisionless process. The obliquely incident radiation (with respect to density gradient) will penetrate the plasma to the point where it will be refracted back out of the plasma. From this point, the so-called "turning point" (density less than critical), an inward component of the radiation will be evanescent (exponentially damped) and tunnels through to the critical layer ($n = n_{cr}$). The projection of the radiation electric field in the direction of the density gradient n can linearly excite electron plasma waves near the critical density (where plasma frequency equals the laser frequency). The subsequent damping of these large amplitude plasma waves as they propagate towards lower density constitutes an important electron heating mechanism. It is important to note here that the resonant absorption is expected even for target illuminations in which the target surface is normal to the laser beam axis. This is a consequence of the fact that, in focusing the radiation on the target surface with fast optics, some of the rays will be at oblique incidence. In addition, induced scattering,⁸ filamentation,¹⁵ and the rippling of the critical surface,¹⁶ all can result in obliquely incident radiation near the critical surface.

The power converted into the plasma oscillations is determined by the "driver" electric field $E_x = |\underline{B} \times \underline{n}|$ at the resonance point.

Here B is the component of the radiation magnetic field directed out of the plane of incidence. The ratio of the electric field leaked (E_x), to the free space value of the radiation electric field (E_0) depends on angle of incidence and on the density gradient scale length,¹⁷ $L = (d \ln N / dx)^{-1}$.

An excellent coverage of this theory has been given in published literature.^{2,18,17,19} We will not go through the complete mathematical treatment, however we will quote the important equations, assumptions and final solutions relevant to our purpose.

We consider the case of a slab plasma with $n_0 = n_0(x)$, with the electromagnetic wave obliquely incident. The electric field is polarized in the plane of incidence, the x-y plane (Fig. 1). The incident wave vector k is at an angle θ with respect to the unperturbed density gradient. To describe the resonant absorption in plasma, we combine a linearized electron-momentum equation with Maxwell's equations.¹⁹ Ion motion is neglected and fields are assumed to vary as $e^{i(kx - \omega t)}$. Basic fluid and Maxwell's equations are:

$$m_e \frac{\partial v_e}{\partial t} + m_e v_{\text{eff}} \frac{\partial x}{\partial t} = eE - \frac{KT_e}{n_e} \frac{\partial n_e}{\partial x}$$

$$\nabla \cdot \underline{D} = -4\pi\rho$$

$$\nabla \times \underline{E} = -\frac{1}{c} \frac{\partial \underline{B}}{\partial t} \quad (\text{II-1})$$

$$\nabla \times \underline{B} = \frac{4\pi}{c} \underline{J} - \frac{1}{c} \frac{\partial \underline{D}}{\partial t}$$

$$\underline{D} = \underline{E} + 4\pi\underline{P}, \quad \underline{P} = en_e x$$

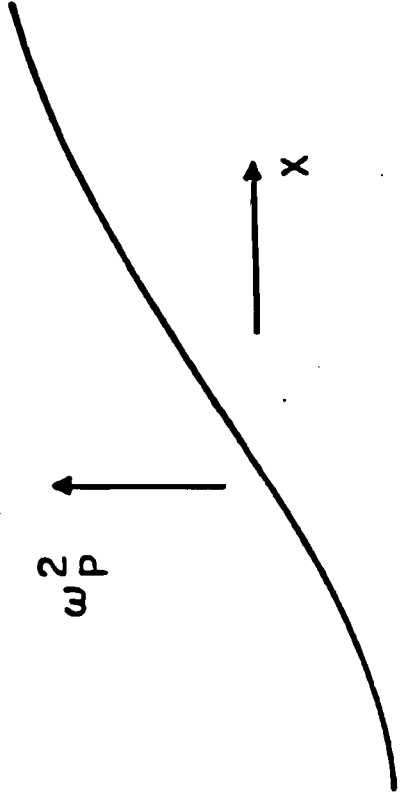
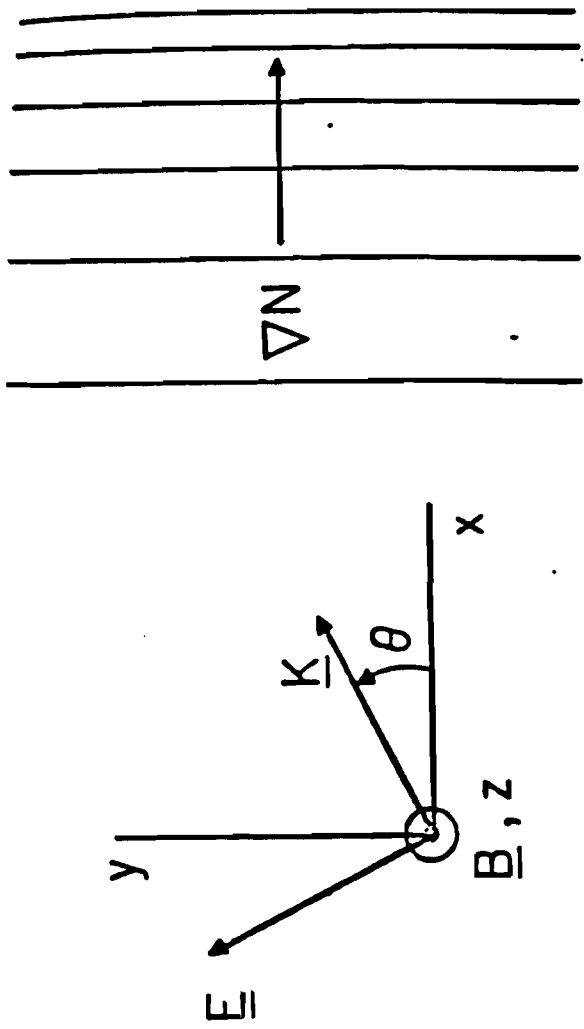


Figure II.1

ν_{eff} = effective electron-ion collision frequency, n_e = background electron density, T_e , m_e and e are electron's temperature, mass and charge respectively, c = velocity of light, and K = Boltzmann's constant.

Employing $\underline{B} = \hat{z}B(x) \text{Exp}\{-i\omega t + ik_y Y\}$ and $\underline{E} = [\hat{x}E_x(x) + \hat{y}E_y(x)] \text{Exp}\{-i\omega t + ik_y Y\}$, taking the unperturbed electron density $n_e(x)$ to be independent of time, the above mentioned equations can be linearized and combined to give

$$\frac{\partial^2 B_z(x)}{\partial x^2} - \frac{1}{\epsilon(x)} \frac{\partial \epsilon}{\partial x} \frac{\partial B_z(x)}{\partial x} + k_0^2 (\epsilon - \sin^2 \theta) B_z(x) = 0 \quad (\text{II-2})$$

where $k_0 = \omega_0/c$ is the free space wave number, with $k_y = k_0 \sin \theta$. $\epsilon(x)$ is the dielectric constant of the plasma with collision frequency ν

$$\epsilon(x) = 1 - \frac{\omega_{pe}^2(x)}{\omega_0^2} \left\{ 1 + \frac{i\nu}{\omega_0} \right\}, \quad \frac{\nu}{\omega_0} \ll 1$$

where $\omega_{pe} = (4\pi n_e e^2/m_e)^{1/2}$ is the electron plasma frequency.

In the collisionless limit, $\nu/\omega_0 \rightarrow 0$, a resonant singularity appears in the second term in equation (2) at the point on the density profile where $\omega_{pe}(x) = \omega_0$ and, therefore, $\epsilon(x) \rightarrow 0$. (By contrast no such resonant singularity appears in the corresponding equation for the light polarized normal to the plane of incidence). In this limit a finite absorption occurs at the singularity. The absorption is caused by the non-zero wave field E_x which tunnels through to the critical point x_c . The equation (2) has been solved in Ref. 20 for $\nu > 0$, $\nu/\omega_0 \rightarrow 0$ and the linear density gradient such that the density rises linearly from

$\omega_{pe}(x) = 0$ at $x = 0$ to $\omega_{pe} = \omega_0$ at $x = L$. The normal component of the electric field vector near the critical surface is represented in the form

$$|E_x| = \frac{\phi(\tau)E_0\sqrt{c}}{\sqrt{2\pi L\omega_0}} \left\{ \left(\frac{x-x_c}{L} \right)^2 + \frac{v^2}{\omega_0^2} \right\}^{-1/2} \quad (\text{II-3})$$

where L is the characteristic distance over which the plasma density changes ($n = n_0[1 - (x-x_c/L)]$), v is the effective electron-collision frequency, E_0 is the amplitude of the electric field in the light beam, and $\phi(\tau)$ is called the resonant absorption function and is defined by $(k_0L)^{2/3} \sin^2\theta$ (which is angle dependent).

B. Acceleration of Ions by Hot Electrons

Plasmas are made of charged particles that move in response to the electromagnetic fields generated either by plasma particles themselves or from external sources. In the case we are going to deal with here, one species of the plasma responds to the electric field produced by another species. The electrons have velocities much higher than ion thermal velocities and tend to separate from cold, stationary ions.

The result is an un-neutralized space charge and an electric field, which retards electrons and accelerates ions. Clearly, for the same electric field, ions with either different charge states or masses will experience different accelerating forces. Plasma then expands under the influence of pressure and electrical forces. The acceleration is most effective at the periphery of the expanding plasma, where the

plasma density is so low that the ions can be accelerated in the electric field essentially without losing the acquired energy in collisions.

An important mechanism which can produce strong electric fields at high irradiance is the plasma pressure. In the presence of density and/or temperature gradients hot electrons try to separate from ions. The electron expansion, however, is limited by the self-consistent electric field created by ion electron separation. To illustrate this, we will assume a two fluid plasma, made of hot electrons and and relatively cold ions. The basic fluid equations are:

$$m_e n_e \frac{d\mathbf{v}_e}{dt} = -en_e (\mathbf{E} + \mathbf{v}_e \times \mathbf{B}) - \nabla p_e + m_e n_e (\nu_{ei} - \nu_{ee}) \mathbf{v}_{ei} \quad (\text{II-4})$$

$$M_i n_i \frac{d\mathbf{v}_i}{dt} = Z_i en_i (\mathbf{E} + \mathbf{v}_i \times \mathbf{B}) - \nabla p_i - m_e n_e (\nu_{ei} - \nu_{ee}) \mathbf{v}_{ei} \quad (\text{II-5})$$

here ν_{ei} is the electron-ion collision frequency, p_e and p_i the electron and ion pressures respectively. All other nomenclatures have standard meaning. We will try to simplify equations (4) and (5). We are looking for long time (longer than electron plasma period) solutions, so electron inertia is neglected. In the absence of the \mathbf{B} field, the terms $(\mathbf{v}_e \times \mathbf{B})$ and $(\mathbf{v}_i \times \mathbf{B})$ drop out. Ions are cold, so their slow density variation enables us to drop the ion pressure term. The collision frequency²¹ is

$$\nu_{ei} = \frac{8\pi e^4 n_i Z_i^2}{M_i^2 (T_e)^{3/2}} \quad (\text{II-6})$$

For high electron temperatures (≈ 10 Kev) the plasma is essentially collisionless,

so collision terms can be neglected. We assume quasineutrality $n_e = \sum_i Z_i n_i$. Incorporating these simplifications, we transform equations (4) and (5) to

$$en_e \underline{E} = - \nabla p_e \quad (\text{II-4A})$$

$$\text{and, } M_i n_i \frac{dv_i}{dt} = Z_i en_i \underline{E} = - \nabla p_e \quad (\text{II-5A})$$

where, $p_e = n_e kT_e$. Now equation (5A) can be written as

$$M_i n_i \frac{dv_i}{dt} = - n_e k \nabla T_e - T_e k \nabla n_e \quad (\text{II-7})$$

From the assumption of isothermality, the first term on the right hand side of equation (7) drops out. Equation (7) suggests that plasma pressure due to the presence of a steep electron density gradient bears the responsibility of imparting accelerating forces on the ions. For the short pulse length (≈ 50 psec) laser commonly used at high irradiance, the density profile is expected to remain relatively steep (less than a few tens of laser wavelengths) during the laser irradiation, due to finite ion expansion velocity. Interferometric measurements^{22,23} of the density profile confirm this notion. At higher laser intensities ($> 10^{14}$ watts/cm²), however, the energy density of the incident radiation can become comparable to the thermal energy of the plasma, so that the radiation pressure can modify and steepen the density profile. It is noteworthy that radiation pressure affects mostly the critical density region so that the density scale length above

critical and below critical can be longer than at critical.

At densities below critical, where plasma expansion can be approximated as freely expanding into vacuum, analytical self similar solutions^{24,25} have been found for the case of an isothermal single specie plasma. In the next section we will briefly review the theory of the isothermal expansion of plasma.

C. Isothermal Expansion of Plasma

In many cases the self-similar isothermal motion of a rarefied plasma gives a good description of plasma expansion. In their pioneering work, Gurevich et al.²⁴ generalised the self-similar solution of an ideal fluid for a plasma expansion. In past years, the model has been extensively studied and was used as a basic model in various works.^{25,26-29}

Moreover, self similar solutions are attractive because they do not contain any characteristic dimensions in the initial and final conditions. The time t and the coordinate x can appear in the solution of such a problem only in the combination x/t . This enables one to simplify the equation considerably and in one dimensional case to obtain analytical solutions.

Plasma is described here by a two fluid model made of hot electrons and relatively cold ions. Later on we will consider the modifications needed to incorporate the more realistic case of a laser plasma, which contains more than one species of electrons (different temperatures) and of ions (different charges and masses). For simplicity, planar geometry and one dimensional expansion is considered; it has been

suggested that the results are not changed greatly in the case of cylindrical or spherical expansion.³⁰

We assume that the plasma at the initial time occupies the half space $x < 0$, and at time $t = 0$ begins to expand into vacuum. The plasma before expansion is illustrated in figure 2. Our assumptions and equations describing the expanding plasma are essentially those of Refs. 25 and 26. Electrons are in thermal equilibrium before the expansion begins. Since the subsequent expansion takes place on a time scale long compared with an electron plasma period [$\tau_p \cong 1/\omega_p = (m_e/4\pi n_e e^2)^{1/2}$], we assume that the electrons are always in equilibrium with the electrostatic potential, i.e., a Boltzmann relation is employed. Each fluid satisfies the continuity and momentum equations. Electron temperature is assumed constant; the validity of this assumption stems from the high electron conductivity coupled to a heat reservoir supplied by the laser. The electron temperature is assumed high enough (\sim tens of Kev) to neglect electron-ion collisions. The ion temperature is assumed high enough to neglect viscosity, but much less than the electron temperature, so that the ion pressure is ignored. The electrostatic potential is described by Poisson's Equation. Thus (for plane geometry) the complete set of equations is

$$\frac{\partial n_i}{\partial t} + \frac{\partial}{\partial x} (n_i v_i) = 0 \quad (A)$$

$$\frac{\partial v_i}{\partial t} + v_i \frac{\partial v_i}{\partial x} = \frac{z_i e}{M_i} E \quad (B)$$

PLASMA BEFORE EXPANSION

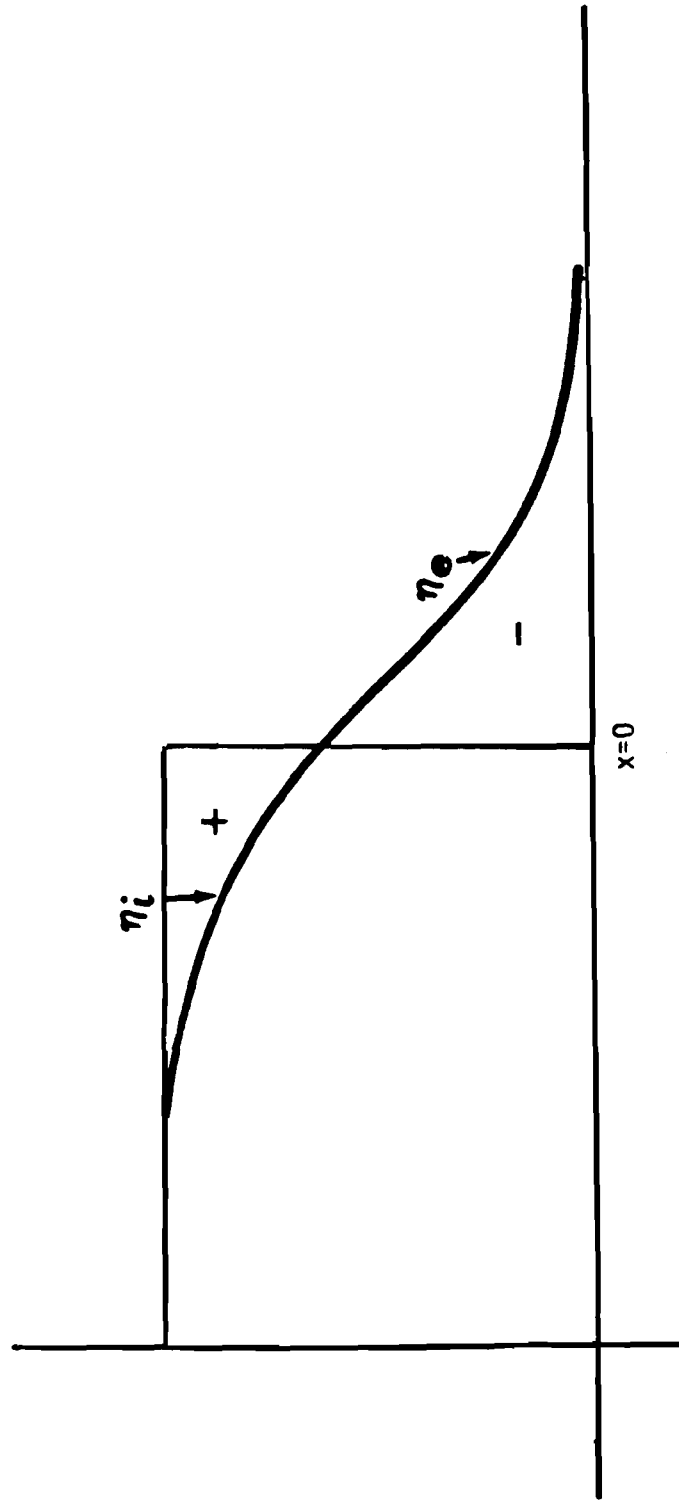


Figure II.2

$$n_e = n_0 \exp \left(\frac{-e\phi}{KT_e} \right) \quad (C)$$

(II-8)

$$\epsilon_0 \frac{\partial^2 \phi}{\partial x^2} = e(n_e - Z_i n_i) \quad (D)$$

Here, v_i = ion velocity, E the electric field, ϕ the potential; and T_e the electron temperature.

Quasineutral approximation

First we consider plasma to be quasineutral, i.e., $n_e = Zn_i$. In fact the plasma is exactly neutral, except at the plasma front where $\text{div } E \neq 0$, and a plasma sheath is formed.

Eliminating E and ϕ from equations (8B) and (8C); using $E = -(\partial\phi/\partial x)$, we have

$$\frac{\partial v_i}{\partial t} + v_i \frac{\partial v_i}{\partial x} = \frac{-Z_i KT_e}{n_e M_i} \frac{\partial n_e}{\partial x} \quad (II-9)$$

Now we will try to develop a similarity solution, in which all dependent variables are functions of $\xi = x/t$ only. Thus,

$$\frac{\partial}{\partial x} = \frac{1}{t} \frac{d}{d\xi} \quad \text{and,} \quad \frac{\partial}{\partial t} = -\frac{\xi}{t} \frac{d}{d\xi}$$

and substitution in (8A) and (9) gives

$$\begin{aligned} (v_i - \xi) \frac{\partial n_i}{\partial \xi} + n_i \frac{\partial v_i}{\partial \xi} &= 0 \\ (v_i - \xi) \frac{\partial v_i}{\partial \xi} &= \frac{-Z_i KT_e}{M_i n_i} \frac{\partial n_i}{\partial \xi} \end{aligned} \quad (II-10)$$

Choosing $C_s^2 = (Z_i K T_e / M_i)$ and eliminating $(\partial n_i / \partial \xi)$ and $(\partial v_i / \partial \xi)$ gives

$$(\xi - v_i)^2 = C_s^2 \quad \text{or,} \quad \cdot \cdot$$

$$\frac{x}{t} - v_i = -C_s \quad \text{(II-11)}$$

Here, the negative root has been chosen (this describes outward expansion). We now want to develop expressions for ion velocity and density. For this, substituting (11) back in (10) we have

$$\frac{\partial v_i}{\partial \xi} = -\frac{C_s}{n_i} \frac{\partial n_i}{\partial \xi}$$

which can be integrated to give

$$v_i = -C_s \ln \left(\frac{n_i}{n_{i0}} \right) \quad \text{(II-12)}$$

Implicit in here is that at unperturbed density, ion velocity is zero, i.e., $v_i = 0$ when $n_i = n_{i0}$. Equation (8C) is used to give

$$\ln \left(\frac{n_i}{n_{i0}} \right) = -\frac{e\phi}{K T_e}$$

therefore,

$$v_i = \left(\frac{e\phi}{K T_e} \right) C_s \quad \text{(II-13)}$$

Also from equation (11), $v_i = \frac{x}{t} + C_s$ (II-13A)

So, $\phi = \frac{1}{C_s} \left(\frac{x}{t} + C_s \right) \frac{K T_e}{e}$ (II-14)

Now, equation (8C) can be used to give

$$n_i = n_{i0} \exp\left\{-\left(\frac{x}{C_s t} + 1\right)\right\} \quad (II-15)$$

The equations formally correspond to the situation in which the ions and the electrons are restricted to the region $x < 0$ and $t = 0$. The infinitely large electric field at the boundary accelerates the boundary ions to infinity as soon as $t > 0$. There is also an electric field at the infinity, since we did not impose any divergence on the electric field, in other words, Poisson's Equation (8D) was not used.

Realistically, we should have allowed for the space charge by employing the Poisson's Equation (8D). The ions which are originally at $x = 0$, will form a well defined "ion front", that moves to the right. Ahead of this front we will always have a pure electron cloud, as shown in figure 3.

Poisson's Equation added

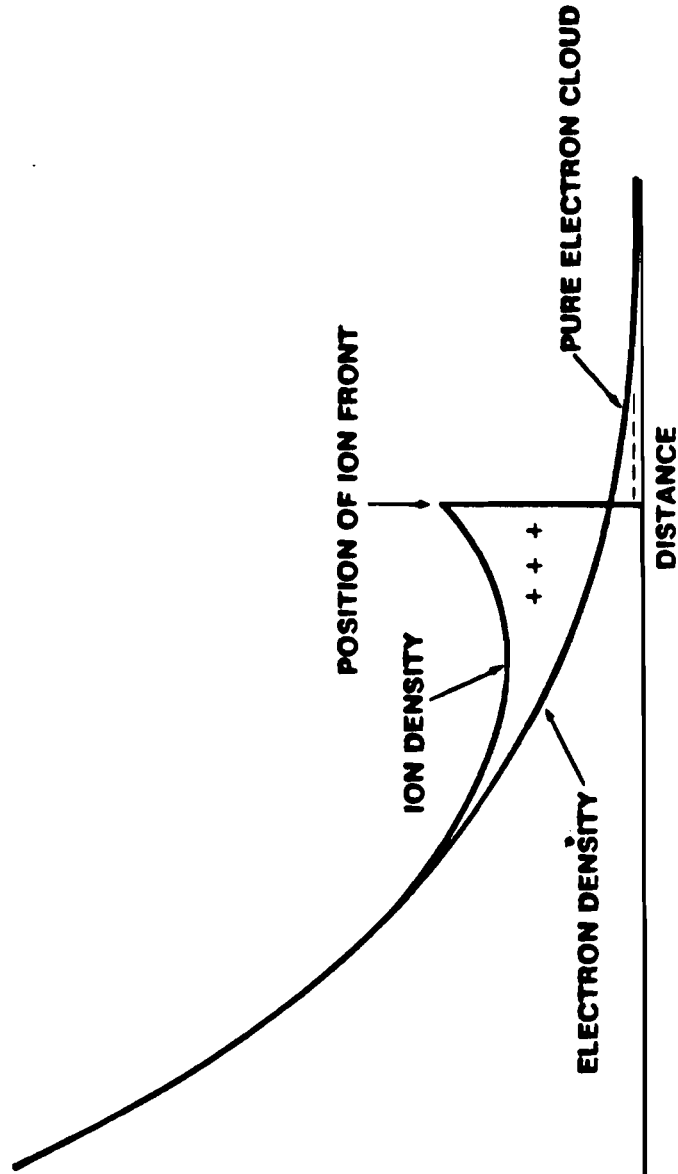
At $t = 0$, Poisson's Equation takes the form

$$\epsilon_0 \frac{d^2 \phi}{dx^2} = n_0 e \left[\exp\left(\frac{e\phi}{KT_e}\right) - 1 \right] \text{ for } x < 0$$

and $\epsilon_0 \frac{d^2 \phi}{dx^2} = n_0 e \exp\left(\frac{e\phi}{KT_e}\right) \text{ for } x > 0$

and 1st integration gives

VARIATION OF ION AND ELECTRON DENSITIES AT THE FRONT



E919

Figure 11.3

$$\frac{1}{2} \epsilon_0 E^2 = n_0 K T_e \left[\exp\left(\frac{e\phi}{K T_e}\right) - 1 - \frac{e\phi}{K T_e} \right] \text{ for } x < 0 \quad (\text{II-16})$$

$$\frac{1}{2} \epsilon_0 E^2 = n_0 K T_e \exp\left(\frac{e\phi}{K T_e}\right) \text{ for } x > 0 \quad (\text{II-17})$$

where $E = -\partial\phi/\partial x$. The boundary conditions employed are $\partial\phi/\partial x = 0$, $\phi = 0$ at $x = -\infty$ and $\partial\phi/\partial x = 0$, $\phi = -\infty$ at $x = +\infty$. The undisturbed plasma is neutral, i.e., the potential is zero.

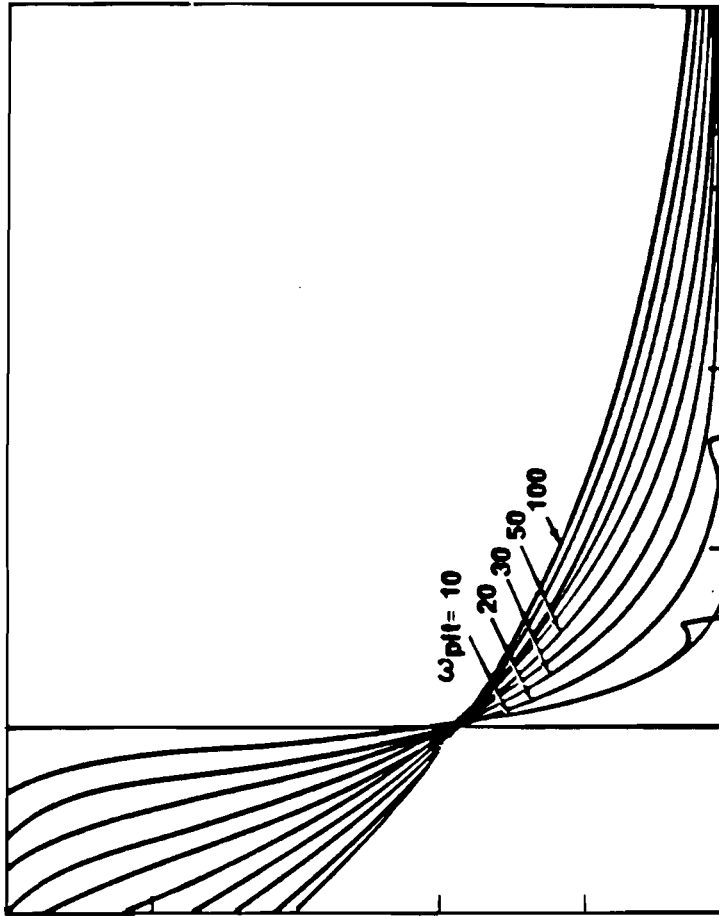
Unfortunately equations (16) and (17) can not again be integrated analytically,²⁶ and therefore are integrated numerically. The process is as follows.

Initially, Poisson's Equation is solved, relaxing the potential and the electron density about the fixed ion background. The initial response is a region of electron space charge in the vacuum half space, concentrated near the ion density discontinuity. The resulting electric field exerts a force on the ions directed towards the vacuum half space. Given this electric field, the equation of motion advances the ion velocity in time which is then used in the equation of continuity to advance the ion density in time. Using the new ion density, Poisson's equation is again solved and the process iterated, advancing the quantities in time as far as desired.

The computations²⁶ give an ion velocity that increases indefinitely with time. The computed density and ion velocity from Ref. 26 have been reproduced in figures 4 and 5.

Naturally, it is hard to imagine an infinite velocity plasma expansion. Then what limits the velocity of the ion front? Well, it may be that some point one or more of the approximations of the similarity

DENSITY DISTRIBUTION



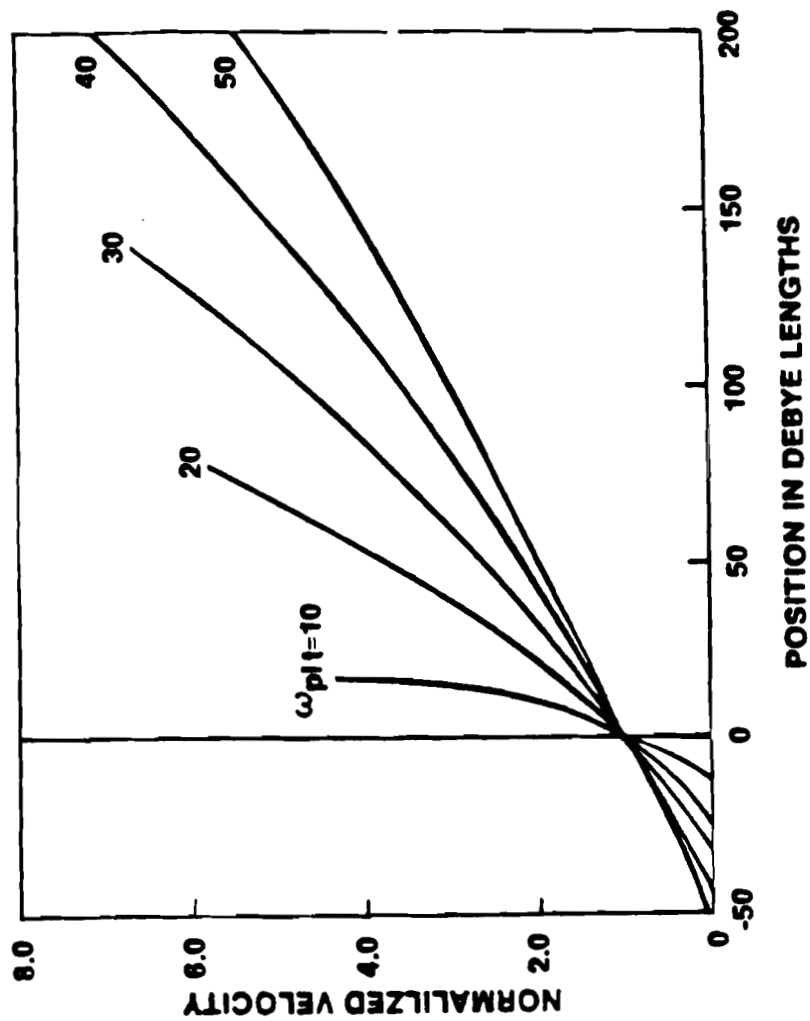
POSITION IN DEBYE LENGTHS

NORMALIZED ION
AND ELECTRON DENSITIES

E916 (Reproduced from J.E. Crow, et. al., J. Plasma Phys., 14, 65, 1975.)

Figure II.4

VELOCITY DISTRIBUTION



E917 (Reproduced from J.E. Crow, et. al., J. Plasma Phys., 14, 65, 1975.)

Figure II.5

solution break down, and from there on the expansion is no longer governed by this analysis.

In the next section we will impose limitations on this analysis that will lead to a finite velocity plasma expansion. Later on we will examine its validity with our experiments.

D. Maximum Expansion Velocity

The isothermal self-similar model of plasma expansion (reviewed earlier) suggests that ions can be accelerated essentially to infinite velocities, by contrast, a Thomson Parabola analyzer (that will be described in the experimental section) shows a clearly defined ion velocity maximum on each shot.

Remember that in deriving the isothermal expansion model we assumed quasineutrality, i.e.,

$$n_e = \sum_i Z_i n_i \quad (\text{II-18})$$

and a Boltzmann distribution of electrons in equation (8C); $n_e = n_0 e^\psi$

$$\text{where } \psi = \frac{e\phi}{kT_e} \quad (\text{II-19})$$

It has been suggested in Ref. 31, that modification can be made in the isothermal expansion model to accommodate for the finite expansion velocity. Here we will merely quote their results as they seem to fit well with experiments.

Two mechanisms could modify the isothermal behavior in a way that would limit ion velocities to the observed maxima: (a) breakdown of equation (18), i.e., no quasineutrality at low densities and; (b) absence of the high temperature Maxwellian tails of the electron velocity distribution, resulting in modification of the Boltzmann distribution of electrons, equation (8C), at low densities.

In mechanism (a), the exponential density profile is truncated by a non-neutral electrostatic sheath, which is formed by charge separation effects. That limits the ion velocity. This happens at a point where the Debye length, $\lambda_D [= (KT_e / 4\pi n_e e^2)^{1/2}]$, equals the density scale length. At this and lower density, charge neutrality and, therefore, coupling of electron pressure to ions should be expected to fail. Numerical simulations³² have been done with this modification as well as the analytical correction³¹ and it has been found that the maximum sheath velocity is given by

$$V_{\max} = 2C_s [1 + \ln(\sqrt{2} \omega_{pio} \Delta t)] \quad (\text{II-20})$$

where $\omega_{pio} = (4\pi n_{i0} Z_i^2 \frac{e^2}{M_i})^{1/2}$, n_{i0} = initial ion density, and (II-21)

Δt is the full width half maximum of the laser pulse.

In mechanism (b), essentially the same effect of exponential density profile truncation is caused by the absence of the Maxwellian tails of the electron velocity distribution. The electron pressure equation of state is effectively modified. Under these quasistatic

conditions the electron velocity distribution can be written as $f_e(E_e)$, where $E_e = 1/2 m_e v_e^2 - e\phi$ is the electron energy. If the tails of the otherwise Maxwellian $f_e \sim \exp(-E_e/KT_e)$ for this almost collisionless plasma are cut off at V_{ed} :

$$V_{ed} = V_{eth} [(E_{ed} + e\phi)/KT_e]^{1/2} \quad (\text{II-22})$$

$$V_{eth} = \left(\frac{2KT_e}{m_e} \right)^{1/2} \text{ is thermal velocity} \quad (\text{II-23})$$

wherever $E_{ed} \gg -e\phi$, f_e is essentially Maxwellian with temperature T_e . However, when $E_{ed} \cong -e\phi$ near some point $\xi = \xi_d$ where the density is a truncated, $V_{ed}/V_{eth} \rightarrow 0$, which is equivalent to having the effective temperature, i.e., mean thermal energy, decrease to zero. Thus the electron pressure is decreased.

A generalization of the procedure that led to the equations (13A) and (15) gives

$$\frac{dn_i}{d\xi} = - \left[\frac{d}{dn_i} \left(n_i \frac{d\psi}{dn_i} \right)^{1/2} + \frac{1}{n_i} \left(n_i \frac{d\psi}{dn_i} \right)^{1/2} \right]^{-1} \quad (\text{II-24})$$

$$\text{and } v_i = \xi + \left(n_i \frac{d\psi}{dn_i} \right)^{1/2} \quad (\text{II-25})$$

Remember here that $[n_i (d\psi/dn_i)]^{1/2} = 1$ from $n_i = \exp(\psi)$. Equations (24) and (25) are solved together with equation (14). Charge neutrality $n_e = Z_i n_i$ is assumed, because when mechanism (b) is operative, it will occur at higher densities than those involved in mechanism (a). The resulting

modified density and field profiles, $n_i(\xi)$ and $E(\xi)$, go to zero at some finite $\xi = \xi_d$, and $v_i(\xi)$ is also modified. For $\xi \rightarrow \xi_d$, equations (24), (25) and (14) give $(V_{md} - V)$, E , and n_i . V_{md} is the maximum ion velocity (V_{max}), and is determined by the distribution cutoff at E_{ed} . These modified isothermal expansions retain self-similarity. Consequently, V_{max} is independent of pulse length, Δt . The density at which the truncation of the expanding plasma occurs, i.e., the density that would be found at ξ_d if the truncation did not occur, can now be obtained from equation (18), charge neutrality and equation (26)

$$N_{ed} = N_{id} \cong \exp(-V_{max}) \quad (\text{II-26})$$

From an experimental point of view mechanism (b) seems to be more attractive. In the case of mechanism (a) the logarithm in equation (20) makes V_{max} too insensitive to experimental parameters. Since V_{max} has been observed to vary under experimental conditions, mechanism (a) does not seem to be a likely candidate.

E. Hot Electron Temperature

From the self-similar, isothermal model of plasma expansion, hot electron temperature can be readily obtained with the knowledge of ion density distribution function. Recall equation (12)

$$n_i = n_{i0} e^{-v_i/C_s}$$

$$\text{or, } \frac{dn_i}{dv_i} = - \frac{n_{i0}}{C_s} e^{-v_i/C_s} \approx \alpha e^{-v_i/C_s} \quad (\text{II-27})$$

$$\alpha = - \frac{n_{i0}}{C_s} = \text{constant, } C_s = \sqrt{\frac{KT_e Z_i}{M_i}} = \text{ion sound speed.}$$

Equation (27) can be transformed to give

$$v_i = - \left(\frac{KT_e Z_i}{M_i} \right)^{1/2} \ln \left(\frac{dn_i}{dv_i} \right) + C_s \ln \alpha \quad (\text{II-28})$$

If $\ln(dn_i/dv_i)$ is plotted against v_i , for isothermal expansion to be valid one would expect the plot to be a straight line, the slope being proportional to $\sqrt{T_e}$. We have employed this technique to find hot electron temperatures from our experimental results for ion distributions as we will see later.

The variation of hot electron temperature with intensity and wavelength has been theoretically investigated. The numerical description^{33,34} of electron heating by resonant absorption predicts $T_e \sim (I\lambda^2)^n$, $0.3 < n < 0.4$. In addition, flux limit arguments in which the bulk of the electrons are stochastically heated in a region around the critical density predict³³ that the electron temperature scales as $(I\lambda^2)^{2/3}$.

F. Multispecies Plasma Expansion

So far we have described the plasma by a two fluid model involving hot electrons and relatively cold ions. In practice, for a laser produced plasma this is not true. In general, ion groups with different charge

to mass ratios (having either different charges or different masses) are formed. This, however, does not change the prescription of isothermal similarity model. Now, all ion groups are treated as separate fluids and they satisfy their own equations of momentum and continuity. The set of equations (10) for multiple ion species changes to

$$(v_{i,j} - \xi) \frac{dn_{i,j}}{d\xi} + n_{i,j} \frac{dv_{i,j}}{d\xi} = 0 \quad (II-29)$$

$$(v_{i,j} - \xi) \frac{dv_{i,j}}{d\xi} = - \frac{eZ_j}{M_j} \frac{d\phi}{d\xi}$$

where, $j = 1, 2 \dots$ for different ion species. Electron density is found by

$$n_e = \sum_j Z_j n_{i,j} \quad \text{and} \quad n_e(\phi) = n_{e0} e^{-e\phi/KT_e} \quad (II-30)$$

Therefore,

$$\frac{d\phi}{d\xi} = \frac{-KT_e}{e \sum_j Z_j n_{i,j}} \sum_j Z_j \frac{dn_{i,j}}{d\xi} \quad (II-29A)$$

Now, we take a particular case (which is relevant to us), in which protons ($Z/M = 1$) are accompanied by heavy ions, e.g., O^{+8} , O^{+7} etc. (with $Z/M = 0.5$, 0.43 etc.), and we estimate the relative acceleration of different species in multispecies plasma expansion.

We assign $j = 1$ to protons and $j = 2, 3 \dots$ to heavy ion species (O^{+8} , $O^{+7} \dots$ etc.); then for $n_{i,1} Z_1 \gg n_{i,2} Z_2 \approx n_{i,3} Z_3$ the potential will be essentially determined by the proton component and

$$\frac{d\phi}{d\xi} = \frac{-KT_e}{en_{i,1}} \frac{dn_{i,1}}{d\xi} \quad (II-29B)$$

Substituting this in (29), the acceleration of the protons is

$$\begin{aligned}
 (v_{i,1} - \xi) \frac{dv_{i,1}}{d\xi} &= \frac{Z_1 K T_e}{M_1 n_{i,1}} \frac{dn_{i,1}}{d\xi} \\
 &= c_s^2 \left(\frac{1}{n_{i,1}} \frac{dn_{i,1}}{d\xi} \right)
 \end{aligned} \tag{II-29C}$$

where $c_s^2 = \frac{Z_1 K T_e}{M_1}$

Similarly the acceleration of O^{+8} is given by

$$(v_{i,2} - \xi) \frac{dv_{i,2}}{d\xi} = \frac{(Z_2/M_2)}{(Z_1/M_1)} c_s^2 \frac{1}{n_{i,1}} \frac{dn_{i,1}}{d\xi} \tag{II-29D}$$

We notice here that the acceleration of each species is proportional to its charge to mass ratio and is very sensitive to the density scale length $[(1/n_{i,1})(dn_{i,1}/d\xi)]^{-1}$ of protons. Because $1 > [(Z_2/M_2)/(Z_1/M_1)] \approx [(Z_3/M_3)/(Z_1/M_1)]$, when protons are present they will acquire higher acceleration than the rest of the species. Moreover, heavy ions will have comparable accelerations because of their close charge to mass ratios. As we will show later our observations are consistent with this. For detailed analysis, the analytical solution is not possible and one needs to resort to numerical analysis.^{27,28,29}

G. Total Number of Energetic Ions

In order to estimate the total energy carried away by fast ions one would like to know the total number of these energetic ions. Moreover, as we will explain in the experimental section, we were able

to measure the number of ions with velocities of ion sound or higher (this is the range we have defined as energetic or fast ions), therefore, we would like to make a theoretical estimate to compare with our experiments. A precise estimate demands a knowledge of the regime where the ions are generated. Therefore, only a crude order of magnitude type of estimate is possible. We will follow the estimation as prescribed by Ref. 35.

The energy gained by ions from the hot electrons produced by resonant absorption of radiation can be expressed by

$$\frac{1}{2} \sum_i n_i M_i v_i^2 = E^2 / 8\pi \quad (\text{II-31})$$

where E is the electric field intensity, n_i is the number density of ions at the critical point, M is the mass and the summation is over the species of ions.

If we recall equation (3), we find that electric field intensity decreases with increasing distance from the critical density point x_c . It seems that the velocity of this motion depends on the coordinate. When the electric field decreases sufficiently to make the velocity $V(x)$ comparable with the sound speed C_s , the ion acceleration efficiency decreases. It can therefore be stated that accelerated ions are produced with velocities ranging from that of sound to a value of V_{\max} determined by the maximum field value. Now, we can estimate the total number of ions that take part in acceleration, if we estimate that spatial region in which the velocity of electromagnetic wave lies in the range from V_{\max} to C_s . Here we rewrite equation (3)

$$|E_x| = \frac{\phi(\tau)E_0\sqrt{c}}{\sqrt{2\pi L\omega_0}} \left\{ \left(\frac{x-x_c}{L} \right)^2 + \frac{v^2}{\omega_0^2} \right\}^{-1/2} \quad (\text{II-3})$$

$$|E_x| = |E_{\max}|, \text{ when } x = x_c$$

$$\text{or, } |E_{\max}| = \frac{\phi E_0 \sqrt{c}}{\sqrt{2\pi L}} \frac{\sqrt{\omega_0}}{v} \quad (\text{II-32})$$

At the point where $v = C_s$ (ion sound speed), the thermal pressure of the plasma $4\pi(n_e K T_e + n_i K T_i)$ approximates the radiation pressure

$$\text{or, } |E_{xt}|^2 = 4\pi(n_e K T_e + n_i K T_i) \quad (\text{II-33})$$

$$\text{But } |E_{xt}| = \frac{\phi(\tau)E_0\sqrt{c}}{\sqrt{2\pi L\omega_0}} \frac{L}{(x_t - x_c)} \quad (\text{II-34})$$

neglecting collisions, as $v \rightarrow 0$.

The spatial width where energetic ions are produced

$$(x_t - x_c) = \Delta x = \frac{\phi(\tau)E_0 L \sqrt{c}}{\sqrt{2\pi L\omega_0} |E_{xt}|} \quad (\text{II-35})$$

Substituting equation (33) in (35), we have

$$\Delta x = \frac{\phi(\tau)E_0 L \sqrt{c}}{\sqrt{2\pi L\omega_0} \sqrt{4\pi(n_e K T_e)}} \quad (\text{II-36})$$

Since $T_e/T_i \gg 1$, ion pressure has been neglected.

If n_c is the density of ions near the critical surface x_c , then the total number of ions in the spherical shell of plasma near the critical

surface is given by

$$N = n_c 4\pi x_c^2 \Delta x$$

$$= n_c 4\pi x_c^2 \frac{\phi(\tau) E_0 \sqrt{L} \sqrt{c}}{\sqrt{2\pi\omega_0} \sqrt{4\pi n_e K T_e}}$$

Here the quantity

$$\frac{n_c 4\pi x_c^2 \phi(\tau) \sqrt{c}}{\sqrt{2\pi\omega_0} \sqrt{4\pi n_e K}} = K_1$$

can be assumed constant for the particular plasma conditions. Then the total ion number is

$$N = K_1 \frac{E_0 \sqrt{L}}{\sqrt{T_e}} \quad (\text{II-37})$$

For laser intensity I , $E_0 \sim \sqrt{I}$, experimental results show $T_e \sim I^{0.32}$, and the numerical simulations³³ have shown that the density scale length $L \sim I^{-0.48}$. Incorporating these dependences in (37) we have,

$$N \sim I^{0.1} \quad (\text{II-38})$$

This indicates that total number of energetic ions is very insensitive to laser intensity, but that their energy is not as seen from equation (31).

H. Prepulse or Double Pulse Effect

In case of the prepulse irradiation of the target, it is believed that an underdense plasma ablation halo, is formed away from the target, before the arrival of the main pulse. To our knowledge no complete theoretical or numerical analysis of the prepulse irradiation effects exists, however we suggest here some of the generally agreed upon interaction physics. For similar intensities of main pulse, the density scale length may remain unaffected at and near the critical surface, in cases of short single pulses and small prepulse irradiation. There is no doubt from the experimental observations,³⁶ however, that a longer scale length plasma is formed in the underdense region ($n \leq n_c$) by the prepulse. The size of the scale length may depend upon the relative intensity and the delay of main pulse to prepulse.

Long underdense (below critical) plasma scale lengths can effect the absorption physics. In particular, they are very conducive to large stimulated Brillouin scatter of light.^{36,37,38} When incident electromagnetic wave decouples into an ion acoustic wave and a scattered electromagnetic wave which has a frequency very similar to incident wave, differing only by ion acoustic frequency, the process is called Brillouin scattering. An excellent review of this mechanism is given in Ref. 36. Brillouin scattering can reflect a large fraction of incident light.

Measurements^{36,38} have shown greatly enhanced Brillouin scatter (by up to a factor of 3) and significantly reduced absorption of the second (main) pulse (in some cases by up to a factor of 2) in the presence of a prepulse formed plasma. We will try to explain the changes that

take place in absorption mechanisms and thus in total absorption.

In short single pulse experiments with high intensities ($> 10^{14}$ watts/cm²), the resonant absorption is the dominant process. Because of the steeper density gradients, less back scatter is expected and this is observed experimentally, i.e., stimulated Brillouin scattering plays an insignificant role. The computer simulations³⁹ have predicted that in the intensity range of $10^{15} - 10^{16}$ watts/cm² total absorption is about 42% with resonant absorption accounting for about 30%. The total absorption percentage remains almost constant in this intensity range. The increase in total absorption follows closely an increase in resonant absorption while Brillouin scattering remains unchanged. This will increase the energy coupled to hot electrons, resulting in higher hot electron temperature. The energy coupled to ions will increase, and a faster ion spectrum should be expected. On the other hand, for the double pulse case, the low density plasma resulting from the prepulse case and its longer scale length greatly enhances Brillouin back scatter. The total absorption is significantly reduced. The absorption physics is then dominated by the complicated interplay, in the underdense region, between classical and/or anomalous absorption, and back scatter. In computer simulations³⁹ of the double pulse case, the total absorption varies from 38% at 10^{15} w/cm² to 30% at 5×10^{15} w/cm², the resonant absorption from 14% to 9%, whereas the back scatter fraction is increased from 40% to 60%. Because of the reduced absorption and the manner in which the absorption takes place, less light actually gets to the critical region and the fraction of resonant absorption is reduced. This results in decreased energy coupling to hot electrons. For the

same intensity of main pulse one would expect lower electron temperature and a less energetic spectrum of ions for the prepulse case compared to single main pulse case. Moreover, the experimental observations by B. H. Ripin, et al. (Ref. 38) indicate that the absorption fraction goes down (as much as by factor of 2) and the back scatter²² goes up (by a factor of more than 2) when the intensity of the prepulse is changed from 1/10 of a percent to 10% of the fixed intensity main pulse. No significant change was observed for different delays between prepulse and main pulse. Furthermore, for the fixed ratio of prepulse to main pulse intensity, the back scatter percentage increased with the intensity of the main pulse. Once the back scatter becomes important, less light gets to the critical surface and the electron temperature does not increase any more. One would expect, in this case, that not only will electron temperature have a weak dependence on main pulse intensity, but also for a fixed main pulse intensity the hot electron temperature, the energy contained in ions will go down as the intensity ratio of prepulse to main pulse is increased. The time delay between the main pulse and the prepulse will not have much impact; the simulations³⁹ also back up this notion.

In sections to follow, we will present our experimental results, and discuss their agreement or lack of it, to the reasoning outlined here.

III. THEORY OF TWO STREAM ION-ION INSTABILITY IN PLASMA

In a multispecies plasma expansion, the ions with different charge to mass ratios (Z/M) may acquire relative velocities due to their different accelerations in the electric field if the ion-ion collision time¹ ($\sim 1.5 \times 10^{18} M_i^{1/2} T_i^{1/2} / Z^4 N_i$) is long compared to the typical acceleration time ($\sim 10^8 \times L/C_s$, L = density scale length, C_s = ion sound speed). This effect has been discussed in the previous chapter. These cold streaming ions in the hot electron background could be subject to a two-stream ion-ion instability.^{2,3} Two stream instability can be explained as follows. Suppose that the ion component of a plasma consists of two or more beams of different species moving relative to each other. A very small perturbation away from zero field at a given point causes a velocity modulation of each beam. In time, this produces a bunching of space charge in the direction of motion of each beam, which creates a much larger potential than that due to the original perturbation. The fields due to any one beam modulate the other beam, which then feed the disturbance back to the source in a highly amplified form. Thus a perturbation builds up cumulatively and an instability results. The possibility of such an instability had been suggested earlier.^{4,5,6}

One objective of this study is to determine the conditions for this instability, and the dependence of its growth rate on the (Z/M) ratios and the density portions of the ion mixture. It will be shown that a linear analysis leads to a substantial growth of the perturbation. This may lead to a short-wavelength ion density fluctuations. The saturation mechanism may be Landau damping, due

to trapping and subsequent heating of ions. This will be explained later. The model is then used to explain the large amplitude, high frequency modulations observed in the asymptotic non-thermal ion distribution.

A. Dispersion Relation

The one dimensional system that we consider here is that of a fluid mixture of two species of positively charged ions, of charges Z_1 and Z_2 , masses M_1 and M_2 , immersed in a background of electrons. If $T_e \gg T_i$, the thermal spread of ion velocities is then of little importance and hydrodynamic equations can be used for the translational velocities. The equations of momentum and continuity for the cold ions are,

$$\frac{\partial n_i}{\partial t} + \frac{\partial}{\partial x} (n_i v_i) = 0$$

(III-1)

$$\frac{\partial v_i}{\partial t} + v_i \frac{\partial v_i}{\partial x} = \frac{-Z_i e}{M_i} E$$

Neglecting electron inertia for low frequency ($\ll \omega_p$) phenomena, the electron momentum equation for isothermal electrons gives

$$E = -\nabla\phi = \frac{-T_e}{en_e} \frac{\partial n_e}{\partial x}$$

Poisson's Equation

$$\nabla^2 \phi = 4\pi e (\sum_i Z_i n_i - n_e)$$

These equations are perturbed about a homogenous equilibrium where the two ion species have a relative velocity. We take perturbations of the form $e^{ikx-i\omega t}$; subsequent linearization of these equations yield a dispersion relation,⁸

$$1 + k^2 \lambda_D^2 = \frac{\xi}{(x+\beta)^2} + \frac{\eta}{(x-\beta)^2} \quad (\text{III-2})$$

where $\lambda_D = (KT_e/4\pi n_e)^{1/2}$ Debye length, $\xi = \gamma_1 C_{s1}^2$, $\eta = \gamma_2 C_{s2}^2$,
 $\gamma_1 = n_1/n_1+n_2$, $\gamma_2 = n_2/n_1+n_2$, $C_{s1} = \sqrt{Z_1 T_e/M_1}$, $C_{s2} = \sqrt{Z_2 T_e/M_2}$,
 $x = V_p - V_r/2$, $\beta = V_r/2$, $V_p = \text{phase velocity } (\omega/k)$ and $V_r =$
 relative velocity of two fluids.

B. Growth Rates in Homogeneous Expanding Plasma

The dispersion relation (III-2) can be written in the form

$$x^4 - x^2 \left\{ 2\beta^2 + \frac{(\xi+\eta)}{(1+k^2 \lambda_D^2)} \right\} + 2x\beta \frac{(\xi-\eta)}{(1+k^2 \lambda_D^2)} + \beta^2 \left\{ \beta^2 - \frac{(\xi+\eta)}{(1+k^2 \lambda_D^2)} \right\} = 0 \quad (\text{III-3})$$

In general, the quartic equation (III-3) has four roots. Because we are interested in the condition for the instability, we impose parametric conditions so that the equation (III-3) has two real and

two complex conjugate roots, one of which corresponds to instability. This is also called the condition for which equation (III-3) has unstable (double) roots.¹¹

If $\xi = \eta$ and the ion species are different, the condition that equation (III-3) will have unstable roots (condition for ion-ion instability in this case) is

$$0 < v_r \leq \frac{2c_s}{(1+k^2\lambda_D^2)^{1/2}} \quad (\text{III-4})$$

For the case when $(\xi-\eta) \ll (\xi+\eta)$ the instability criterion becomes

$$v_r^2 \leq \frac{4(\xi+\eta)}{(1+k^2\lambda_D^2)} \left[1 - \frac{1}{3} \left(\frac{\xi-\eta}{\xi+\eta} \right)^2 + \dots \right] \quad (\text{III-5})$$

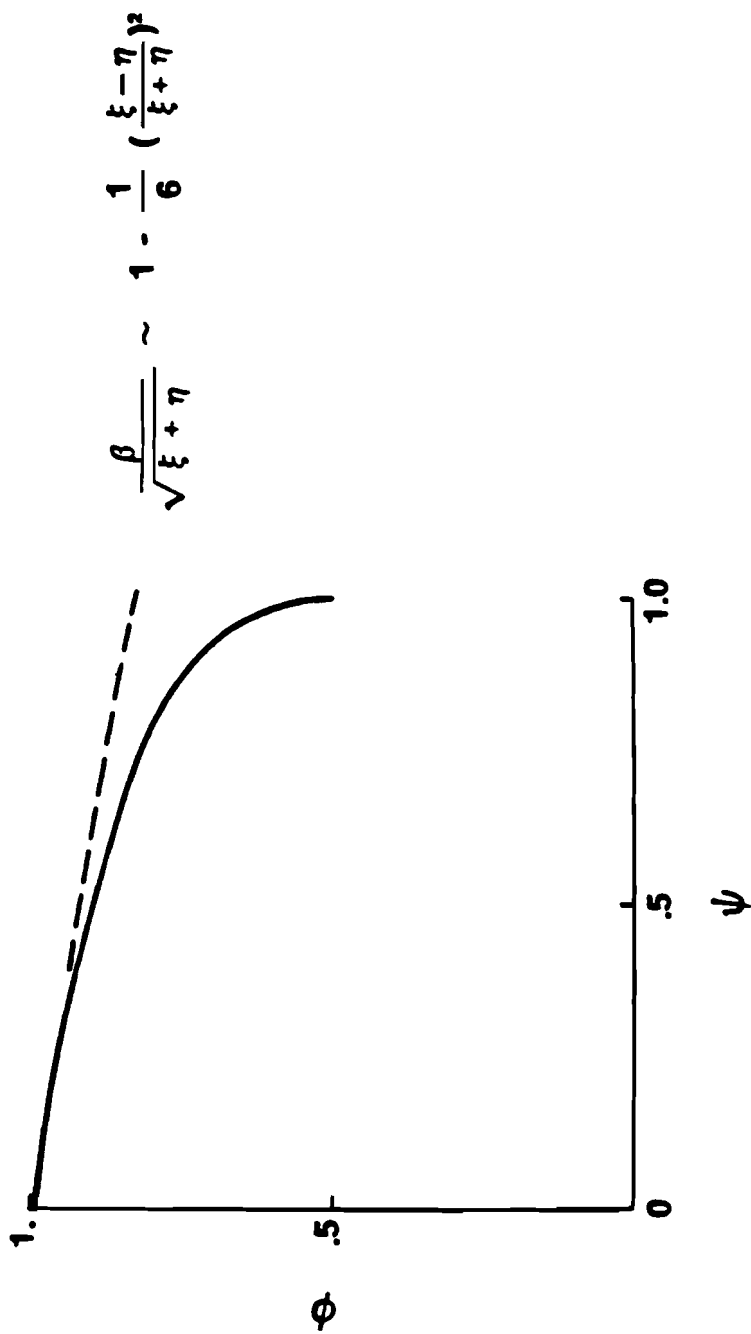
Because $(\xi-\eta)/(\xi+\eta)$ has been assumed $\ll 1$, only the terms $O \left[\left[(\xi-\eta)/(\xi+\eta) \right]^2 \right]$ have been kept.

In the general case the quartic equation (III-3) can be solved numerically to yield growth rates ($\gamma = \text{Im}\omega$) for different values of γ_1 , γ_2 , Z_1/M_1 and Z_2/M_2 . A plot of the threshold velocity as a function of the stream densities and the sound speed is shown in figure III.1. Values of the imaginary part of the phase velocity $V_p (= \gamma/K)$ have been calculated as a function of relative stream velocities for different ξ/η ratios as shown in figure III.2.

C. Application to Experimental Observations

Now we attempt to explain the experimental observation. Figure III.3

TWO STREAM THRESHOLD VELOCITY AS A FUNCTION OF STREAM DENSITIES AND SOUND SPEED



E1043

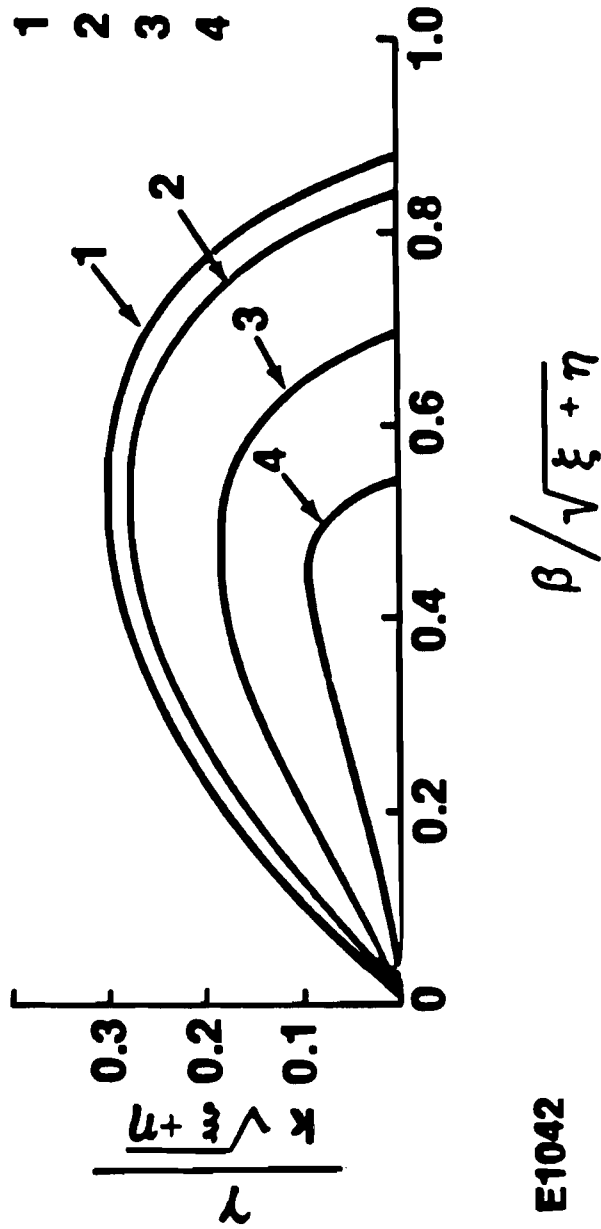
Figure III.1

GROWTH RATE VERSUS RELATIVE VELOCITY



PLOT $\left| \frac{\xi - \eta}{\xi + \eta} \right|$

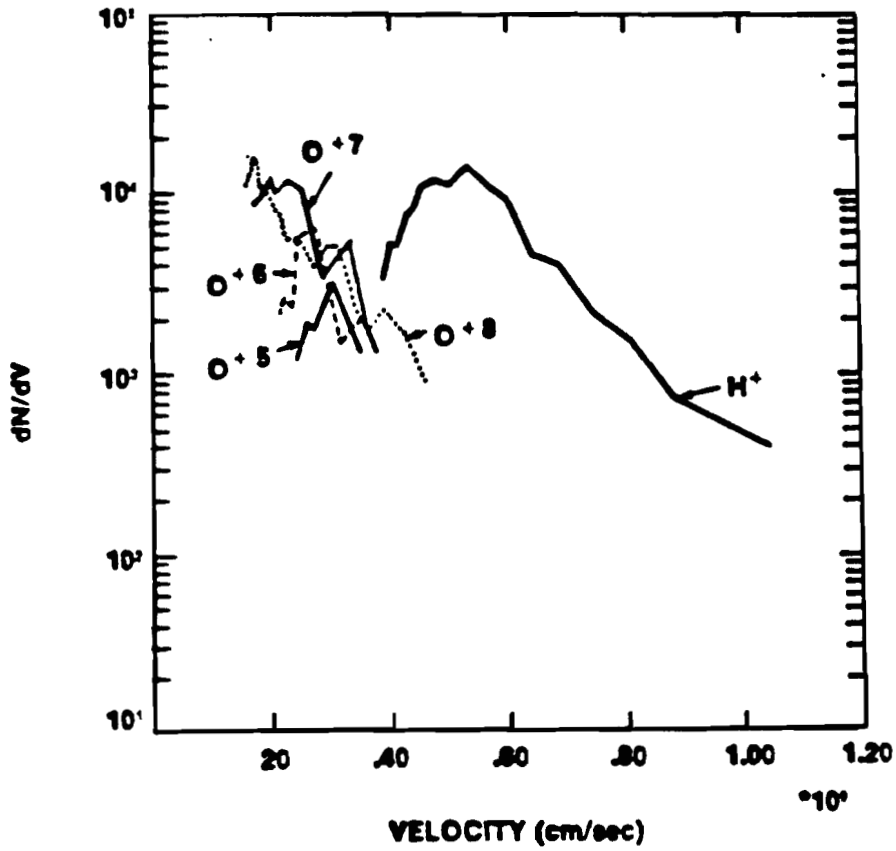
- 1 0.0
- 2 0.5
- 3 0.9
- 4 0.99



E1042

Figure III.2

ION SPECIES DENSITY DISTRIBUTION AS A FUNCTION OF VELOCITY



E1034

Figure III.3

shows the asymptotic ion distribution function as measured by the "Thomson Parabola" in an arbitrary energy band. Experimental conditions are: Nd: Glass Laser, $I = 10^{15}$ watts/cm², glass micro-balloon 80 μm -diam., 0.8 μm thick, and surface focussed. The density modulations as seen are characteristics of several shots under different experimental conditions. We investigate two groups of ions for this instability, having a similar and a dissimilar Z/M. Usually in a laser produced plasma the protons are followed by a group of heavy ions. We take the cases where $Z_1/M_1 = 1$ (protons) and $Z_2/M_2 = 0.5$ are in one group (H/L), and $Z_1/M_1 = 0.5$ and $Z_2/M_2 = 0.4$ are in other group (H/H). Except for the proton case, the distribution shows about 4-5 peaks.

Given the growth rate of the instability for an infinite homogeneous plasma, we would now like to estimate the total growth of an initial wave packet as it propagates through the rarefying plasma, characteristic of a laser fusion target corona. To analyze the character of these features and their dependence on the parameters it is natural to use, as before, hydrodynamic equations. As a model of such a plasma we will use the self-similar, two ion species, isothermal rarefaction model of Gurevich.⁹ The equations have the following form,

$$(u_1 - \tau) \frac{dN_1}{d\tau} + N_1 \frac{du_1}{d\tau} = 0$$

$$(u_1 - \tau) \frac{du_1}{d\tau} + \frac{Z_1 \frac{dN_1}{d\tau} + Z_2 \frac{dN_2}{d\tau}}{2(Z_1 N_1 + Z_2 N_2)} = 0$$

$$(u_2 - \tau) \frac{dN_2}{d\tau} + N_2 \frac{du_2}{d\tau} = 0$$

$$(u_2 - \tau) \frac{du_2}{d\tau} + \frac{M_1 Z_2}{2M_2 Z_1 (Z_1 N_1 + Z_2 N_2)} \left(Z_1 \frac{dN_1}{d\tau} + Z_2 \frac{dN_2}{d\tau} \right) = 0 \quad (\text{III-6})$$

Here N_1 and N_2 are ion concentrations and $u_1 = v_1 (2T_e Z_1 / M_1)^{-1/2}$,
 $u_2 = v_2 (2T_e Z_2 / M_2)^{-1/2}$, $\tau = (x/t) (2T_e Z_1 / M_1)^{-1/2}$, T_e = electron
 temperature, v_1 and v_2 are the mean velocities of the fluids.

These equations are derived in the same manner as the equation 10
 (Chapter II). Implicit in the derivation of these equations is
 quasineutrality, $n_e = \sum_i Z_i n_i = n_0 e^{e\phi/KT_e}$ where n_e = electron density,
 n_0 = unperturbed electron density and ϕ = potential.

For the set of linear equations (III-6) to possess a solution,
 the determinant of the coefficients should be zero, i.e.,

$$Z_1 N_1 (u_2 - \tau)^2 \left[(u_1 - \tau)^2 - \frac{1}{2} \right] + Z_2 N_2 (u_1 - \tau)^2 \left[(u_2 - \tau)^2 - \frac{M_1 Z_2}{2M_2 Z_1} \right] = 0 \quad (\text{III-7})$$

Starting with $u_1 = 0$, $u_2 = 0$ and initial τ obtained from the
 equation (III-7) we mapped out numerically the density profile of
 the ion mixture as a function of τ . The density profiles for heavy
 ions ($N_1 = 0.5$, $Z_1/M_1 = 0.5$, $N_2 = 0.5$, $Z_2/M_2 = 0.4$) and, heavy and
 light ions ($N_1 = 0.25$, $Z_1/M_1 = 1$, $N_2 = 0.75$, $Z_2/M_2 = 0.5$) have
 been shown in figures III.4 and III.5. The ratios of the densities
 were chosen according to the experimental observations.

We compute the total growth of a packet, G , by integrating the

DENSITY DISTRIBUTION AS A FUNCTION OF τ FOR HEAVY ION SPECIES

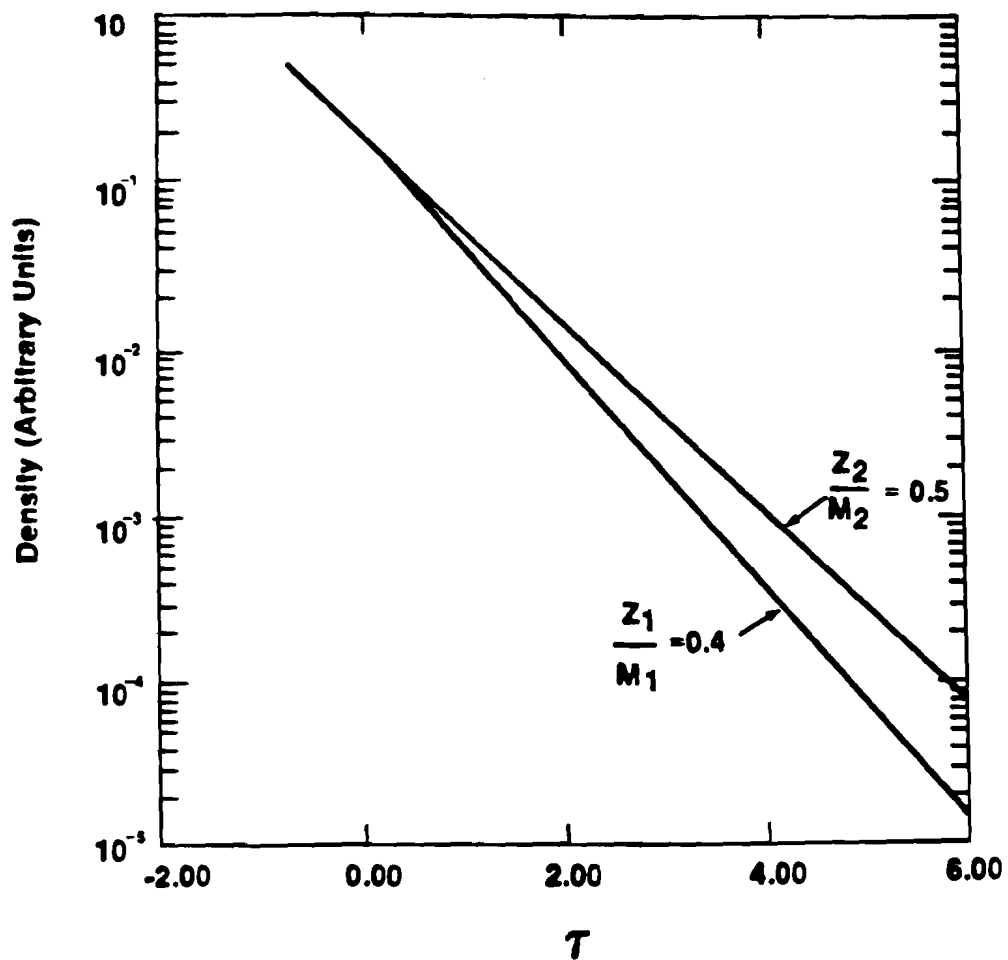
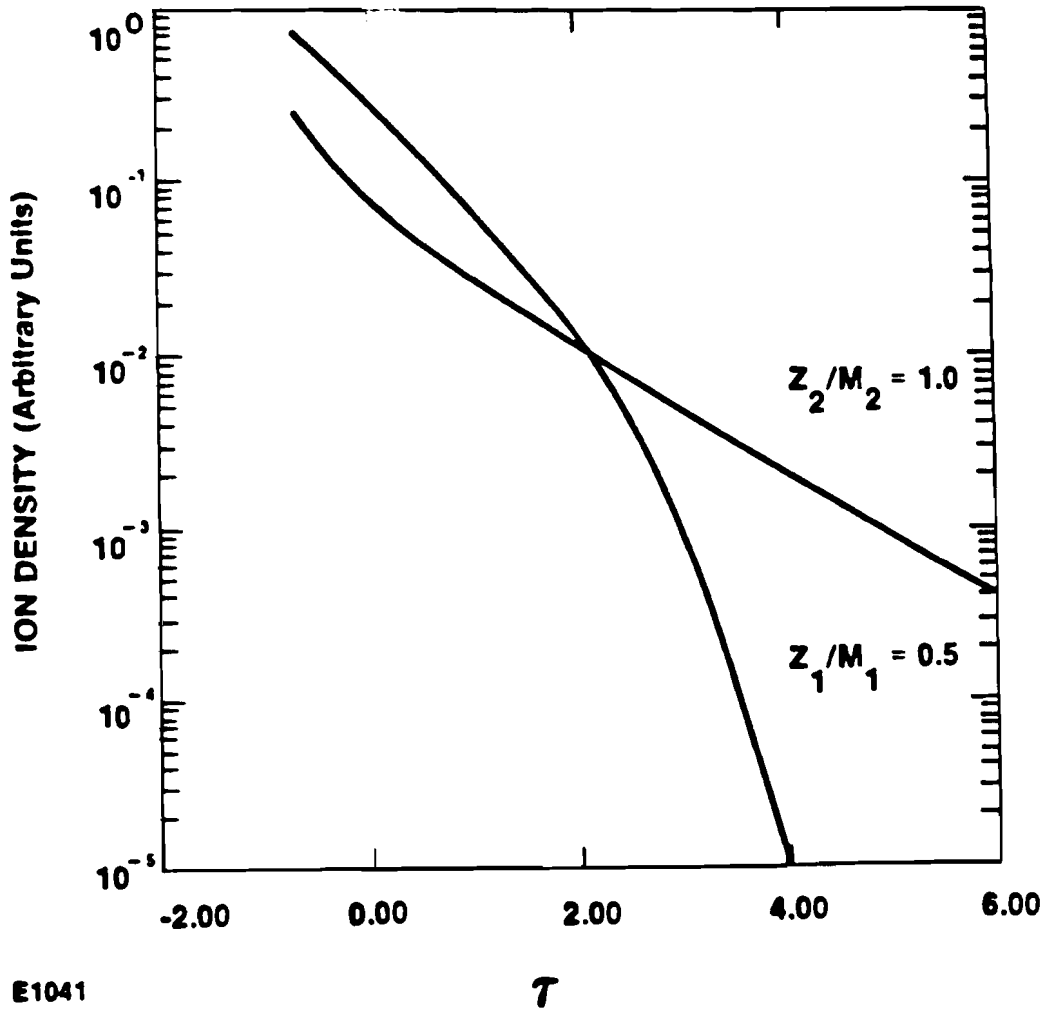


Figure III.4

DENSITY DISTRIBUTION AS A FUNCTION
OF τ FOR PROTONS (LIGHT IONS)
AND OXYGEN (HEAVY IONS)

UR
LLE



E1041

τ

Figure III.5

local growth rate along the trajectory of the packet $x(t)$ given by

$$G(t) = \int_{t_0}^t \gamma(x(t')) dt'$$

$$\gamma = k \text{Im}(V_p)$$

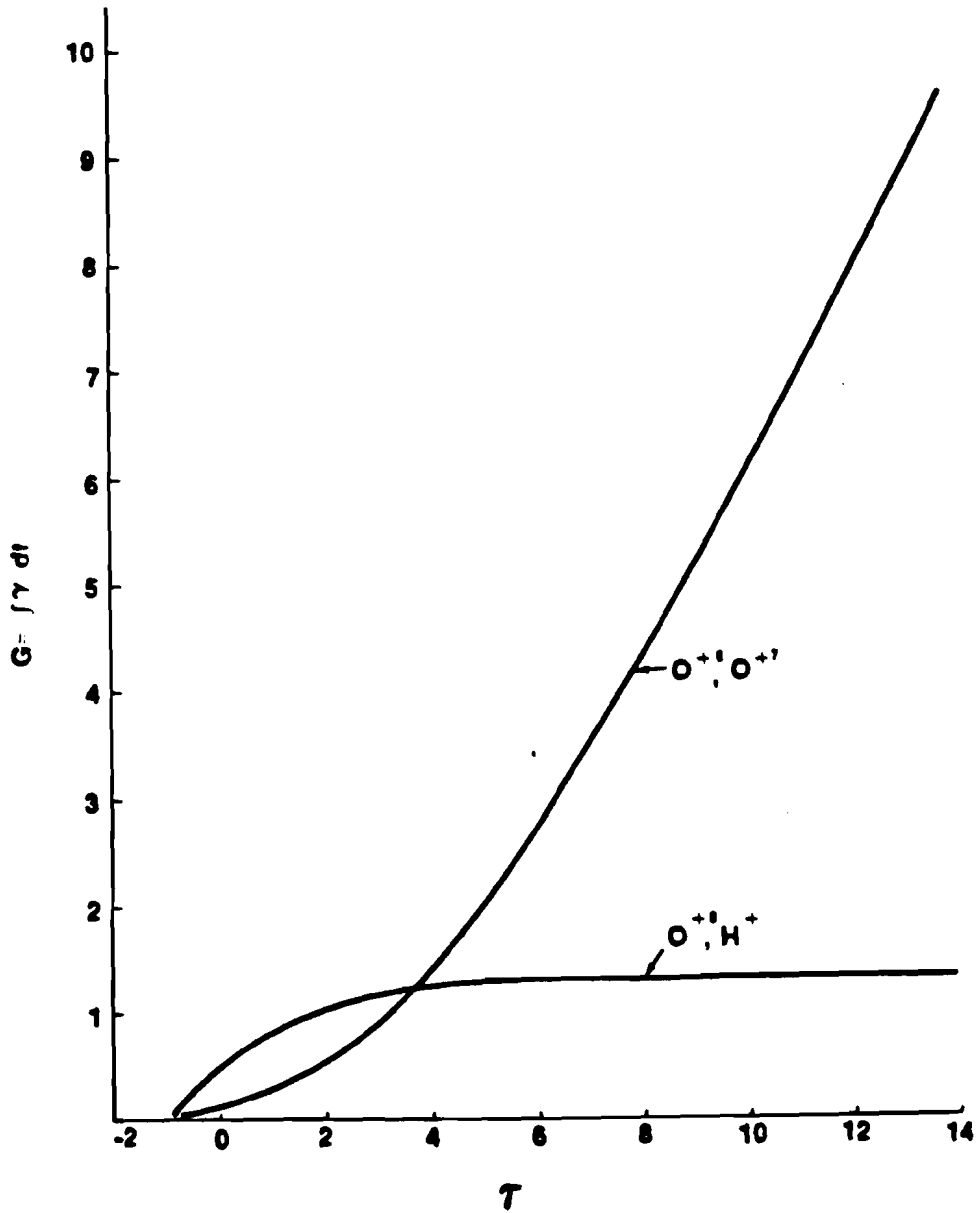
$$\frac{dx}{dt} = V(x,t) + R_e(V_p); \text{ from } x = x_0, t = t_0$$

$$k = k_0 \left(\frac{dx}{dx_0} \right)^{-1} = k_0 \exp \left[- \int_{t_0}^t \left(\frac{dV}{dx} + \frac{d}{dx} R_e(V_p) \right) dt \right]$$

The integration is continued until the growth, G , saturates. The total growth of the wave packet for both ion groups has been shown in figure (III.6). To maximize G , one clearly chooses x_0 , t_0 to be as small as possible to maximize the growth time and k to be as large as possible to maximize the growth rate. One's choice, however, is limited by the assumptions of these simple calculations. The initial time t_0 has to be sufficiently large that the gradient scale length of the rarefaction $L(t_0)$, exceeds the wavelength of the perturbation else inhomogeneity effects would kill the growth rate, that is we require $kL(t_0) \gg 1$. We arbitrarily choose $kL(t_0) = 10\pi$. Secondly, Landau damping and dispersion of the wave packet limit $k\lambda_D \leq 1$. We initially assume $k\lambda_D = 0.6$ and then monitor $k\lambda_D$ through the growth period. For the one species rarefaction $k\lambda_D$ is an exact constant, for two species rarefaction we find it to be approximately so, as shown in figure III.9. We have also estimated the Landau damping rate as a function of $k\lambda_D$ for different electron to ion

TOTAL GROWTH OF THE WAVE PACKET WITH INCREASING τ

UR
LLE



E1039

Figure III.6

$K_{\lambda D}$ AS A FUNCTION OF τ

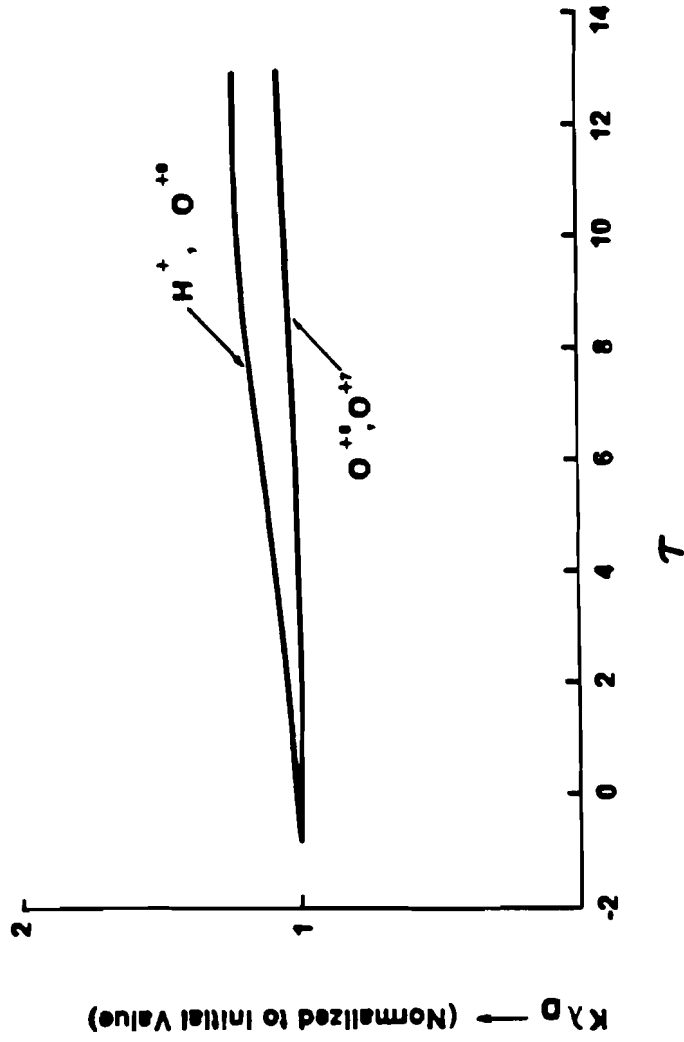


Figure III.9

E1036

temperature ratios.

Landau damping is caused by the particles in the distribution that have a velocity nearly equal to the phase velocity of the wave "the resonant particles". These particles travel along with the wave and do not see a rapidly fluctuating electric field; they, therefore, can exchange energy with the wave effectively. A Maxwellian distribution, however, has more slow particles than fast ones. Consequently there may be more particles gaining energy from the wave than the vice versa, and the wave may be damped. We used the expression for Landau damping from Ref. (10)

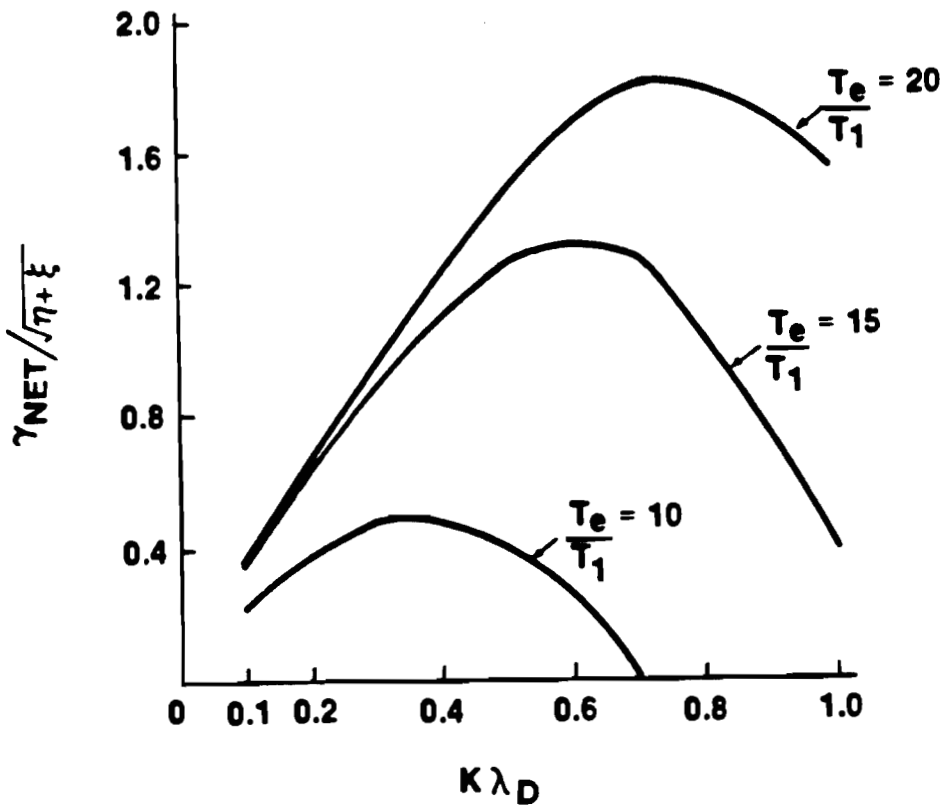
$$\frac{\omega_i}{kC_s} = - \frac{(\pi/8)^{1/2}}{(1+k^2\lambda_D^2)^2} \left[\left(\frac{T_e}{T_i} \right)^{3/2} \exp \left[- \frac{(T_e/T_i)}{2(1+k^2\lambda_D^2)} \right] + \left(\frac{m_e}{M_i} \right)^{1/2} \right]$$

This damping rate has been derived from the fluid theory.

The net growth (after the adjustment for Landau damping rate) is plotted in figure III.10, for T_e/T_i as a parameter. It is evident from the plots that for this instability to grow effectively, a lower bound of T_e/T_i is approximately 10. For known electron temperature, this suggests an upper bound in ion temperature. We also varied the initial position of the wave packet on the density profile, namely x_0 , and monitored the total growth as shown in figure III.8.

As the figure III.7 shows, initially, the growth rate is higher for (H/L) group of ions but it drops down sharply with increasing τ . On the other hand, for (H/H) group of ions the growth rate starts with low value and for large τ , attains saturation. In neither case does

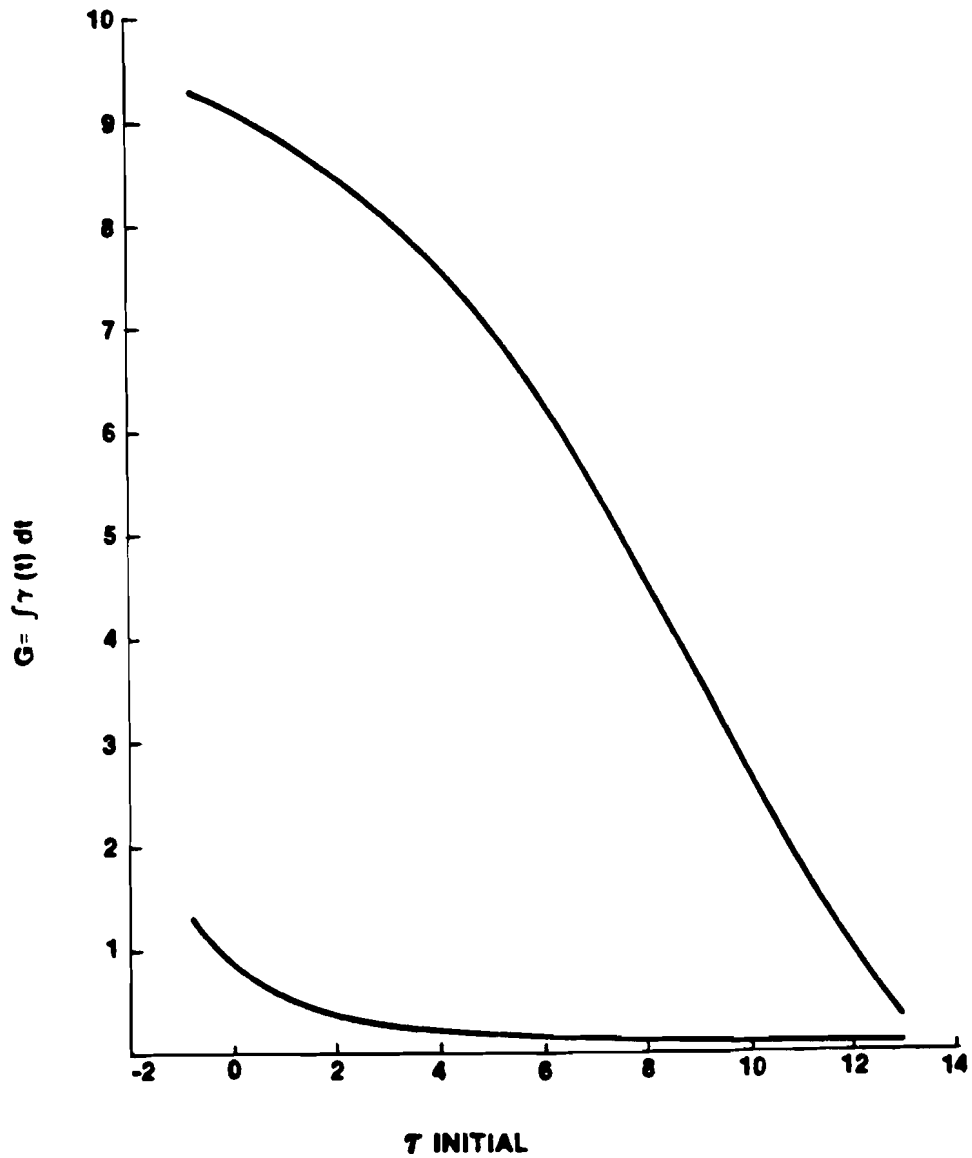
NET GROWTH RATE (AFTER LANDAU DAMPING) VERSUS $K\lambda_D$



E1035

Figure III.10

**TOTAL GROWTH OF WAVE PACKET
ORIGINATING AT DIFFERENT POSITIONS
(τ INITIAL) ON STREAM DENSITY PROFILE**

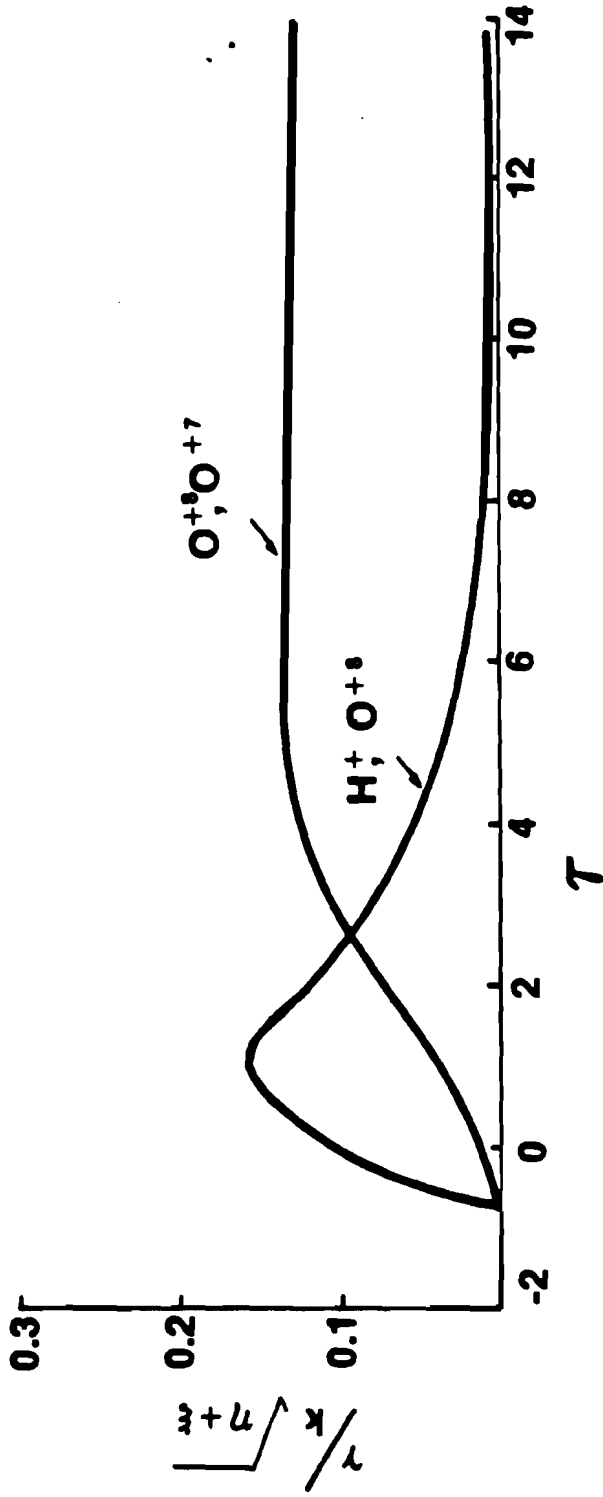


E1037

Figure III.8

**GROWTH RATE AS A FUNCTION OF τ , STREAM
DENSITIES AND SOUND SPEED**

UR
LLE



E1038

Figure III.7

the relative velocity of two species exceed the value required to quench the instability (figure III.2). The growth rate in case of (H/L) group is, however, limited by the rapid fall off of the density of the heavy species with increasing τ .

If we compare the results of H/H and H/L ions groups, growth of (H/H) group is much higher than that of (H/L) group (even though both lie within velocity threshold conditions of instability). We see this behavior in experimental observations in that the proton spectrum is smooth, while the heavy ion species spectra have large fluctuations that we ascribe to the growth of the (H/H) ion-ion instability. We, however, cannot rule out the possibility of protons being generated from the contaminants on the surface of the target and accelerated outward. In this case the density coupling with the heavy ions will not exist to begin with, and a smoother distribution of the protons (as seen) will be expected.

We have shown that the streaming plasma could be short wavelength ($\approx \lambda_D$) ion-ion two stream unstable. The coupling mode of the instability is dominated by the density ratios. This may act as a source to a long wavelength ion acoustic turbulence. Also this model fits very well to our experimental observations.

IV. EXPERIMENTAL SYSTEMS AND INSTRUMENTS

A. Introduction

The experiments were carried out at the College of Engineering and Applied Science's Laboratory for Laser Energetics. The experimental setup used here for high energy ion ($> 10 \text{ Kev/Z}$) studies consisted of a high power Nd: Glass, 50 psec, $1.06 \mu\text{m}$ wavelength laser (called Glass Development Laser: GDL), a two beam target irradiation facility (called Beta target chamber) and the ion spectrograph (called "Thomson Parabola"). In addition, x-ray measurements¹ in 10 Kev-500 Kev range were made. The laser and target performances were monitored on each shot.

As described in the Introduction Chapter (Chapter I), it is easy to understand the negative role played by fast ions in laser fusion experiments. Since it is difficult to make use of these ions, which are copiously produced in many laser-target interactions, it is of present interest to find the appropriate conditions under which their production can be minimized without significantly affecting the implosion dynamics. Naturally, this demands a knowledge of their generation and propagation mechanisms.

The main purpose of this thesis is to conduct systematic parametric studies of the generation and propagation of energetic ($> 10 \text{ Kev/Z}$) ions. There has been a growing interest in the use of structured or shaped or long time scale ($> 1 \text{ nsec}$) pulses for laser fusion target experiments. We attempted to generate these plasma conditions by providing a deliberate prepulse of varying amplitude

and timing with respect to the main pulse. We studied the behavior of energetic ions under these conditions. The specific objectives in this thesis can be itemized as follows:

- a. To examine if there is any laser energy or intensity threshold for the production of energetic ($> 10 \text{ Kev/Z}$) ions in a laser-target interaction.
- b. To measure the asymptotic ion distribution for a variety of charge to mass ratios.
- c. To see if hot electron temperature can be deduced from the ion distribution function.
- d. To estimate the fraction of the target mass carried away by these ions and total energy contained in them.
- e. To measure the maximum expansion velocity of these ions, i.e., to how many times the ion sound velocity (calculated from the hot electron temperature) these ions are accelerated.
- f. To observe the variation of the items (a to e) with a laser prepulse ahead of the main pulse. Two kinds of prepulses were used, one preceded the main pulse by 300 psec and the other by 1100 psec, both were varied in intensity with respect to main pulse from 1% to $10^{-4}\%$.

Other sections of this chapter will briefly illustrate the experimental facility. The main ion diagnostic instrument (Thomson Parabola) will be described in some detail.

B. GDL and Beta Target Chamber

The Glass Development Laser (GDL) System² at the Laboratory for Laser Energetics is a one beam, phosphate glass system capable of delivering peak powers in excess of 0.5 Terrawatts in nominal 50 psec pulses. Figure IV1 shows a schematic diagram of the laser system. The system was modified to insert a controlled prepulse ahead of the main pulse. The modification is shown in figure IV2. The timing of the prepulse, from 300 psec to 1100 psec ahead of the main pulse, was adjusted with the use of a retroreflecting prism mounted on a translational stage as shown in figure IV2. The intensity of the main pulse and prepulse was adjusted independently with the help of two half wave plates in conjunction with the polarizer P. A more detailed description of the system is given elsewhere.³

A vacuum photodiode and a Tektronics 7401 oscilloscope (with built in image intensifier and 1 GHz bandwidth) were used to monitor relative timing between the prepulse and main pulse. A low power shot, i.e. firing only the first four rod amplifiers, was used and the half wave plates were adjusted so that the prepulse and the main pulse beams were of approximately equal intensities. The resulting oscilloscope trace from the photodiode signal indicated the prepulse to main pulse time difference to be 1100 psec. A representative picture is shown in figure IV3. The accuracy of the measurement was limited by the risetime of the scope and about 10 ft of the RG-58 cable. It is estimated to be about 100 psec. With this position of the translation stage marked, the subsequent

SCHEMATIC LAYOUT OF GDL

UFR
LLE

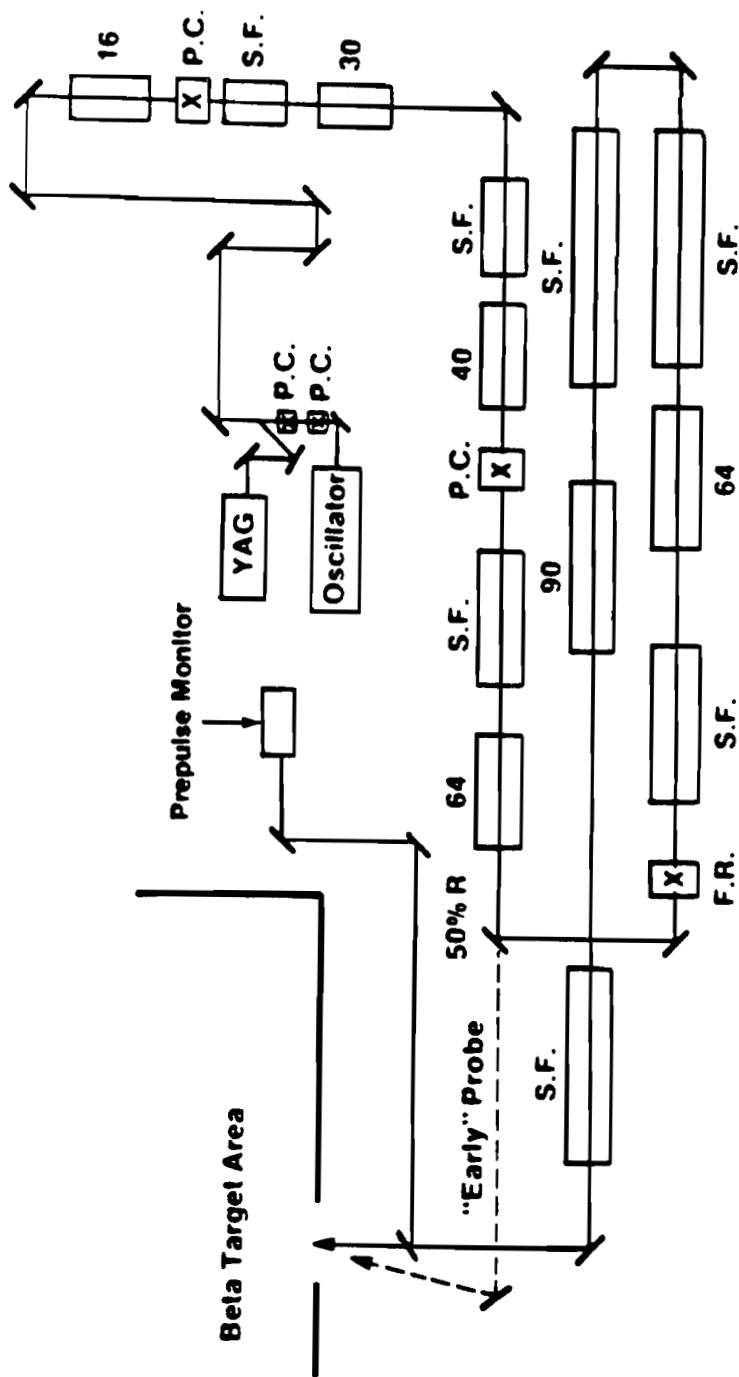


Figure IV.1

E789

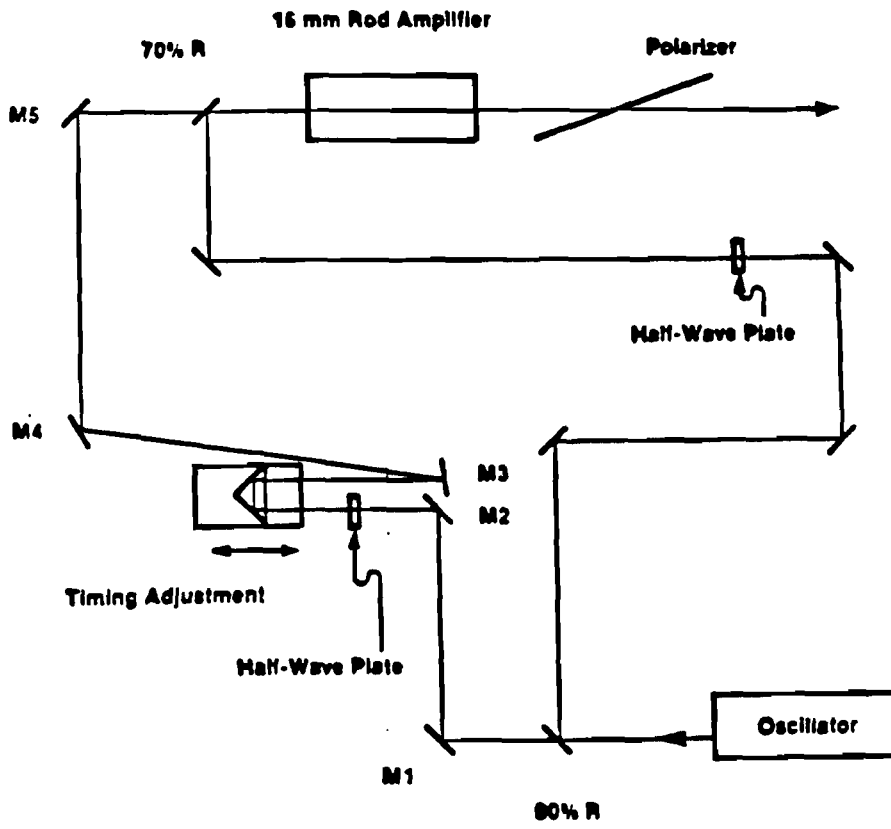
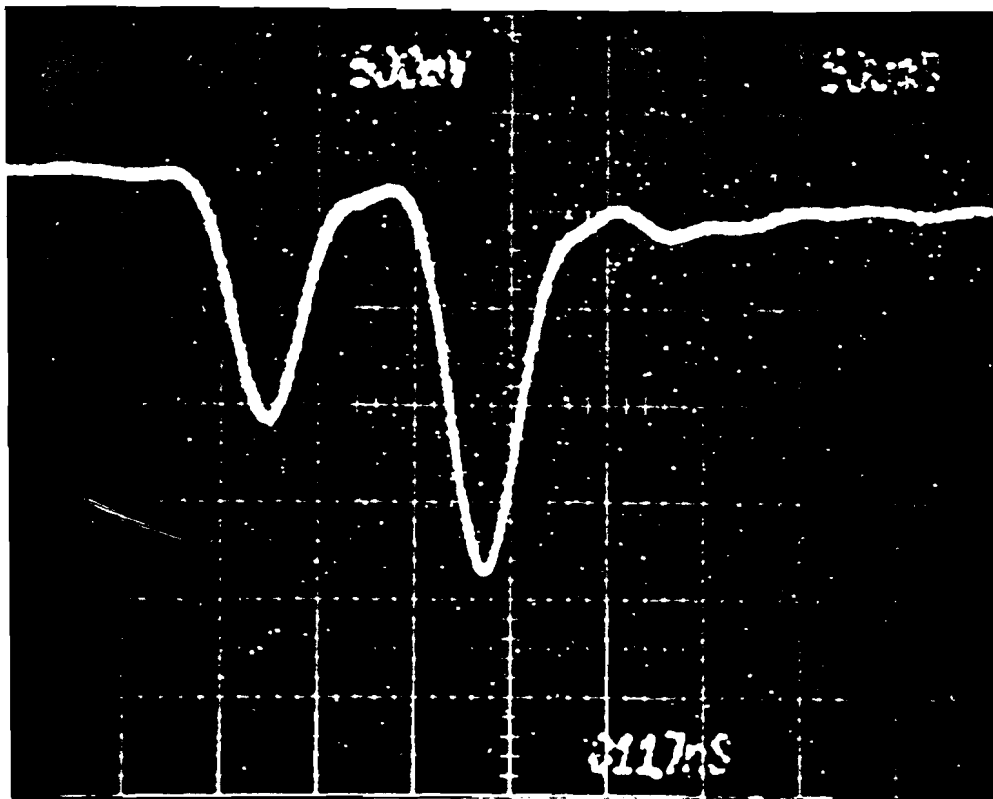


Figure IV.2



E912

Figure IV.3

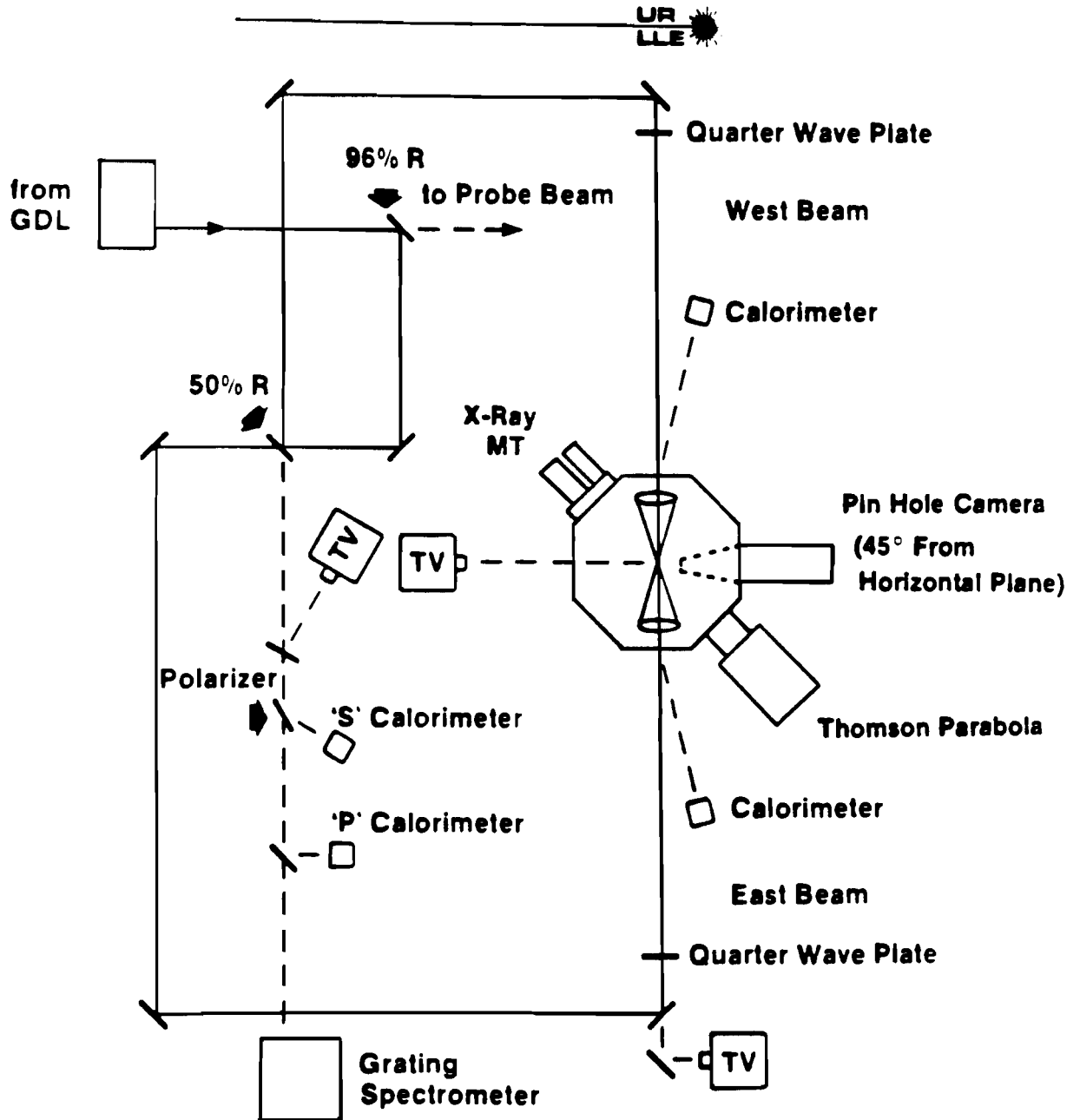
prepulse times were calculated from $t = 1.1 \text{ (nsec)} - 2d/c$, where $2d$ is the distance by which the path length was increased and c the velocity of light. Since the measurements of stage translation can be made to millimeter accuracy, the reproducibility of any prepulse setting is accurate to within a few picoseconds.

To make sure that there were no unintended prepulses propagating through the system, we monitored the prepulse contrast for no prepulse shots with a charged coupled diode and a 7401 Tektronics oscilloscope. The oscilloscope was set at prepulse level. The overdriving of the scope and destruction of the diode was prevented by inserting a water cell in front of the diode. The breakdown of the water cell due to the high intensity following the prepulse, made it opaque to the incoming main pulse, thus protecting equipment from destruction as well as making contrast monitoring easier.

Now a brief description of the target irradiation facility, also called Beta target interaction facility, will conclude this section. A schematic diagram is shown in figure IV4 with the diagnostics used in position.

As can be seen in the diagram, the incoming beam is split into two beams of equal strength by a 50% reflecting mirror. These beams are fed into the target chamber from opposing directions, east and west. F/2 aspheric lenses were used to focus these beams on the target. On most of the shots, the pin hole x-ray camera was used to measure the focal spot diameters on the target to allow calculation of the incident intensity. A streak camera with appropriate etalon was employed to measure full width half maximum of the laser pulse on each shot. The representative

"BETA" TARGET AREA



E786

Figure IV.4

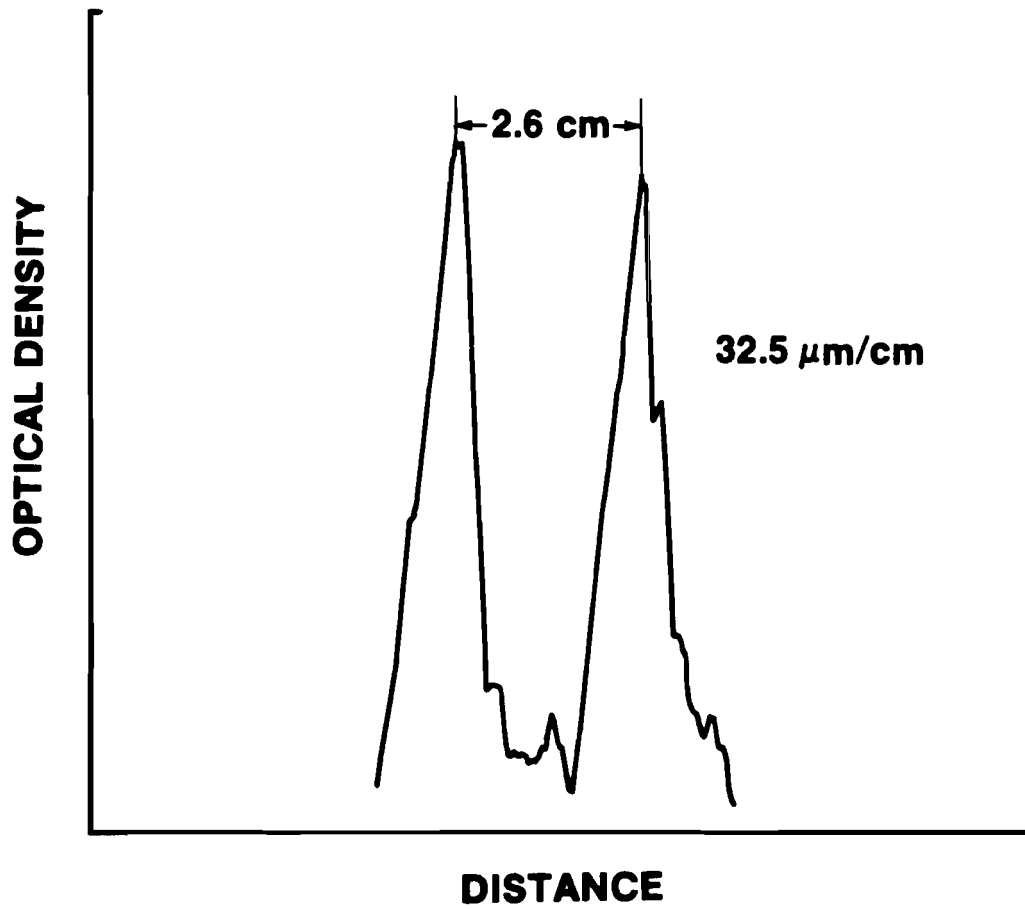
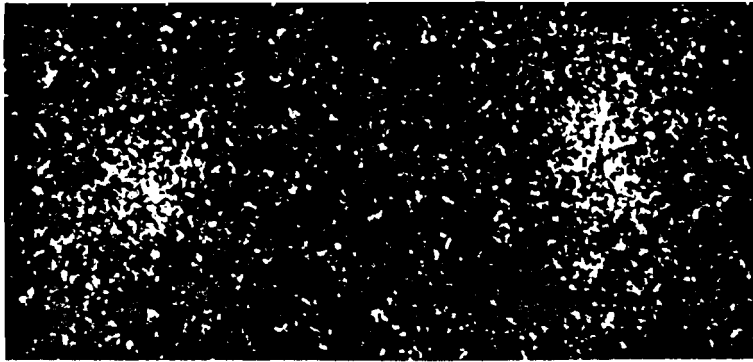
traces are shown in figure IV5 and IV6. Typical experimental conditions were as follows: Target; empty glass microballoon of approximately 80 μm diameter and 0.8 μm wall thickness, surface focus with focal spot diameter about 30 μm and intensities between 10^{15} to 10^{16} Watts/cm². As shown in the diagram IV4, laser calorimeters are placed at appropriate positions to measure the incident energy on the target. The alignment and the proper focusing on the target is done with a CW ND: YAG laser. A 50 μm correction is applied to the focusing lenses to compensate for the chromatic shift due to 100 \AA difference between YAG and phosphate glass lasing wavelengths.

C. Thomson Parabola

a. Introduction

There are a variety of plasma ion detectors available; the widely used ones are Faraday cup charge collectors, electrostatic mass spectrometer, magnetic ion spectrometer and Thomson Parabola. They vary widely in the method of operation, dynamic range, energy range and reliability. The choice of a particular instrument is usually dictated by the ion energy band of interest, resolution, dynamic range and reliability of measurement.

Charge collectors yield qualitative information about the asymptotic ion velocity distribution when placed far from the target at a measured distance. The ion current is measured with a simple conductor intercepting the plasma. The

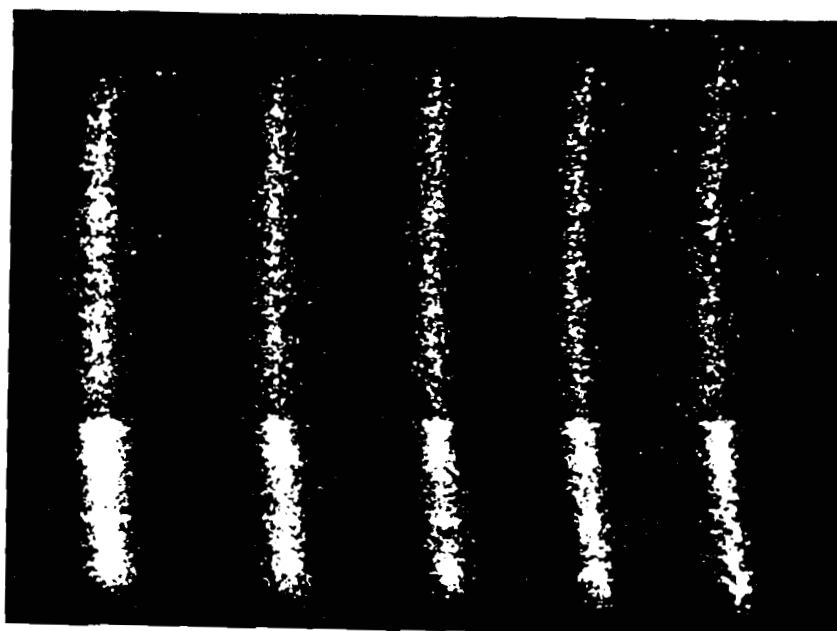
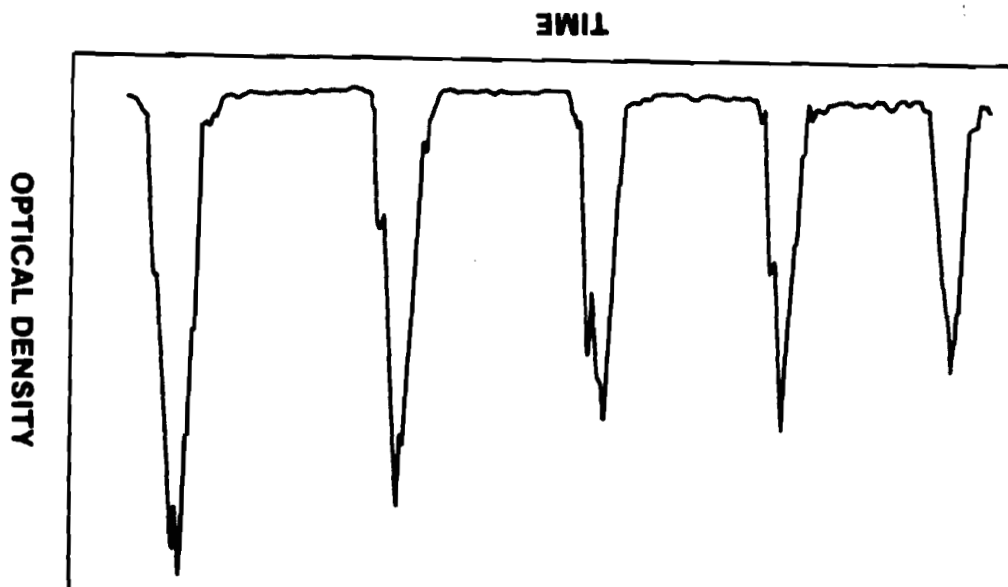


E1133

Figure IV.5

Figure IV.6

E1132



electrons are separated from the plasma by electrical biasing. The signal can be displayed on an oscilloscope. The distance of the charge collector from the target (ion flight distance) divided by the time of flight gives the ion velocity for the current distribution. The time of flight assumption is valid as long as the ion time-of-flight and flight distance between the target and the charge collection point remain respectively much larger than the characteristic emission times and dimensions of the ion source. In order to get the energy distribution, one needs to know the charge to mass (Z/M) ratio of the species in the multispecies plasma. Because of the inability of charge collectors to differentiate between ion species, they have to be used in conjunction with an ion mass spectrometer (which measures (Z/M)). Furthermore, because of the electrical measurement of ion current, there is a minimum ion flux that can be measured above the stray electrical noise of the system. This poses a problem for non-thermal ion measurement where the flux is quite low. For thermal ions, however, there is no problem. In addition, the time resolution is limited by the R-C time of the device and oscilloscope. The problem of secondary emission of electrons for ions striking the conductor and the questionable ability of the bias to separate high energy electrons from the incoming plasma, has made this device very controversial. However, because of their simplicity and small size they remain the conventional device used by most laboratories for measuring thermal ($< 10 \text{ Kev}/Z$) ions from laser produced plasmas.

An electrostatic mass spectrometer,^{4,5} on the other hand, measures (Z/M) ratios of the species and velocity distributions simultaneously. This is a parallel plate type device in which the entering ions are deflected in the same plane by an electric field. The method relies on time of flight separation of the ion velocity classes. During the expansion, the time of flight to the fixed position (of analyzer) L is related to the velocity v simply by $t = L/v$, provided that the ion generation time is negligibly small compared to L/v . By passage through the electrostatic analyzer, the ions are additionally selected on the basis of $v^2/(Z/M)$. The time of arrival at the ion detector is proportional to $(M/Z)^{1/2}$, the (Z/M) species are then identified by measuring the arrival time on a detector. Hence a detector located at a given point x on the detection plane will measure a set of points $(n, v, Z/M)$ where n is the number ions with velocity v and charge to mass ratio (Z/M) . By using several collectors in the detection plane, one obtains a sufficient number of such points to reconstruct the velocity spectrum of each (Z/M) state. By far the major drawback stems from the fact that one does not obtain the continuous measurement of ion velocities and, therefore, of the energies. The discrete velocity points for each (Z/M) state are limited to the number of collectors used. Furthermore, the resolution of (Z/M) states is limited by the frequency response of the electronics. (In essence, the continuous measurement of (Z/M) states and energy distribution is not possible with this device.) It is also useful to point out here, that in addition to the problems previously mentioned

because the device requires very high voltage to measure high energy ions the upper energy limit is typically 100 Kev/Z. Even this is an optimistic estimate because of the difficulties involved in measuring the low fluxes at these energies.

For the measurement of high energy ions (> 10 Kev/Z), a magnetic ion spectrometer^{6,7} with solid state track detector at the collection plane has been used. Uniform magnetic fields are produced by permanent or electromagnets. An ion deflects in a magnetic field according to its charge to momentum ratio. The dynamic range of the instrument is quite high (usually 100) and ions up to 1 Mev/Z can be measured. The deflection plane of an ion species is perpendicular to the magnetic field and the deflection of an ion specie is proportional to $(Z/M) \times (B/v)$. Therefore, the instrument gives the velocity distribution for a single ion species plasma. For a multispecies plasma, however, this instrument is not very useful. Moreover, the knowledge of the (Z/M) of the ion species is required in advance. However, the non-electrical nature of measurement makes the instrument more reliable. The ion tracks registered on the solid state detector are counted to yield a density distribution and the position of the tracks gives velocity distribution. The accuracy of the measurement may be challenged because of the assumptions made for the (Z/M) . Furthermore, it is difficult to vary the dynamic range of the instrument between the shots.

We chose the "Thomson Parabola" method of ion spectroscopy for its ability to analyze simultaneously the energy distribution of a wide range of charge to mass ratio ion species and its

high dynamic range (> 100). Here, advantage is taken of the properties of the electrostatic mass spectrometer and magnetic spectrometer by combining them together. Qualitative or quantitative data analysis can be done by employing a channeltron electron multiplier array (CEMA) or solid state track detector respectively in the detection plane. The data analysis in the later case is, however, very tedious. The complete description of the instrument and data analysis follows.

The name "Thomson" comes from the fact that J. J. Thomson⁸ in 1909 used this concept to disperse the electron beam in a cathode ray tube experiment. The "parabola" designates the trajectories of the charged particles, which under the influence of the parallel electric and magnetic fields of the instrument, trace out a parabolic shape on the film plane. The instrument's fields can be set to measure positively as well as negatively charged species. For this work we are interested to measure the positively charged species only. Solid state track detectors CR-39 (to be described later) were used with the instrument to register individual ions. Tracks are formed when energetic particles passing through the electrically nonconducting solid state track detectors, produce a narrow trail of radiation-damaged material which upon etching yields the track. Tracks can be enlarged to visual size by chemical etching. Hot alkaline solution, in this case, is a good etchant. A brief description of this process will be given later. The number of tracks registered gives the density distribution of particles. For known electric and magnetic fields the position of a track

gives the velocity and energy of a particle. The density distribution in either velocity or energy space can be deduced for the particles reaching the analyzer. For the first time we have extracted a quantitative measurement of density distribution according to the charge to mass ratios of the species.

Since the instrument measures the species according to the charge to mass ratio, care has to be exercised to make sure that the charge state of a species reaching the analyzer has not changed in flight. Change in charge state can occur by charge exchange or recombination with the background gas (during the flight path).

The probability of charge exchange is estimated⁹ as

$$P = \sigma n \ell \%$$

where σ is the charge exchange cross-section and is proportional to the charge state Z of the ions. For fully ionized glass, $Z = 10$ and σ is about 10^{-14} cm^2 .⁹ The detector to target distance ℓ is about 150 cm in our case, and $n = 2 \times 10^{10} \text{ cm}^{-3}$ (i.e., 5×10^{-7} Torr) is the density of the background gas. Therefore, the probability of charge exchange in our case is about $3 \times 10^{-2}\%$. It has been observed experimentally¹⁰ that charge exchange is significant at background pressures of 10^{-5} Torr and above. For example, it has been found (Ref.10) that when the background pressure was increased from 10^{-7} to 10^{-6} Torr, the fully stripped carbon ion (C^{+6}) signal was reduced by a factor of 3/4. It was reduced by as much as a factor of two for a background pressure of 10^{-5} Torr. When the background pressure was raised to 10^{-4} Torr and higher, the signal essentially disappeared. No change in signal was observed

when the background pressure was lowered below 10^{-7} Torr. Based on this experimental evidence, as well as the theoretical estimates done above, it has been inferred that at about 10^{-7} Torr, charge exchange is insignificant because of the small charge exchange cross-section.

Most of the previous experiments done at other laboratories, with background pressure greater than 10^{-5} Torr, have indicated that the acceleration of ion species is independent of their charge states. In other words, at maximum expansion velocities they have not only observed ion species with the highest charge state but also those with lower charge states. We believe that these results are influenced by the charge exchange of streaming ions with the background gas. For example, during the free streaming phase of the ions (i.e., after the acceleration is over) the charge exchange can transform some of the ions from their initial charge state to lower charge state without altering their velocities. In this case one would expect and observe the independence of ion acceleration upon its charge state. This, therefore, does not unravel the real dynamics of plasma acceleration.

We made an effort to keep our background pressure (both in the target chamber and the instrument) at or below 3×10^{-7} Torr where experiments¹⁰ have shown no signature of charge exchange. Surprisingly, we have found different charge species accelerated to different maximum velocities. We believe this will give a better insight in the acceleration process of the plasma.

b. Instrument description

The instrument is comprised of three parts, as shown in figure IV7; an aperture system, a deflection sector and a recording plane where the incoming particles end up making tracks. We will discuss the deflection sector first and then we will end this section with a discussion of aperture effects and a description of the film plane. A sectional sketch of the instrument is shown in figure IV7A.

The analyzing sector consists of two mild steel (magnetic steel) plates connected to, but electrically insulated from an electromagnet. These plates are mounted in an aluminum housing. The electromagnet produces a nearly homogeneous magnetic field between, and transverse to, the plates. The magnetic field can be readily adjusted by changing electrical current to the electromagnet. An electric field parallel to the magnetic field is established by biasing one plate relative to the other grounded one. The plates were made much longer (15 cm) and wider (5 cm) than the plate separation (1.75 cm) to minimize the effect of end fringing fields in comparison with the working fields within the gap. Inside the analyzer particles undergo deflection under the influence of electric and magnetic fields. These deflections are proportional to charge/energy and charge/momentum ratios respectively. Upon leaving the analyzing sector, the particles travel along straight trajectories. The particle trajectories can be analysed as follows:

Plasma entering through aperture a_2 (defining aperture, see

CROSS SECTIONAL VIEW OF THOMSON PARABOLA

UFR
LLE

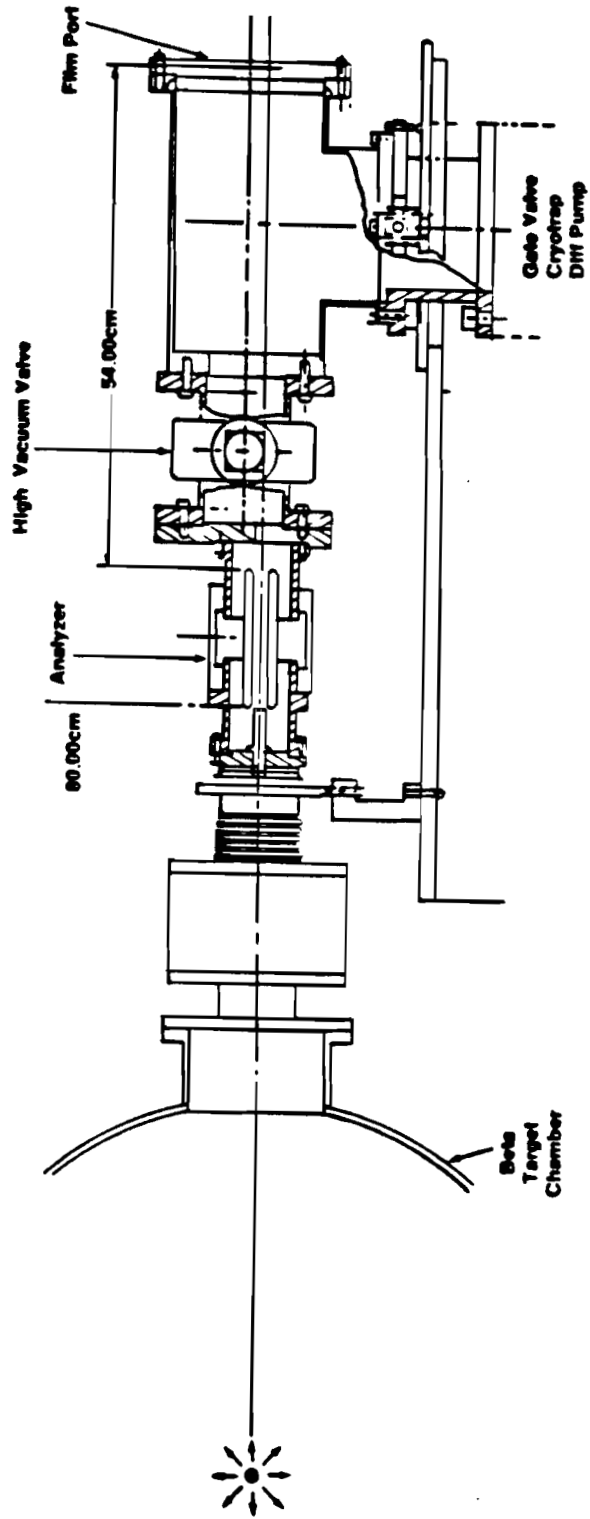


Figure IV.7A

THOMSON PARABOLA

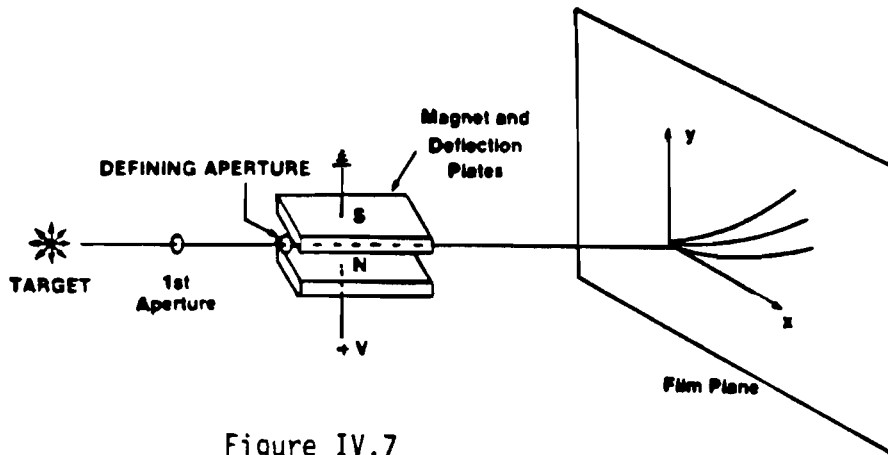


Figure IV.7

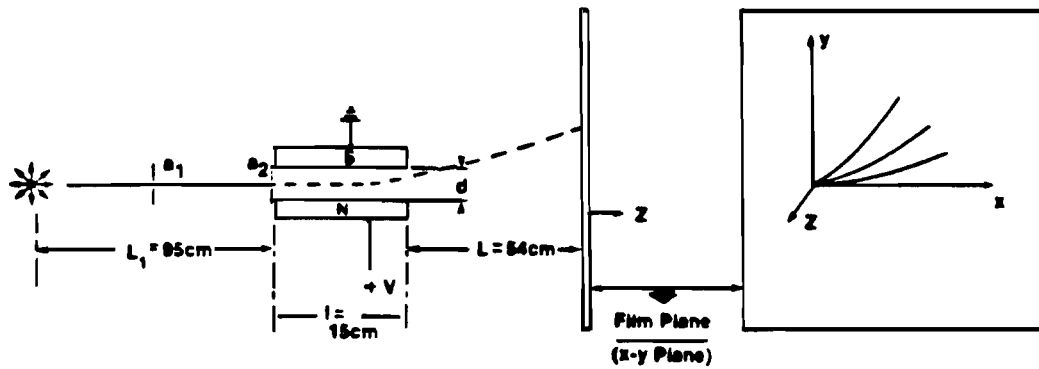
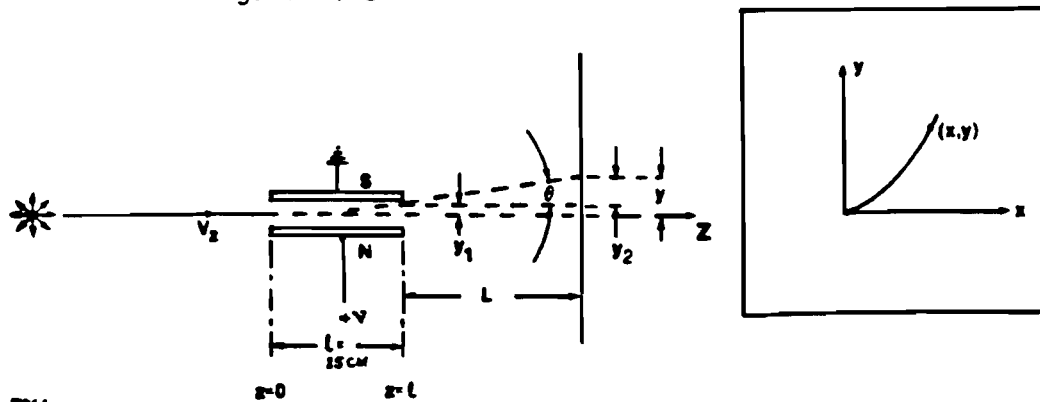


Figure IV.8



8014

Figure IV.9

figure IV8) undergoes ion and electron separation under the influence of electric and magnetic fields, which are parallel to each other and perpendicular to ion motion (z-direction).

Referring to geometry in figure IV8, and using MKS system of units, the equation of motion in the y-direction due to electric field E_y is,

$$M_i \frac{dv_y}{dt} = ZeE_y \quad (IV-1)$$

M_i = Ion Mass, v_y = velocity in y-direction

Z = charge state of the ion.

The equation of motion in the x-direction due to the magnetic field

$$\begin{aligned} M_i \frac{dv_x}{dt} &= Ze(\underline{v} \times \underline{B})_x \\ &= Zev_z B_y \end{aligned} \quad (IV-2)$$

v_x = velocity in x direction

v_z = velocity in z direction (initial direction of motion)

B_y = magnetic field in y-direction

Integrating equation (1) twice with respect to t , we get the deflection in the y-direction due to electric field

$$y = \frac{ZeE_y}{M_i} t^2/2 \quad (IV-3)$$

Here it has been assumed that at time $t = 0$, velocity $v_y = 0$.

Now integrating equation (2) twice with respect to t , we get the deflection due to the magnetic field in the x -direction to be

$$x = -\frac{Ze v_z B_y}{M_i} t^2/2 \quad (\text{IV-4})$$

Again here it has been assumed that at $t = 0$, velocity $v_x = 0$.

Upon leaving the analyser the particles move in a straight trajectory. The combined effect at the film plane at a distance L can be calculated.

If the particle is moving in the z -direction with velocity v_z , the time taken to travel through a distance ℓ is

$$t = \ell/v_z$$

Substituting this in equation (3)

$$y_1 = \frac{Ze E_y \ell^2}{4E}$$

$$E = 1/2 M_i v_z^2 = \text{kinetic energy of ion in } z\text{-direction.}$$

The slope of the trajectory at $z = \ell$ (see figure IV9)

$$\left. \frac{dy_1}{d\ell} \right|_{z=\ell} = \left(\frac{Ze E_y}{4E} \right) 2\ell$$

$$\text{Therefore } y_2 = L \left. \frac{dy_1}{d\ell} \right|_{z=\ell} = 2\ell L \left(\frac{Ze E_y}{4E} \right)$$

The final position y on the film plane is

$$y = y_1 + y_2$$

$$= \frac{ZeE}{4E} y (\ell^2 + 2\ell L)$$

$$\text{or, } y = \frac{ZeE}{M_i v_z} \frac{y \ell}{2} (\ell/2 + L) \quad (\text{IV-5})$$

Similarly the deflection due to the magnetic field from equation (4) is

$$x_1 = \frac{ZeB}{2M_i v_z} y \ell^2$$

and,

$$x_2 = \frac{ZeB}{M_i v_z} y \ell L$$

the total deflection in the film plane is

$$x = x_1 + x_2$$

$$x = \frac{ZeB}{M_i v_z} y \ell (\ell/2 + L) \quad (\text{IV-6})$$

Combining equations (5) and (6) eliminating v_z

$$y = \left[\left(\frac{E_y}{B_y} \right) \left(\frac{M}{Z} \right) \frac{1}{[e\ell(\ell/2+L)]} \right] x^2 \quad (IV-7)$$

Equation (7) is an equation of a parabola. For a fixed geometry of the instrument and given values of electric and magnetic fields, equation (7) suggests that each discrete value of (M/Z) will produce an unique parabolic trace with the highest energies closest to the origin, $x = y = 0$. Also equations (5) and (6) indicate that the y axis is the energy axis and the x -axis is the momentum axis.

The trajectory of constant velocity (v_z) in the detection plane can be found by simply dividing equation (5) by equation (6) which gives

$$y = \left(\frac{E_y}{B_y} \right) \left(\frac{1}{v_z} \right) x \quad (IV-8)$$

Therefore, the trajectory of constant velocity is a straight line with slope $[(E_y/B_y) \times (1/v_z)]$.

The instrument used has the following dimensions, $L_1 = 95$ cm, $\ell = 15$ cm, $L = 54$ cm, $d = 1.75$ cm, the first aperture $a_1 = 1000$ μm and defining aperture $a_2 = 200$ μm .

Choice of field strengths (design parameters)

We are interested in observing ions with velocities between 10^8 cm/sec and 10^9 cm/sec (10 Kev/Z to 1 Mev/Z for average SiO_2 ions. The choice is dictated by the fact that the lower limit is set by the

film sensitivity (to be discussed later) and the upper limit is set arbitrarily with the assumption that the highest velocity ion will have a velocity below this. In case the observation is to the contrary, the field strength can be adjusted to accommodate higher energy ions.

Electric and magnetic fields are chosen such that the high energy ions (in this case 1 Mev/Z) have appreciable observable deflection. We tend to assign this deflection in order to calculate required field strengths. We estimate that a deflection of the order of 0.5 mm is observable. To demand a deflection of this order, we estimate from equations (5) and (6), electric and magnetic fields of approximately 140 V/cm and 100 gauss respectively. This will provide an x-deflection of 4.5 cm and y deflection of 6 cm for the lowest energy ions, which will essentially govern the size of the film.

Magnetic fringe field effect

The equations obtained so far assume that fields are uniform within their boundaries and vanish elsewhere. In practice, the deflections are determined by the line integral of the fields along the line paths. In the absence of an ion source to calibrate the analyzer, one design goal should be to minimize the stray fields and the fringing fields on ion trajectories. This can be done by maximizing the ratio of the length of the electrode to the separation (gap) between the electrodes. In this case it was approximately 4.35.

It is well known that the magnetic field lines between the iron pole faces, tend to converge towards sharp edges, giving rise to maxima in field strength. The edge effect has been discussed extensively¹¹ in connection with electrostatic and magnetic problems. A guideline to reduce the fringing effect has been proposed which suggests the rounding off of the sharp corners to the radius of

$$r = \frac{3\sqrt{3}d}{2\pi} = 0.83d = 1.45 \text{ cm}$$

where d is the gap between electrodes (1.75 cm). This is also known as Rogowski pole shape.¹²

Care was exercised to bring the fringing field effect to a minimum in the instrument by shaping the electrode edges to the Rogowski pole shape.

C. Resolution

The deflection method employed in the analyzer does not exhibit any of the focusing properties associated with many type of mass spectrometers. The resolution is determined by the size and the angular divergence of the incident beam and by space charge effects subsequent to collimation. A single aperture can be used to produce a collimated beam from a true point source. Since a laser heated target forms an expanding sphere of plasma, a single aperture would have to be placed inconveniently far from the target to ensure a well collimated beam. For convenience we

chose a two-aperture system, with defining aperture of 200 μm nearest to the analyser.

The entrance pin hole size of the analyser must be less than the Debye length λ_D ($\approx 7.43 \times 10^2 \times T_e^{1/2} \times n^{-1/2}$ cm, T_e in eV) of the incoming plasma so that the electrons can be separated from the ions upon entering the analyser. In our case the pin hole diameter was 200 μm , whereas the Debye length was approximately 740 μm ; here the plasma has been assumed to have cooled to room temperature during expansion (i.e., $T_e \approx 1/40$ eV) and the density of the plasma n is approximately $10^7/\text{cm}^3$ (from measurement).

Space charge expansion of the ion beam inside the analyser imposes some problems in commonly used particle spectrometers. The expansion of a mono energetic ion beam with an initial radius r_0 (cm) diverges due to space charge to¹³

$$r_1 = \frac{r_0 s_1 e z n^{1/2}}{\sqrt{2} (\epsilon_0 E)^{1/2}} \quad (\text{IV-9})$$

where, r_1 = divergence after distance s_1 (cm)

E = ion energy (eV)

Z = charge state, e = electronic charge (e.s.u.)

$\epsilon_0 = 8.85 \times 10^{-12}$ and n = density ($\#/\text{cm}^3$).

The angular divergence θ is given by r_1/s_1 .

To minimize this effect the aperture is placed far enough away so that the density is low. In our case the diameter of the beam at the film plane after space charge divergence is estimated to be 300 μm (for $n \approx 10^7 \#/\text{cm}^3$, $Z = 8$, $E = 10 \text{ Kev}/Z$). Because the lowest

detectable ion energy was used for calculation, this is the most conservative estimate of space charge. Notice from equation (9) that the divergence due to space charge becomes smaller at higher energies. Moreover, this effect was experimentally checked by measuring the width of the parabolas on the film. If the width is confined to the geometrical divergence a_3 , which in this case is given by

$$a_3 = \frac{a_2}{L_1} (L + \ell + L_1) \quad (\text{IV-10})$$

and estimates to approximately 350 μm , then space charge effects are not present. Any broadening in addition to the geometrical effects will indicate the presence of space charge effects. In our case no such problem was found to be present. The width of the parabola was approximately 344 μm .

Therefore, the resolution is solely dominated by the geometrical divergence of the beam. The uncertainty in charge to mass ratio and the velocity at the extreme ends of the parabola (highest and lowest energy ends) can be determined with the help of geometry of figure IV10 and equations (11) and (12)

$$y = \left(\frac{E_y}{B_y} \right)^2 \left(\frac{M}{Z} \right) \left(\frac{1}{K} \right) x^2 \quad (\text{IV-11})$$

$$\frac{x}{y} = \left(\frac{B_y}{E_y} \right) v \quad (\text{IV-12})$$

where $k = e\ell(\ell/2 + L)$

THOMSON PARABOLA

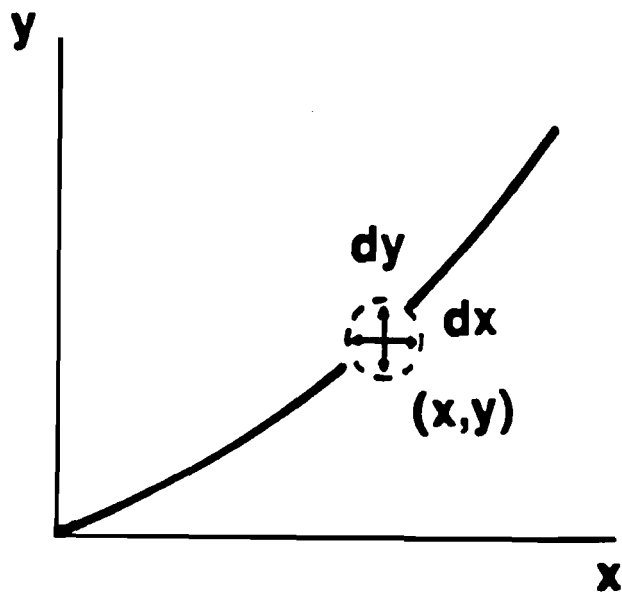


Figure IV.10

E913

From equation (11)

$$\frac{d(Z/M)}{(Z/M)} = 2 \frac{dx}{x} - \frac{dy}{y} \quad (\text{IV-13})$$

Here, dx and dy are the widths of the parabola in x and y directions respectively (figure IV10). If the point (x,y) is chosen at the center of the parabola (ideal curve), the deviation from the ideal curve (because of the finite width of the parabola) in x and y directions could be $\pm dx/2$ and $\pm dy/2$ respectively. Therefore, realistically the resolution of (Z/M) (equation 13) should be represented as

$$\frac{d(Z/M)}{(Z/M)} = \pm \frac{dx}{x} \mp \frac{dy}{2y} \quad (\text{IV-13A})$$

and a conservative estimate is obtained by keeping the signs of dx and dy the same. In our case $dx = dy = 400 \mu\text{m}$ and for high velocity oxygen ions (10^9 cm/sec) typically $x = 2.5 \text{ mm}$ and $y = 1.3 \text{ mm}$. Therefore at high energy end of the spectrum the resolution of (Z/M) from equation (13A) is 31%, whereas at the low energy end the resolution improves to 3.5%.

The velocity resolution is determined from equation (12) which with the help of equation (7) yields

$$\frac{dv}{v} = \frac{dx}{x} - \frac{dy}{y} \quad (\text{IV-14})$$

Here again, the center of the parabola being at (x,y)

(figure IV10), the deviation from the ideal curve (center curve) could be up to $\pm dx/2$ and $\pm dy/2$ in x and y directions respectively. Therefore, the velocity resolution from equation (14) should be represented by

$$\frac{dv}{v} = \pm \frac{dx}{2x} \pm \frac{dy}{2y} \quad (\text{IV-14A})$$

For the conservative estimate, we keep the signs of dx and dy the same. This then gives the velocity resolution of 23% at the high velocity end (10^9 cm/sec) and that of 1.9% at the low velocity (10^8 cm/sec) end of the spectrum.

As can be inferred from these estimates, one's resolution of velocity and (Z/M) at high energy end is limited. Higher the energy of a particle, the smaller is its deflection for a given set of electric and magnetic fields (equations 5 and 6) and their resolution of (Z/M) and velocity becomes poorer (equations 13A and 14A). Furthermore, at high energy end, the parabolas converge to the same origin (equation 12) and become indistinguishable, as a consequence a poor resolution results. On the other hand, low energy particles have large deflection and the parabolas are well separated, therefore, a better resolution is expected and obtained.

Fortuitously, our data was not subjected to the same poor resolution as estimated above for the high energy end of the spectrum. This is because we did not observe the oxygen ions up to the highest measurable velocity (10^9 cm/sec). For example, oxygen (O^{+8}) ions had the highest velocity of $5-6 \times 10^8$ cm/sec and typical deflections

of $x = 11$ mm and $y = 5$ mm. The resolution of (Z/M) from equation (13A) comes out to be 7.6%. The difference in (Z/M) between O^{+8} and O^{+7} is 12.6% and therefore there was no uncertainty in distinguishing O^{+8} from O^{+7} at high energy end. In case of protons the typical high energy end deflections were $x = 13$ mm and $y = 2.5$ mm, giving us a resolution in (Z/M) of 11%, whereas the difference in (Z/M) between protons and O^{+8} is 50%. Similarly, the velocity resolution was also very good in our case. For example, at high energy end for O^{+8} it was 5.8% and for protons it was 9.5%. Furthermore, our parabolas were quite distinguishable at the high energy end of the spectrum.

d. Sensitivity

The sensitivity of the instrument depends upon the type of the detecting medium employed. For the measurements pertaining to this thesis work, we are interested in measuring light ions (protons) from 50 Kev to a few Mev and heavy ions (like silicon, oxygen, carbon, etc.) from 10 Kev/Z to about 1 Mev/Z. We chose a solid state track detector called CR-39¹⁴ (allyl diglycol carbonate). CR-39 is commercially available, optically clear, amorphous, thermoset plastic in which charged particles' tracks can be revealed by etching in a hot NaOH solution. The material is sensitive to record light ions (protons) above 25 Kev and heavy ions above 10 Kev/Z¹⁵. The variation of the uniformity of response of this material is <1%. The superb optical quality of the material makes it ideal for the identification of mass and charge of charged particles.

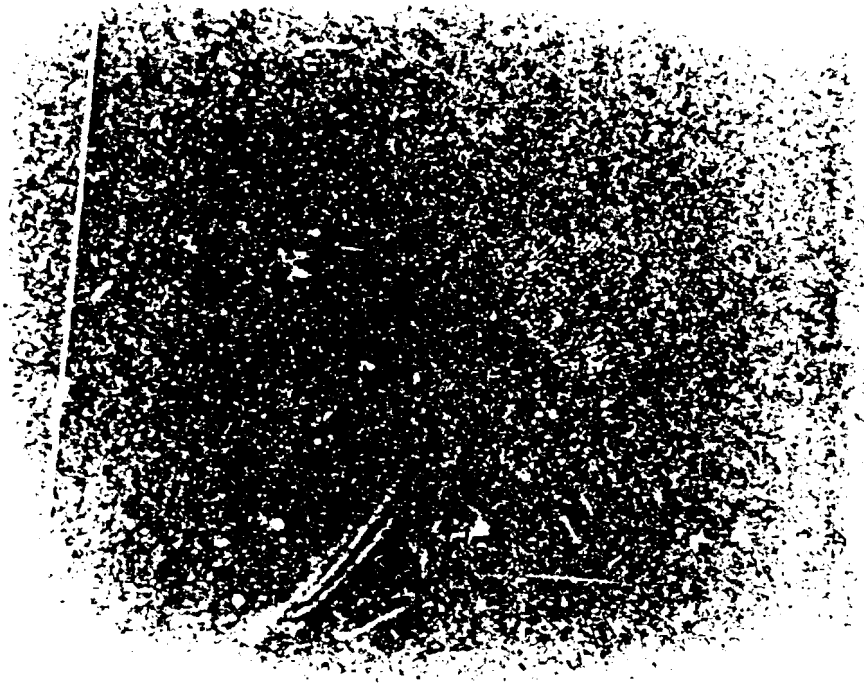
In an organic polymer such as CR-39, tracks are formed when the charged particle ionizes and excites molecules, breaking the cross link, i.e., chains. The chain ends form new species which are highly reactive chemically.¹⁶

When etched with an alkaline solution under appropriate conditions, the etch rate is higher where the cross link is broken compared to the bulk of the material. Each track is seen under a microscope, as a round conical indentation. The size and depth of these tracks depend upon the velocity and the charge state of the particles. Each particle hitting the surface of the material forms a track.

We etched the exposed film with a 6.25 N NaOH solution at 55°C for 24 hours. This resulted in uniform, round and well isolated particle tracks.

e. Data reduction

We indicated earlier that particles are confined to a parabolic trajectory on the film plane according to their charge to mass ratios. The position of the particles on the parabola indicates the energy with which particle entered the analyzer. Figure IV11 is a picture of the etched film showing the parabolas as would be seen by the naked eye. Under a microscope with proper magnification these parabolas are made up of a large number of individual round tracks formed by the charged particles. To quantify the density distribution one needs to count millions of these tracks. Needless to say it is not only a very tedious but also very time consuming



E912

Figure IV.11

process. Sometimes it is classified as a next to impossible task and this has resulted in the fact that nobody had yet unraveled full quantitative information from these measurements.

Most of the laboratories have used channeltron electron multiplier array¹⁷⁻¹⁹ (CEMA) as a detector for experiments involving the "Thomson Parabola". This registers ion density on a polaroid film. The way it works is that the output of CEMA is used to excite a phosphor, the output of which is then recorded on the film. The output of CEMA-phosphor does not allow one to ascertain absolute (or relative) number of particles impinging upon it. Although it is a very good method to obtain quick qualitative information, quantitative information requires calibration of the CEMA in the energy and charge spectrum of ion species. The only calibration source of such type, as we know, is laser plasma itself. In the absence of a calibration, we believe, quantitative measurement is not possible.

Dr. C. Joshi, et al.,²⁰ at National Research Council (Canada) have developed an optical fourier transform technique (OFT) to quantitatively assess the density of ion tracks on cellulose nitrate film. Ion tracks on the film are confined to a rectangular two-dimensional array by placing an electro-etched nickel mesh over the film during the exposure. Noise on the film is assumed uniform and randomly distributed. This imposed periodicity in the signal allows one to separate the film noise from the signal by suitably masking the Fourier transform of the film. The contrast enhanced image so obtained is digitized by a scanning vidicon to yield ion

density on the film. Besides requiring a lot of instrumentation, the technique demands a good calibration and optimization of mesh size for each shot (i.e., ion density). Thus, for only those shots, in which the mesh size is optimum for the density (to make a clear straight diffracting edge), data can be analysed. Besides this selective nature of data processing, the quantitative information obtained is also questionable. The method clearly fails for very low density (no clear diffracting edge) and very high density (diffracting edge formed by overlapping tracks) on the film. Again, we feel this method may yield good qualitative information, but is not worth the effort. In order to use this instrument effectively, i.e., to do quantitative measurements, one needs to develop good, reliable and less tedious data reduction process.

For the first time we attempted to extract the full quantitative information from these measurements. Obviously we did not choose to do so by manual counting under a microscope. Instead, we used a feature analysis system called "Omnicon" at Los Alamos Scientific Lab., which was modified to suit the specific needs of track counting. It is commercially marketed by Bausch and Lomb.

"Omnicon" is essentially a pattern recognizer. A microscope is coupled to a display system with a vidicon camera. The system is calibrated to different optical densities (grey scale range). With the help of appropriate software and microprocessors, it determines the boundaries of the feature by sensing the change of the phase of the grey level. A detailed description of the system is given in Ref. 21.

The image of the specimen, the results of the analysis and a variety of messages, appear on the TV-like display. The specific area in the image to be analysed (the field of measurement) is indicated by a frame, the position and the size of which can be varied by the operator. Within a field it is possible to perform measurements:

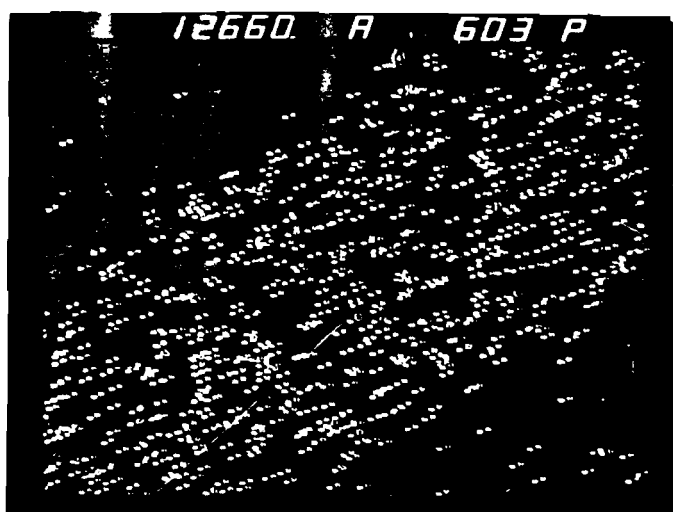
- on all individual features in the field
- only on the features selected by the operator
- on all features lying within a range of size and shape specified by the operator.

Measurements include:

- total count of all features
- length (diameter)
- perimeter
- areas of the features.

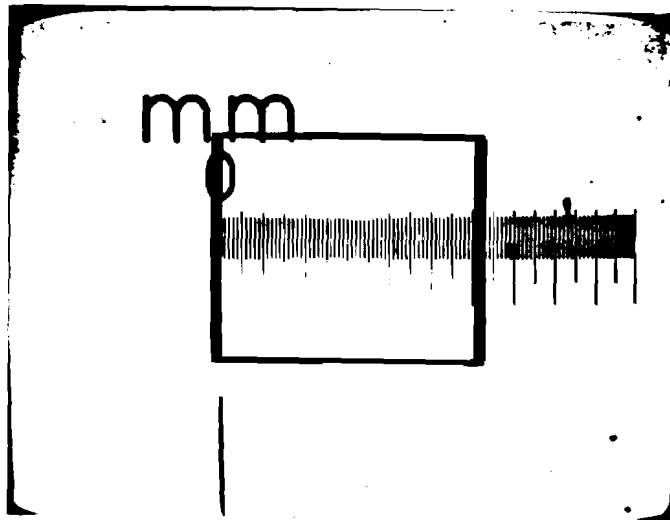
A typical display of our film is shown in figure IV12. The frame shows the field of measurement. The procedure we followed for the data reduction is as follows.

We set the magnification of the microscope to make the tracks distinct. In this case it was 120 x. The size of the field of measurement (frame) was measured with a calibration scale (figure IV13). Then with the help of x-y translation stage of the microscope the field of measurement frame is moved along the parabolas from one end to the other, at each point the machine displays the number of tracks on the screen. The x-y co-ordinates are noted from the translation stage. The same process is repeated for



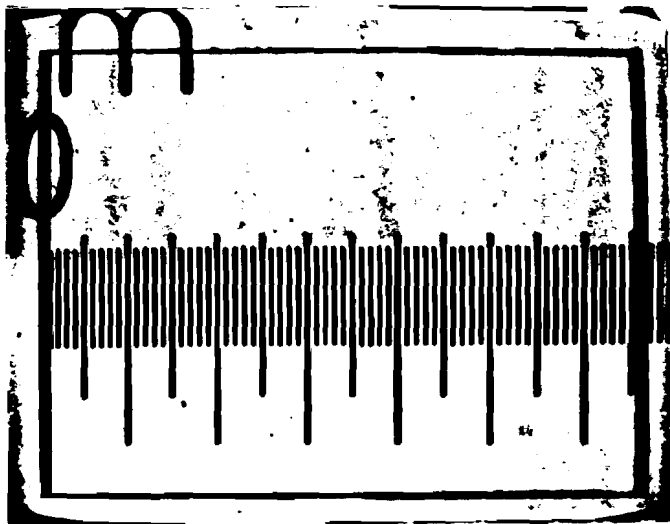
E911

Figure IV.12



1 div = 10 μm

4X



1 div = 10 μm

10X

E910

Figure IV.13

all frames on each parabola and for all parabolas. In principle one can program the automatic translation stage to follow a given equation of curve, this feature was not operational.

Ideally one would like to take as small a frame as possible for better resolution of velocity and count the number of tracks of each successive frames without overlapping them. We chose our frame size to be $600 \mu\text{m} \times 600 \mu\text{m}$. For known (Z/M) and using equation (6), we estimated the velocity resolution (dv/v) for the size of the field of measurement chosen. Equation (6) gives,

$$\frac{dv}{v} = - \frac{dx}{x} \quad (\text{IV-15})$$

Here dx = width of the frame in x direction ($600 \mu\text{m}$). The velocity resolution at the high energy end estimates to 6% and at the low energy end to about 1.2%. Sampling of the successive frames was not deemed necessary as the density of the tracks was found to be slowly varying in adjacent frames. Moreover, the large number of frames greatly increase the data reduction time.

For each frame of measurement (figure IV12), we get a set of points (x,y,N) where x and y are the x and y co-ordinates respectively of the center of the frame and N is the number of tracks between the points x_1 and x_2 , the width of the frame in the x direction. The velocity band dv is determined by using the equation (6) for known (Z/M) . It is useful to mention here that the film plane of the instrument provides on each shot a set of reference axes. These axes are parallel to the axes of measurement (formed with the origin on the line of

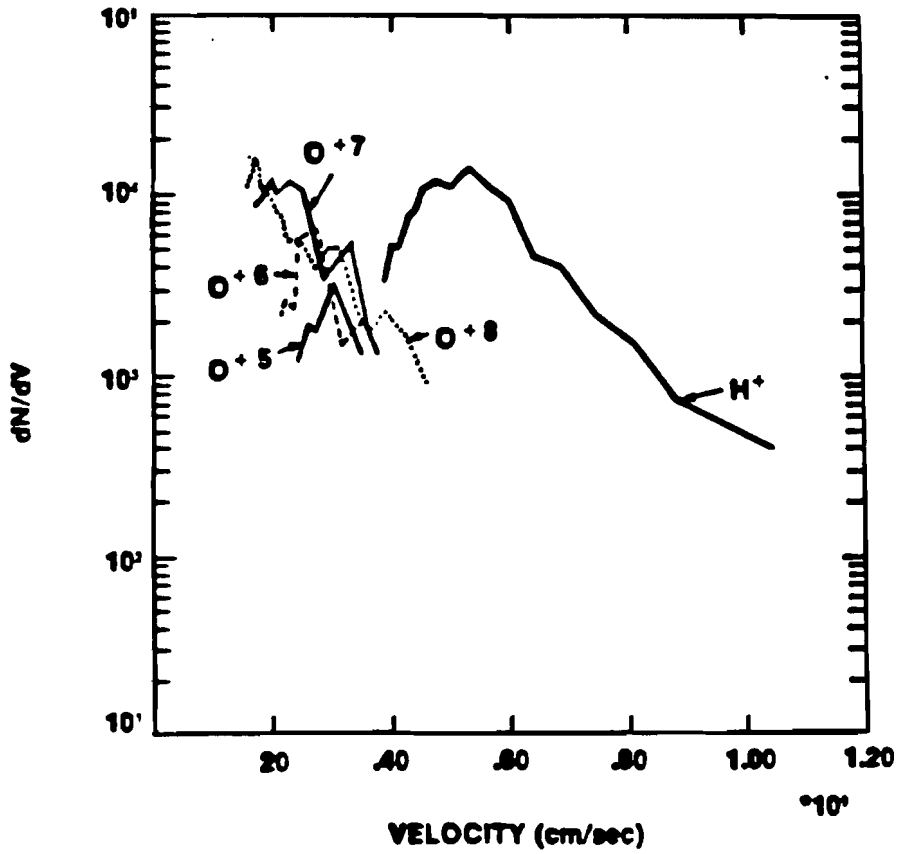
sight of the target) and are off-set from them. This off-set was determined by marking the axes of measurement. This was done by the double exposure of a film, from two target shots with only one field (electric and magnetic fields respectively) on at a time. In all shots, track positions were measured from reference axes, and compensated for the off-set during data analysis. In general, these measured parameters were fed into the data analysis computer. The data reduction program (attached at the end of this thesis) exploits equations (5) and (6) to yield charge to mass ratio of the species and their velocity distribution. An ion density plot in velocity space, generated by the computer, is shown in figure IV14. The plots can be properly integrated to yield total number of particles of each species and their total energy content. These then, can be summed to give the total number of particles entering the analyzer and the total energy contained in them.

f. Problems and errors

The main problem in this type of measurement is that of quantitative analysis of the data. Pattern analysers are very expensive and the manual method is extremely cumbersome. The Thomson analyser is not compact and has to be kept far away from the plasma source, where densities are sufficiently low that any space charge effects are negligible. This makes the instrument less versatile.

There are several possible sources of errors in analysing Thomson Parabola data. The effect of field modulation in the

ION SPECIES DENSITY DISTRIBUTION AS A FUNCTION OF VELOCITY



E1034

Figure IV.14

analyser and the unstable ground potential (sometimes) gives rise to wiggles in the parabolas. At the high energy end, where all the parabolas are converging to the same origin, their separation becomes less distinct. This, compounded with the wiggling effects of the parabolas brings additional uncertainty in the knowledge of the charge to mass ratios and energies of the particles. Extreme care has to be exercised to prevent this. In our case, minimization of ground loops prevented this.

Although the magnetic field of the electromagnet is calibrated for the input current, the retentivity of the magnetic field in the magnetic material makes it difficult to predict the magnetic field exactly at a later setting. One way to handle this problem is to probe the magnetic field in the analyser all the time, which is by no means a simple task. Interestingly, a simple visual observation of all the parabolas on the film provides a definite identification of the one corresponding to protons. This is because the protons have $Z/M = 1$, which is much higher than Z/M of other species (e.g., O, Si, C etc.), which have Z/M of 0.5 and less. Therefore, the protons have an x deflection (equation (6)) much higher than other species and this enables one to identify a proton parabola very easily. Analyzing the proton parabola and assigning the value of $Z/M = 1$, we can calculate the line average of the magnetic field (B_y) exactly from equation (6). The magnetic field value so calculated has been found to differ from that of earlier measured values by as much as 10%. The electric field is known to an accuracy of 2% (power supply accuracy). The field values estimated this way increase the

accuracy of the identification of the charge to mass ratios of other species.

The number of tracks in one frame is usually about 200. Assuming this to be a purely random sample, the standard deviation is 14.14. This gives an uncertainty of $\pm 7.07\%$ in the number of counts. This is increased somewhat if we use the pattern analyzer. There, some scratches or noise in the film are also counted as a feature if they happen to fall within the counting threshold. We calibrated the analysis by counting tracks with both the microscope and the image analyser and found this to be a negligible error ($< 2\%$).

V. EXPERIMENTAL RESULTS AND DISCUSSION

The results of a non-thermal ($> 10 \cdot \text{Kev/Z}$) ion density distribution measurement are summarized in Table I and II. For each shot listed in Table I, the hot electron temperature (T_e), fraction of target mass in non-thermal ions, fraction of incident energy in ions, ion sound speed (C_s) and maximum expansion velocity V_T ("ion front" velocity) were determined. These are listed in Table II.

For the underlined shots in Table I, we did not detect non-thermal ($> 10 \text{ Kev/Z}$) ions, which we believe signifies the energy threshold on the target for the production of non-thermal ions. Interestingly, we find that the energy threshold is higher in case of prepulse on the target, compared to the no prepulse case. For example, from Table I we infer that for 300 psec prepulse with relative amplitude of 10^{-2} to the main pulse, the energy threshold is about 1.68 Joules, which is lower than for an 1100 psec prepulse for which the threshold is around 2.6 Joules. When there is no prepulse on the target, the threshold is in the neighborhood of 1.14 Joules, which is lower than for either of the prepulse cases. The conclusion from this is that a no prepulse plasma is more conducive for the production of non-thermal ions.

The intensities on the target were varied from 10^{15} to 3×10^{16} w/cm^2 . Empty glass microballoons of nominally 80 μm -diam and 0.8 μm thickness were used as targets. For a fixed laser intensity ($\sim 2 \times 10^{15}$ w/cm^2), we varied the intensity ratio (contrast ratio) of prepulse to main pulse, from 10^{-2} to 10^{-6} . In the plots, 10^{-7} is defined as the no prepulse case. For each amplitude ratio, two settings of the relative timing

TABLE I

Energy on the target (Joule)	No Prepulse	Contrast Ratio				
		10 ⁻²	10 ⁻³	10 ⁻⁴	10 ⁻⁵	10 ⁻⁶
12-10	4242(10J)	4294(10.6)B				
	4283(11.3J)					
8-6	4291(6.63J)	A4404(7.64)				
4-6	4401(5.92)	4397(5.52)A				
		4405(4.67)A				
		4288(6.7)B				
		4292(6.24)B				
		4287(5.92)B				
2-4	4296(3.2)	4414(2.96)A	4378(3.62)B	4422(2.4)B	4418(2.8)A	4424(2.68)B
	4297(3.2)	4389(2.0)A	4423(2.35)B	4417(2.24)A	4385(2.08)B	4387(2.44)B
	4376(3.0)	4295(3.2)B		4383(2.24)B		4419(2.3)A
	4386(2.54)	4377(3.0)B				
	4374(2.26)	4425(2.6)B				
		4320(2.02)B				
Below 2	4318(1.68)	4415(1.68)A	4416(1.84)A		4421(1.08)	
	4352(1.14)	4398(1.18)A				
	4290(1.1)	4357(1.84)B				
	4354(0.74)	4299(1.72)B				
	4317(0.6)	4319(1.28)B				
		4355(0.92)B				
		4356(0.92)B				

Prepulse A - 300 psec

B - 1100 psec

Shot numbers are shown in each column. The figures in parenthesis show the actual energy on the target in Joules and the letter at the end shows the nature of prepulse.

TABLE II

Shot #	Intensity W/cm ²	Hot electron temp. Tev (Kev)	Fraction of incident energy in ions (%)	Fraction of target mass in ions	"Ion front" (VT) velocity (cm/sec)	Ion-sound speed $C_s = \sqrt{ZT_e/M}$	V_T/C_s
4242	3.0×10^{16}	37.1	25.74	1.35	1.59×10^9	1.92×10^8	8.28
4283	3.5×10^{15}	5.1	1.64	0.34	9.72×10^8	7.13×10^7	13.63
4287	5×10^{15}	9.44	7.86	0.45	9.97×10^8	9.7×10^8	10.27
4288	7.3×10^{15}	8.5	3.07	0.324	8.79×10^8	9.21×10^7	9.54
4291	2.7×10^{15}	15.44	14.87	0.81	1.1×10^9	1.24×10^8	8.87
4292	1.8×10^{16}	6.34	2.87	0.41	8.75×10^8	7.95×10^7	11.00
4294	8×10^{15}	6.75	6.96	0.79	1.1×10^9	8.2×10^7	13.41
4296	5×10^{15}	20.5	13.64	0.58	1.03×10^9	1.43×10^8	7.20
4297	5×10^{15}	21.0	14.43	0.61	1.03×10^9	1.45×10^8	7.10
4318	2×10^{15}	14.47	10.04	0.35	8.2×10^9	1.2×10^8	6.83
4374	5×10^{15}	22.11	16.08	0.63	9.58×10^8	1.48×10^8	6.47
4376	7×10^{15}	23.1	17.56	0.99	1.06×10^9	1.51×10^8	7.01
4377	3×10^{15}	29.0	4.07	0.45	8.82×10^8	1.7×10^8	5.18
4378	3.8×10^{15}	13.25	4.93	0.57	7.62×10^8	1.15×10^8	6.62
4383	5×10^{15}	15.1	6.25	0.26	8.7×10^8	1.22×10^8	7.13

TABLE II (Continued)

Shot #	Intensity W/cm ²	Hot electron temp. Tev (Kev)	Fraction of incident energy in ions (%)	Fraction of target mass in ions(%)	"Ion front" (VT) velocity (cm/sec)	Ion-sound speed $C_s = \sqrt{ZT_e/M}$	V_T/C_s
4385	6×10^{15}	18.5	6.71	0.27	7.8×10^8	1.36×10^8	5.73
4386	2×10^{15}	13.97	11.5	0.44	8.65×10^8	1.18×10^8	7.33
4387	2.4×10^{15}	17.4	9.0	0.51	9×10^8	1.32×10^8	6.81
4397	4×10^{15}	8.37	3.38	0.36	9.74×10^8	9.14×10^7	10.65
4401	1.2×10^{16}	31.18	12.89	0.80	1.26×10^9	1.76×10^8	7.15
4404	4.5×10^{15}	8.89	5.19	0.61	0.9×10^9	9.42×10^7	9.55
4405	1.1×10^{16}	7.54	5.92	0.29	9.29×10^8	8.67×10^7	10.71
4414	1.5×10^{15}	9.1	14.55	0.68	9.8×10^8	9.53×10^7	10.28
4416	1.2×10^{15}	4.52	8.45	0.264	7×10^8	6.71×10^7	10.43
4417	3.3×10^{15}	15.5	11.25	0.41	1.05×10^9	1.24×10^8	8.46
4418	2×10^{15}	13.8	11.78	0.37	1.06×10^9	1.17×10^8	9.05
4419	1.8×10^{15}	12.5	15.0	0.43	9.4×10^8	1.11×10^8	8.46

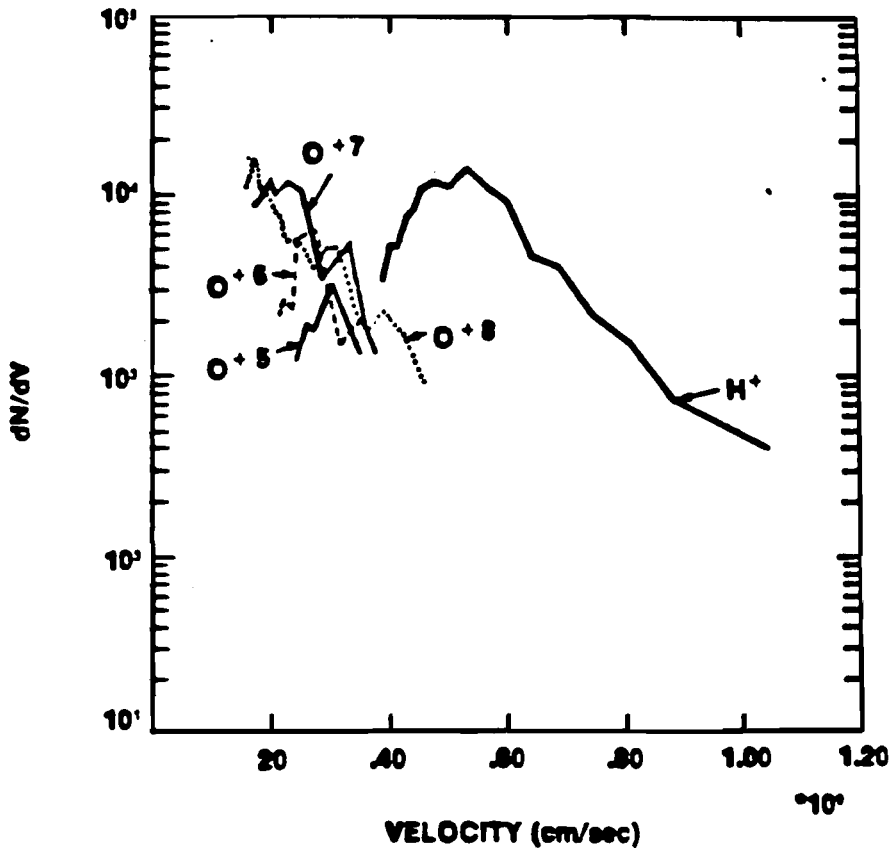
between prepulse and main pulse were used; 300 psec and 1100 psec.

A. Asymptotic Ion Distribution

Figure V2, shows a typical ion density distribution measured by the "Thomson Parabola". Separate plots of all the species have been shown. In the plasma blow-off, we found protons (H^+) and different species of oxygen (O^{+8} , O^{+7} , O^{+6} etc.). We numerically integrated these plots to obtain the total number of ions and the energy contained in them. The numerical data reduction computer program is attached at the end of this thesis. Four charge collectors¹⁰ were used at various positions in the target chamber to estimate the extent of asymmetry in the ion blow-off.

Figure VI A shows the positions of the charge collectors in the target chamber. They were placed at about 25 cm from the target. A typical charge collector trace is shown in figure VI B. The first peak of the trace corresponds to an ion velocity of about 1.2×10^8 cm/sec (charge collectors are not sensitive above this velocity). Although this peak lies at the lower end of the velocity spectrum measured by the "Thomson Parabola", this was the only diagnostic we had available to crudely estimate the angular distribution of the ion blow-off. For calculation purposes, we divided the target chamber into four sections, each section covering π solid angle (like an orange section) and containing one of the four charge collectors. Then, the amplitude of the first peak of all charge collector traces were normalized to the charge collector which was closest to the "Thomson Parabola." For example,

ION SPECIES DENSITY DISTRIBUTION AS A FUNCTION OF VELOCITY



E1034

Figure V.2

CHARGE COLLECTOR TRACE

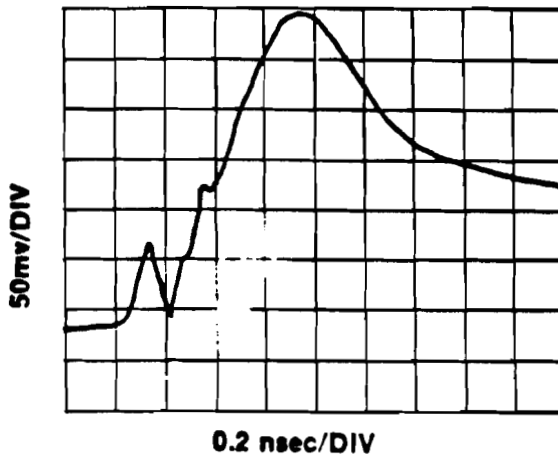
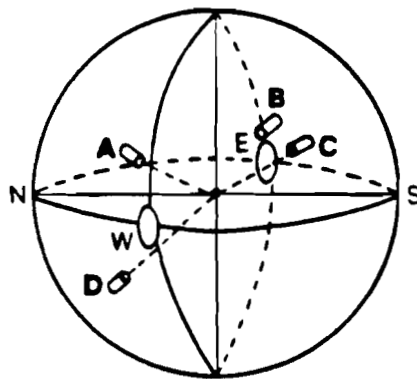


Figure V.1B



- A. At NE 45° Horizontal
- B. Top of East Lens
- C. 45° SW Horizontal
45° Vertical Up
- D. 45° NW Horizontal
45° Vertical Down

Figure V.1A

E1134

if the amplitudes of charge collectors A, B, C and D are a, b, c and d respectively and charge collector "A" is closest to "Thomson Parabola", then the effective solid angle is

$$\Omega_{\text{eff}} = [\pi + \pi(b/a) + \pi(c/a) + \pi(d/a)] = \pi \left[1 + \frac{(b+c+d)}{a} \right]$$

This provided us with the correction factor to estimate the non-thermal ion blow-off in 4π . As can be seen from the plot, the ion density has high frequency, high amplitude modulations. We have proposed a two stream ion-ion instability model to explain this. This we have already discussed in detail in Chapter III. We believe it provides a good explanation.

In Chapter II, we discussed several characterizations that can be made of the expanding plasma, once the ion density distribution is known. Now, we will invoke those models to characterize the plasma. One should bear in mind at this point that all the models are strictly one dimensional and planar, while the experiment is on spherical targets. Two and three dimensional computer simulations, however, have indicated that the use of these models is an excellent method to estimate plasma parameters macroscopically, without introducing significant error. We will compare our results to the theoretical and numerical models discussed in Chapter II.

B. Hot Electron Temperature

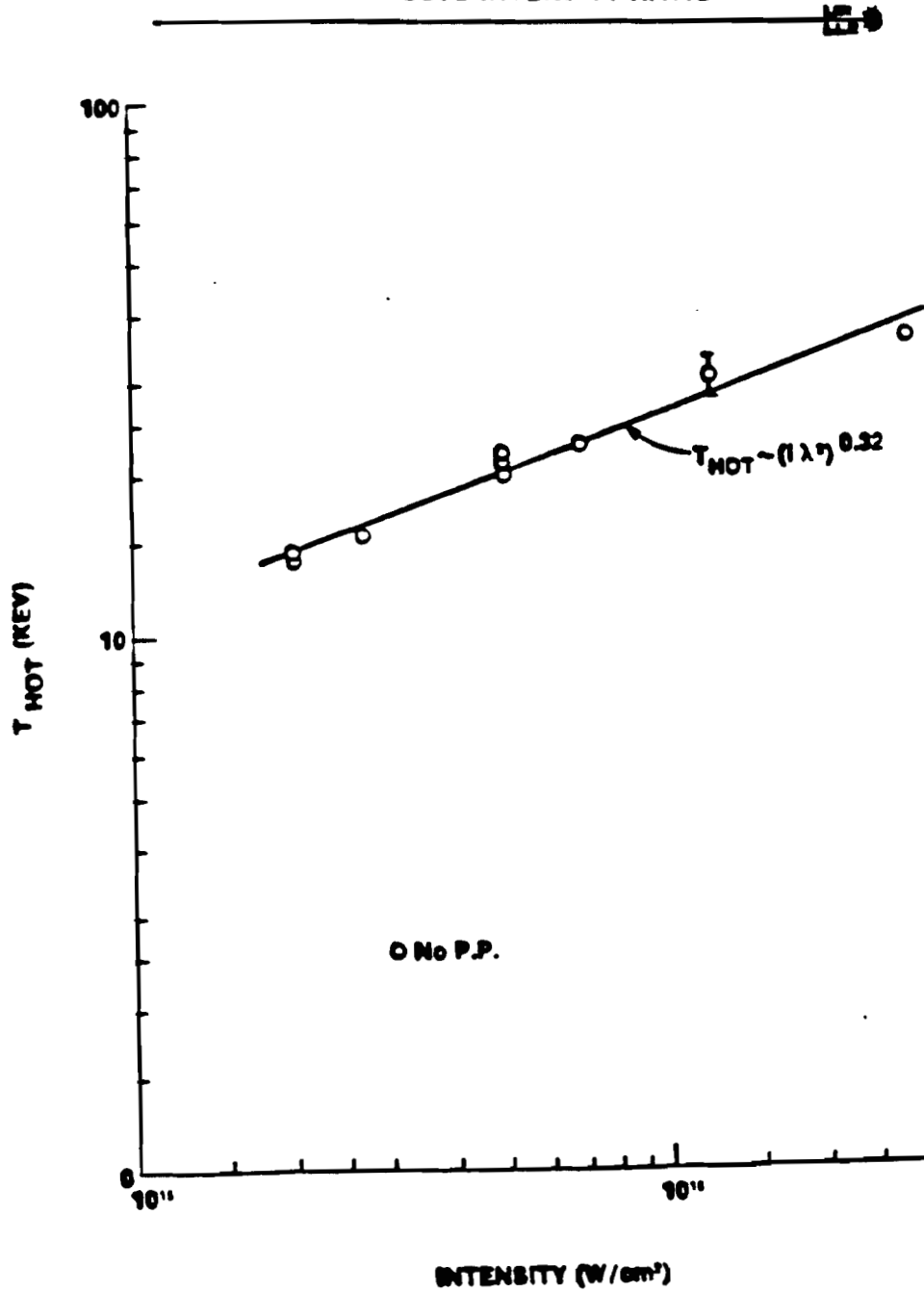
If for the moment we ignore the modulations in the density distribution, the plot of $\ln(dN/dV)$ versus V (figure V2)

is essentially a straight line. This is the form expected from the self-similar solution of an isothermal rarefaction model (equation 28, Chapter II). The measurement of the slope of the distribution and the use of equation (28) gives an estimation of hot electron temperature. The dependence of hot electron temperature on intensity is shown in figure V3. It follows a power law $T_e = K(I\lambda^2)^{0.32}$, $K = 1.89 \times 10^4$ Kev/watt. Interestingly, with the introduction of a prepulse, the power law is no longer valid. A dramatic change is observed for prepulse to main pulse ratio of 10^{-2} (figure V4). The hot electron temperature becomes independent of intensity, hot electron temperature, however, goes down with increasing contrast ratio. However, the type of prepulse does not make a significant difference (figure V5).

C. Fraction of Target Mass in Energetic Ions

The plot of (dN/dV) vs. V (figure V2) can be used to evaluate total number of ions detected. The integration for $\int_V (\sum_i (dN_i/dV_i)) dV$ is carried out where the summation is over all the species i present. This number is compared to the total number of atoms present in the target. For example, a 80 μm diam. 0.8 μm thick glass microballoon has approximately 2.56×10^{15} atoms. The fraction of the total target mass carried by non-thermal ions, evaluated in this manner, is shown in figure V6. It is below 1%. Surprisingly, in all cases, there is no effect of intensity on number of ions involved. Furthermore, no effect of prepulse (both for its relative amplitude and timing to main

HOT ELECTRON TEMPERATURE VERSUS INTENSITY
FIGURES NEXT TO POINTS INDICATE PREPULSE
TO MAIN PULSE INTENSITY RATIO



67422

Figure V.3

**HOT ELECTRON TEMPERATURE VERSUS INTENSITY
 FIGURES NEXT TO POINTS INDICATE PREPULSE
 TO MAIN PULSE INTENSITY RATIO**

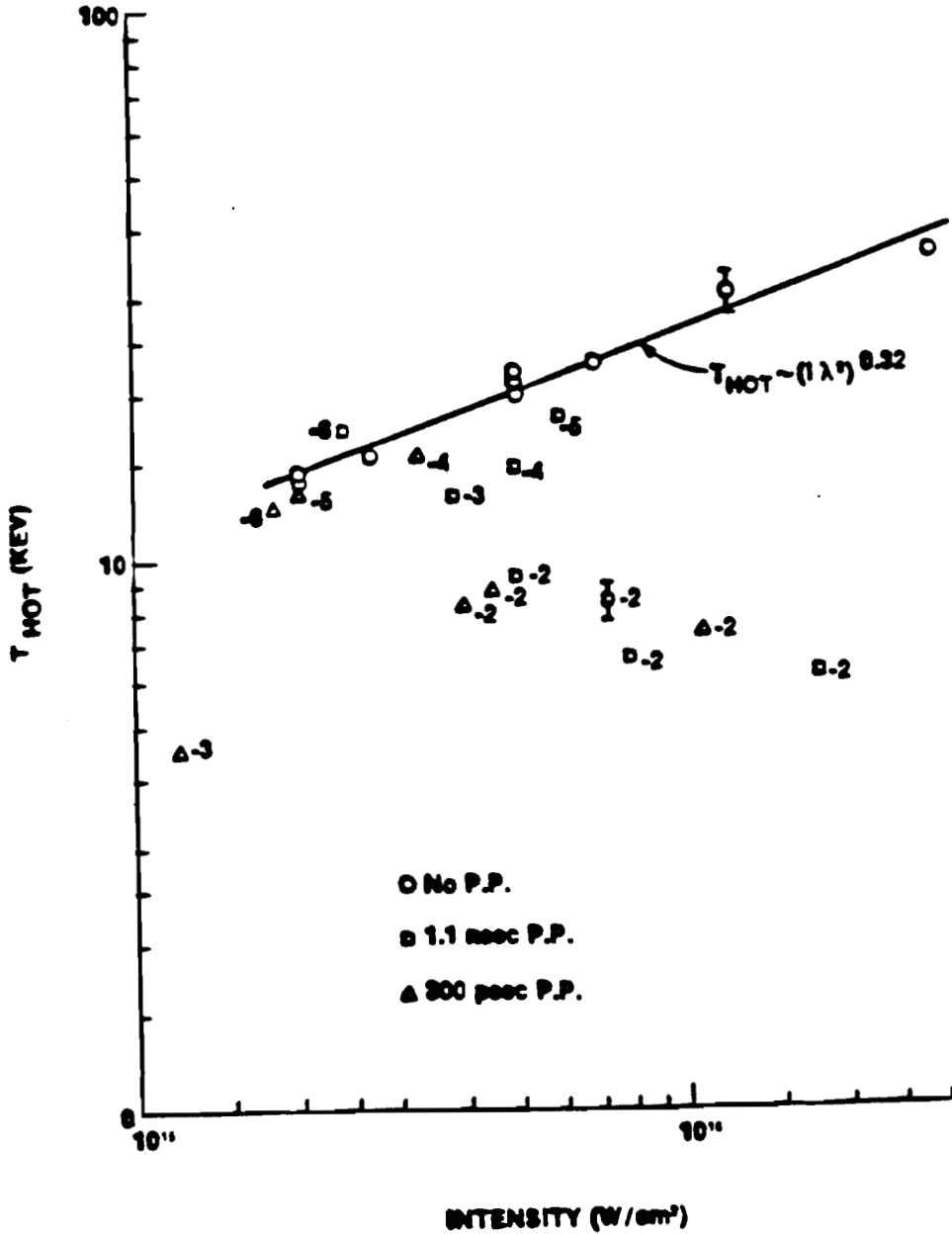
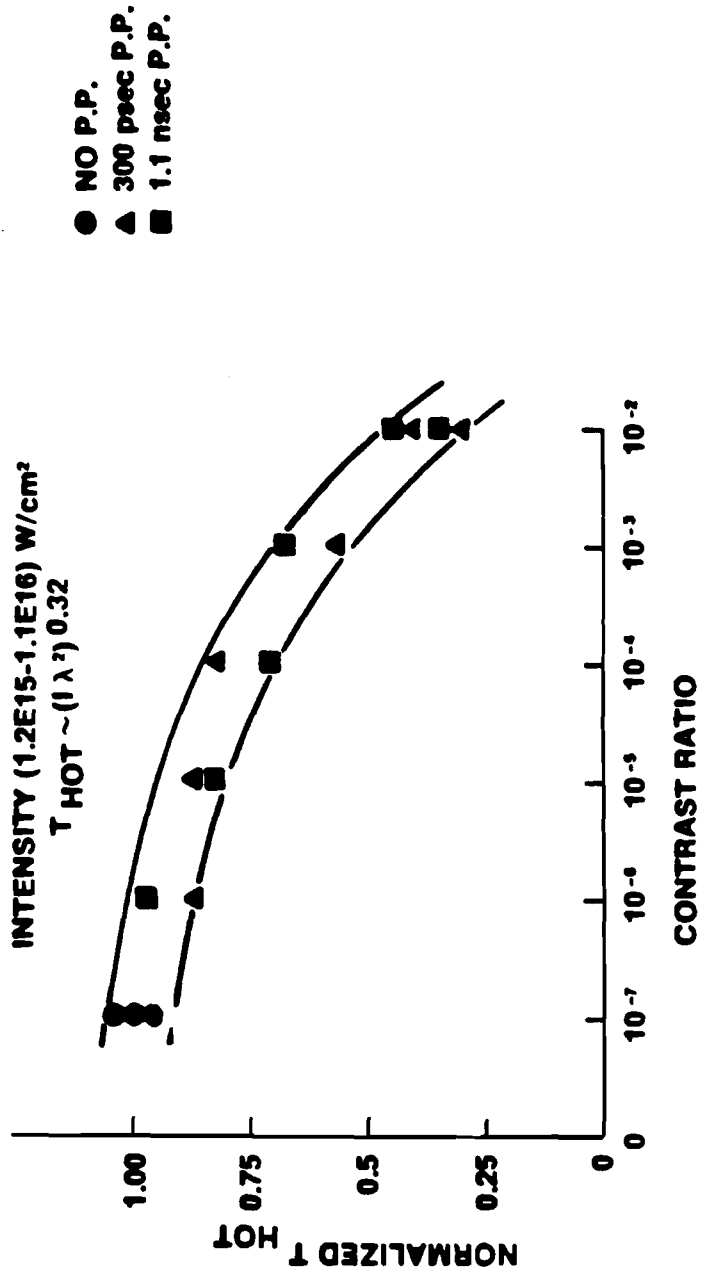


Figure V.4

(Numerals next to data points indicate log₁₀ of Prepulse to Main pulse amplitude ratio.)

NORMALIZED HOT ELECTRON TEMPERATURE VERSUS PREPULSE TO MAIN PULSE INTENSITY RATIO

LJR
LLE

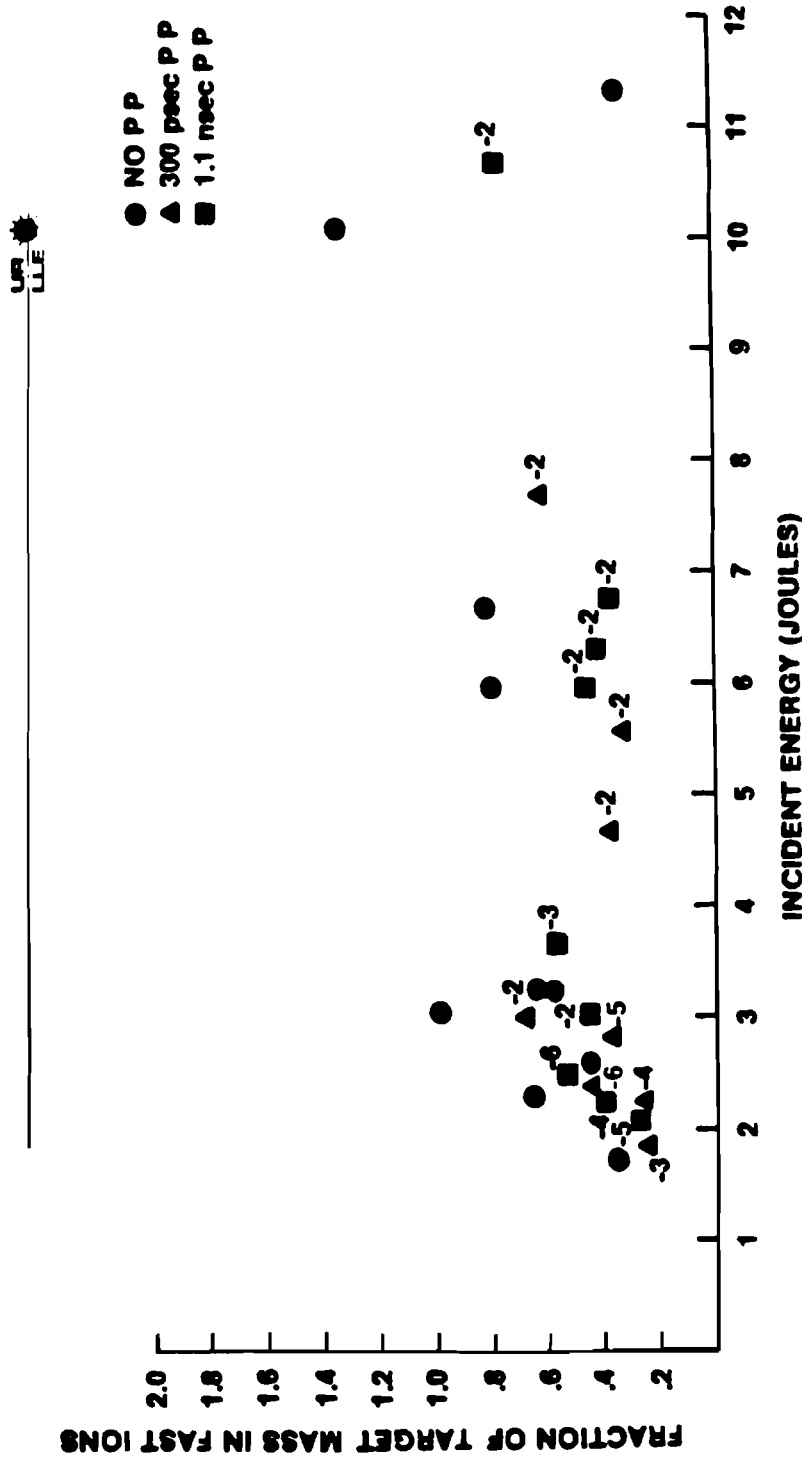


(10⁻⁷ is defined as no prepulse on the target.)

E908

Figure V.5

FRACTION OF TARGET MASS IN NONTHERMAL IONS VERSUS ENERGY ON THE TARGET



(Numerals next to data points indicate log₁₀ of prepulse to main pulse amplitude ratio.)

E907

Figure V.6

pulse) was observed (figure V7).

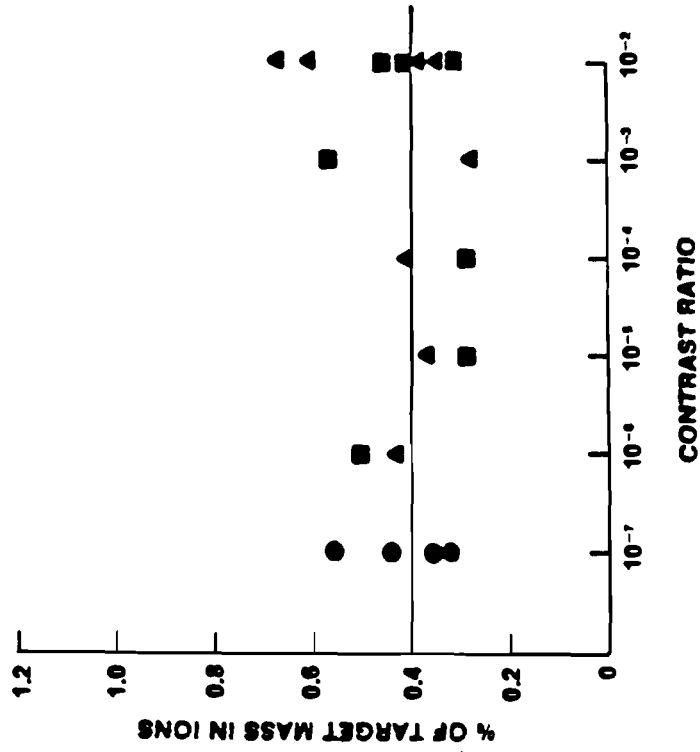
D. Fraction of Incident Energy in Energetic Ions

Recall the plot of dN/dV vs. V (figure V2), the integration $\int_V \sum_i (M_i/2) (dN_i/dV_i) V_i^2 dV_i$ gives the total energy carried by these non-thermal ions. The estimation of the total ion energy in 4π solid angle is done in the same way as discussed in Section A. This, then, is compared to the laser energy incident on the target. The fraction of the energy incident on the target, carried by non-thermal ions evaluated in this manner is shown in figure V8. This fraction varies from 2.5% to 25%. We see that the fraction of energy increases with increasing incident energy for no prepulse case. With the introduction of prepulse this fraction goes down. At prepulse to main pulse amplitude ratio of 10^{-2} , however, the fraction becomes independent of incident energy. It should be pointed out here, that in this case no difference between the 300 psec and 1100 psec prepulse is observed. As can be seen from figure 9, the energy fraction in non-thermal ions goes down with increasing contrast ratio, interestingly; the drop is faster in case of an 1100 psec prepulse compared to 300 psec prepulse. This we believe is due to a longer scale length plasma created by an 1100 psec prepulse, a discussion will follow in this Chapter.

FRACTION OF TARGET MASS IN NON-THERMAL IONS VERSUS PREPULSE TO MAIN INTENSITY RATIO

USP
LLF

- NO P.P.
- ▲ 300 psec P.P.
- 1.1 nsec P.P.

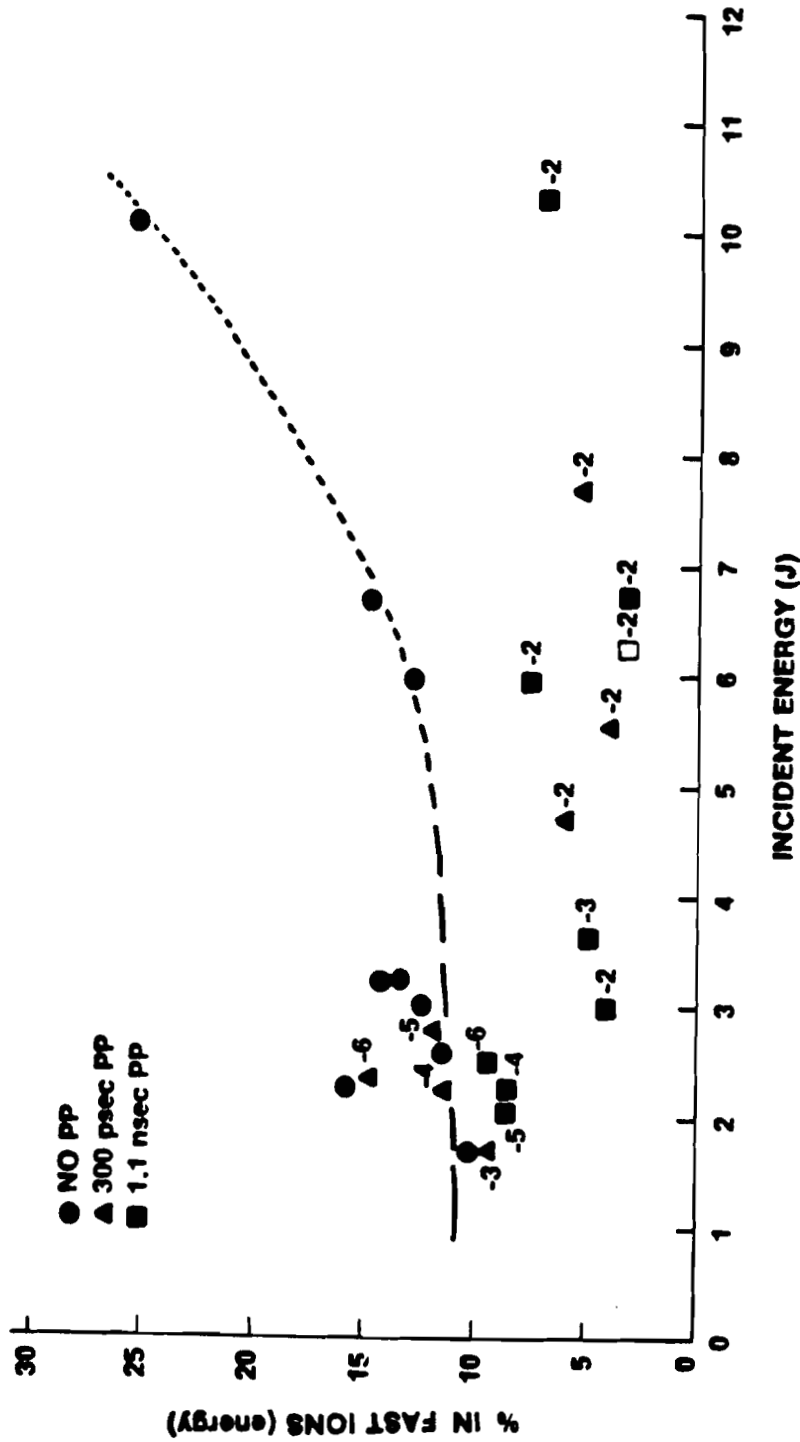


EB006 (10^{-7} is defined as no prepulse on the target.)

Figure V.7

FRACTION OF INCIDENT ENERGY IN NON-THERMAL IONS VERSUS ENERGY INCIDENT ON THE TARGET

LPR
LLE



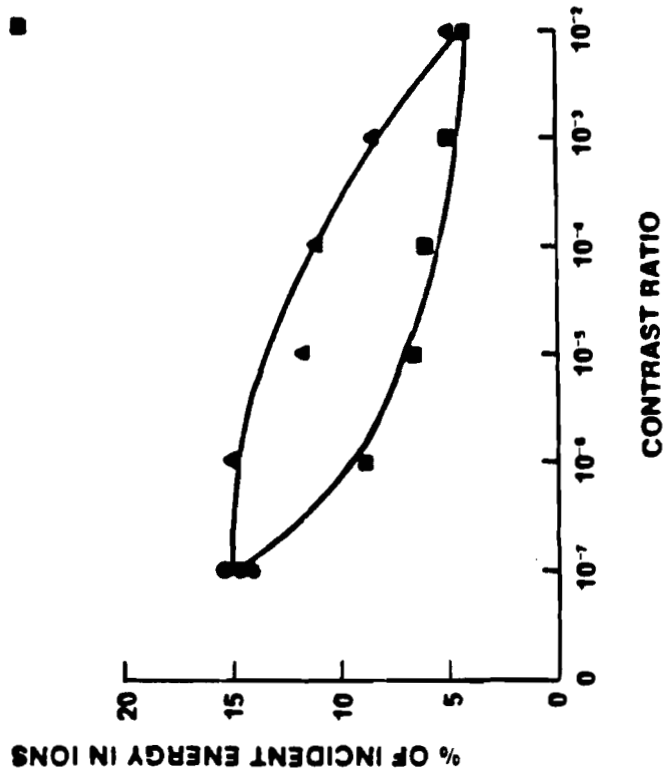
ES05 (Numerals next to data points indicate \log_{10} of prepulse to main pulse amplitude ratio.)

Figure V.8

FRACTION OF INCIDENT ENERGY IN NON-THERMAL IONS VERSUS PREPULSE TO MAIN PULSE INTENSITY RATIO

LFR
LLE

- NO PP
- ▲ 300 psec PP
- 1.1 nsec PP



E904 (10^{-7} is defined as no prepulse on the target.)

Figure V.9

E. Maximum Expansion Velocity

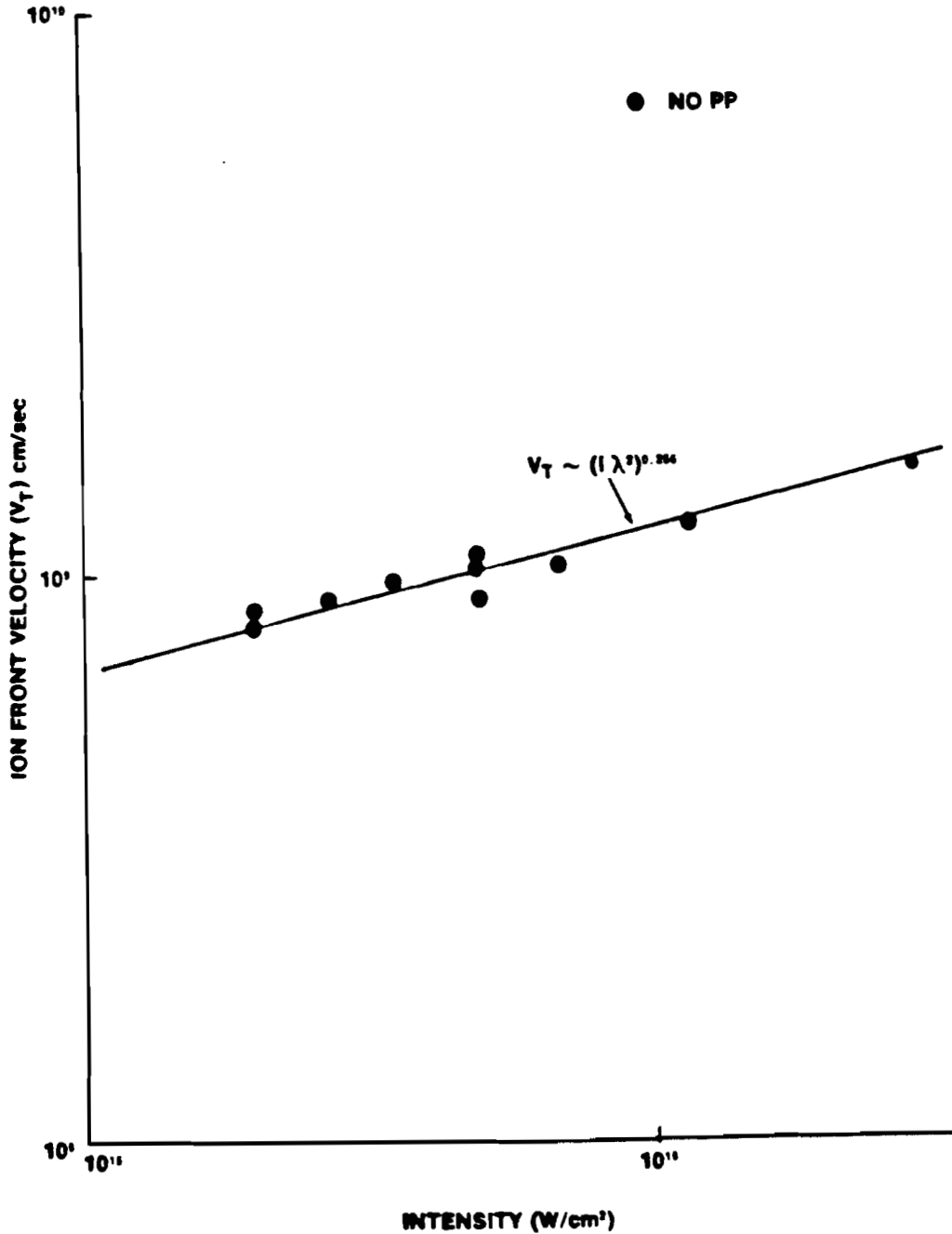
Because of their high charge to mass ratio, the protons ($Z/M = 1$) are pulled out preferentially by the electric field from the mixture of ions of lower charge to mass ratios ($Z/M = 0.5$ and less). Therefore, protons happen to be the fastest moving particles in the expanding plasma. Their terminal velocity has been used as the maximum expansion velocity (or "Ion Front") velocity of the plasma.

The "ion front" velocity (V_T) has been plotted in figure V10. This increases with intensity for no prepulse case (fig. V10a) and follows a power law $V_T = K(I\lambda^2)^{0.25}$, $K = 9.83 \times 10^4 \text{ cm}^3/\text{Joule}$. With the introduction of prepulse, however, the ion front velocity becomes intensity invariant (fig. V10b). We have also calculated for each shot the ion sound speed ($C_s = \sqrt{Z_i T_e / M_i}$). This has been compared to the "ion front" velocity and the figure V11 shows the plot. We find that the ratio of "ion front" velocity to ion sound speed is higher for the prepulse case than for no prepulse case.

F. Discussion

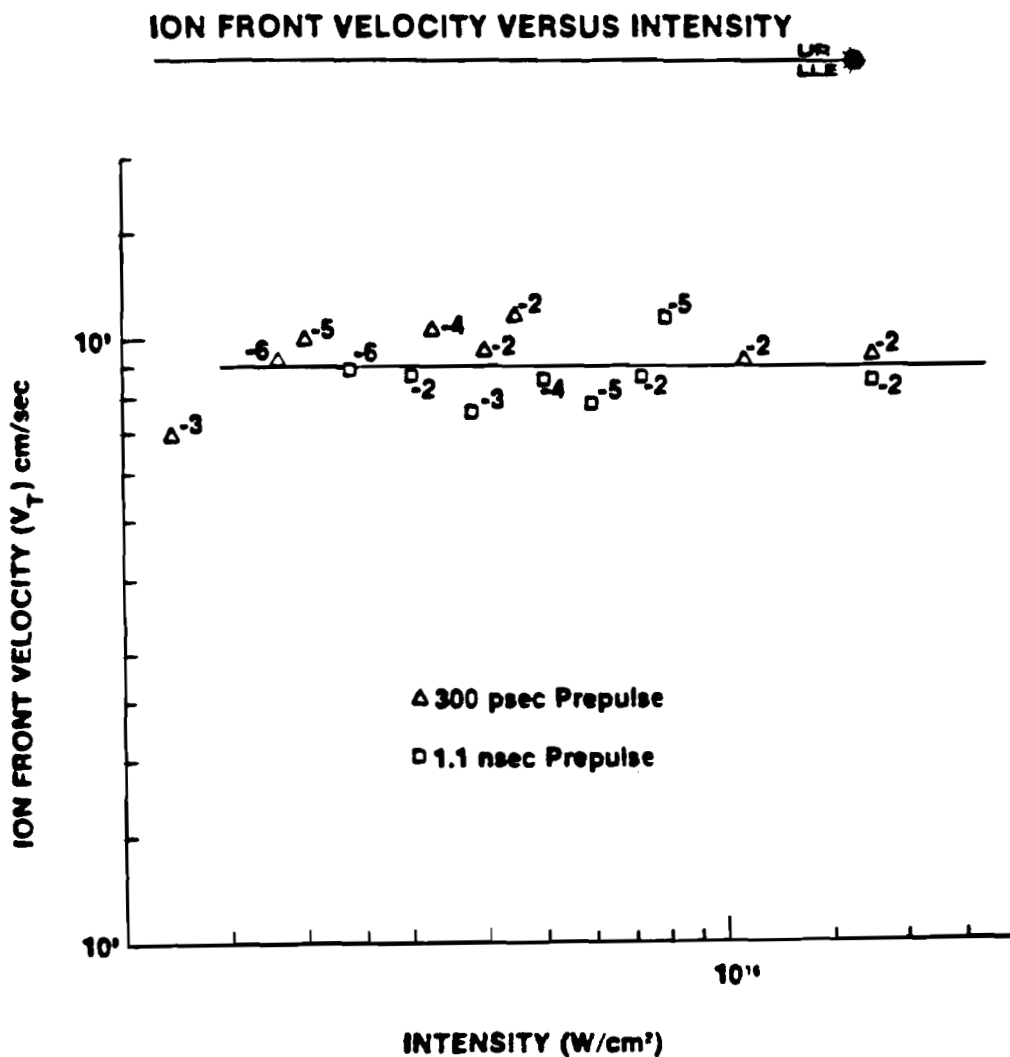
Now we will compare our results to the theoretical models and numerical predictions discussed in Chapter II. It should be kept in mind that any quantitative agreement is somewhat fortuitous, for several reasons. First of all, the models are one dimensional. Secondly, we do not have any knowledge of total absorption and particularly the partition in different absorption mechanism. Finally, the extent of anisotropy of non-thermal ion is unknown. Qualitative

ION FRONT VELOCITY (V_T) VERSUS INTENSITY



E902

Figure V.10a



(Numerals next to data points indicate \log_{10} of prepulse to main pulse ratio.)

E1031

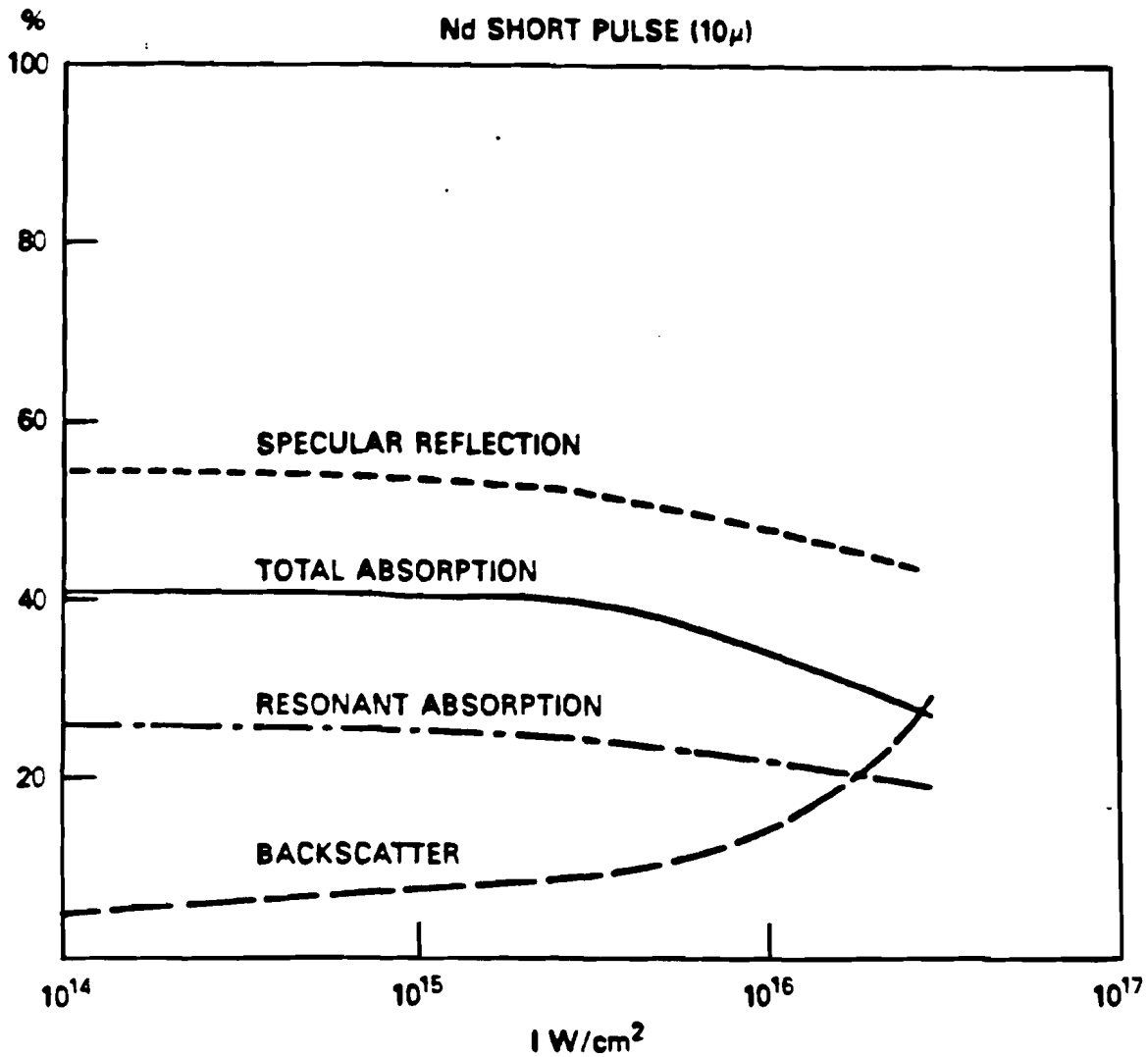
Figure V.10b

agreements, however, we believe will lead us to the better understanding of the dynamics.

We find that the dependence of hot electron temperature on intensity $T_e \sim (I\lambda^2)^n$, for no prepulse case, agrees very well with the predictions made by the numerical description^{1,2} of electron heating mechanism by resonant absorption. In our case $n = 0.32$, whereas the scheme predicts $0.3 < n < 0.4$. The flux limiting arguments,³ however, predict $n = 0.66$. Therefore, the dominance of the resonant absorption is obvious from these experiments.

For all cases, we did not find any effect of intensity on number of ions involved (figure V6). This is not too surprising, if we recall equation (II-38). There we predicted that number of non-thermal ions should vary as $I^{0.1}$. This explains the weak intensity dependence seen experimentally.

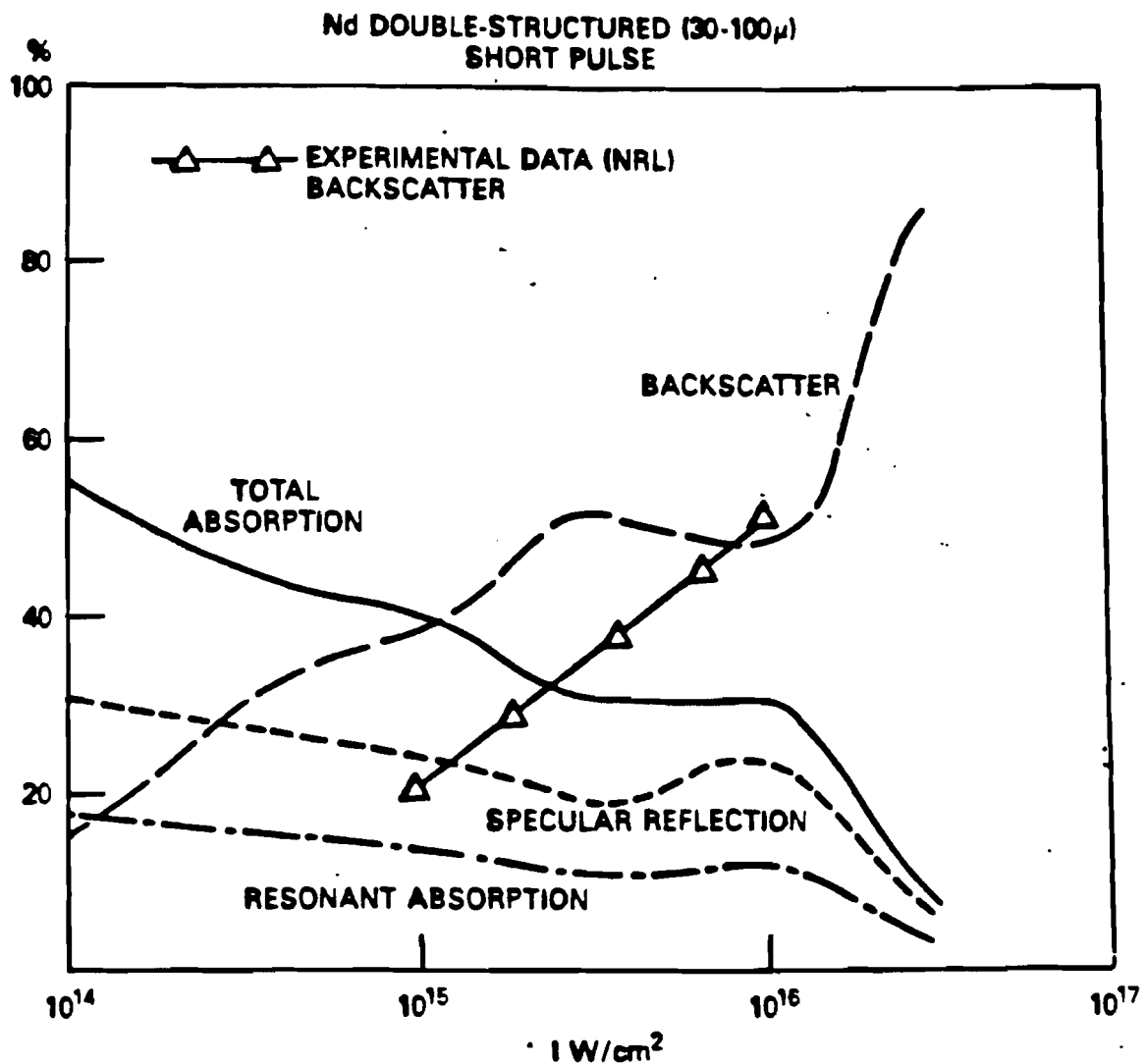
We will now use the predictions of computer simulations of Ref. 8 to explain some of our other observations. We have discussed this in some detail in Chapter II. For convenience a portion of the simulation, relevant to our purpose, has been reproduced in figures V12, V13 and V14. These simulations were done for 70 psec, Nd: Glass laser on glass microballoon targets. The numerical simulation predicts (figure V12) that for short single pulse (no-prepulse) resonant absorption remains almost constant over the range of intensities on the target, dropping slowly at about 10^{16} W/cm². This suggests that for the same laser pulse width an increase in intensity (which also means increase in energy) on the target will result in more light tunnelling through to the critical surface. Therefore, there will be an enhancement in the



Plot of absorption, resonant absorption, specular reflection and backscatter as a function of irradiance for short pulse Nd laser plasma

Figure V.12

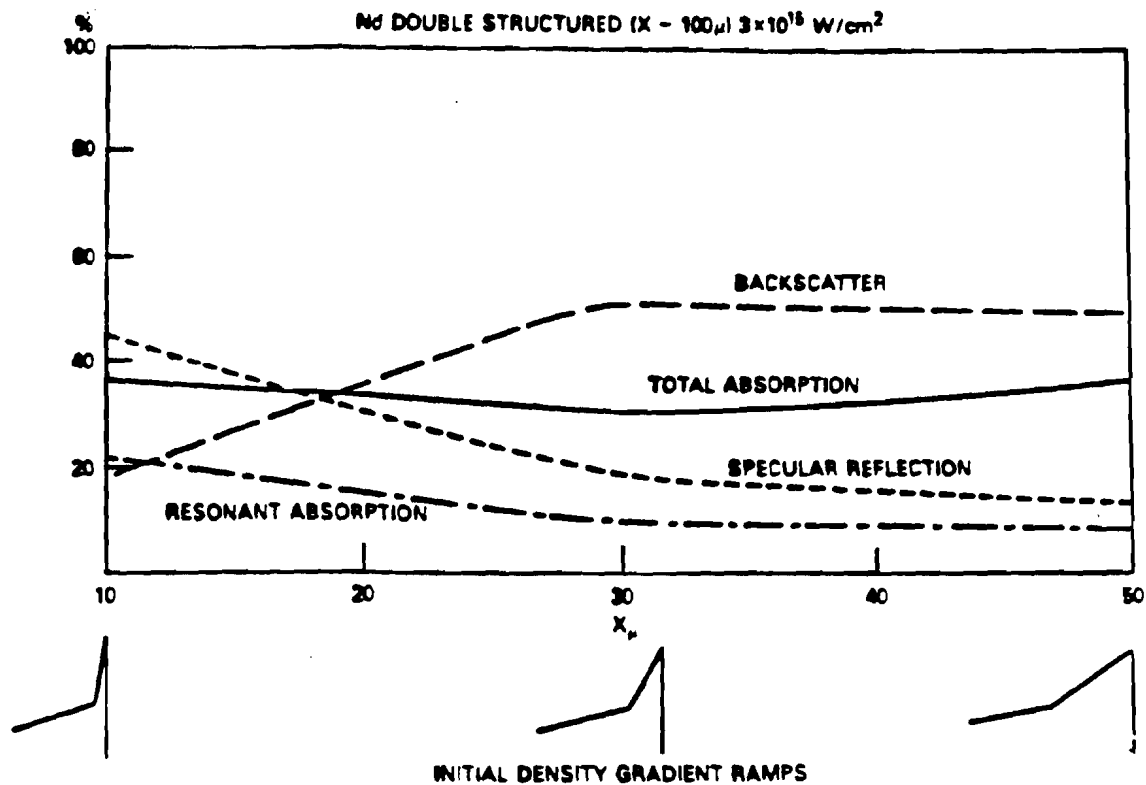
(Reproduced from NRL Memorandum Report 4083, Oct. 1979 by D.G. Colombant and W. Manheimer)



Plot of absorption, resonant absorption, specular reflection, and backscatter as a function of irradiance for a double structured pulse Nd laser plasma. The line which extends from 10^{15} - 10^{16} W/cm^2 is the NRL data

Figure V.13

(Reproduced from NRL Memorandum Report 4083, Oct. 1979 by D. G. Colombant and W. Manheimer)



Plot of absorption, resonant absorption, specular reflection and backscatter as a function of inner gradient scale length x_μ for a double structured Nd laser produced plasma at maximum irradiance 3×10^{15} W/cm²

Figure V.14

(Reproduced from NRL Memorandum Report 4083, Oct. 1979 by D. G. Colombant and W. Manheimer)

energy coupled to the hot electrons. This in turn will cause an increase in hot electron temperature. Also the energy coupled to the ions will be increased. For the same number of ions involved this will translate into an increase in maximum expansion velocity ("Ion Front" velocity). In other words, these numerical simulations simply suggest us that for no prepulse case, hot electron temperature, "ion front" velocity and energy contained in non-thermal ions should increase with intensity (energy) on the target. Our experimental observations, shown in figures V3, V10a and V8, agree very well with these predictions.

On the other hand, the numerical simulation shows that under similar conditions with the introduction of prepulse (which has been designated as double structured short pulse) not only is the fractional resonant absorption lower compared to short single pulse, but it decreases with increasing main pulse intensity. For example, at 10^{15} watts/cm², for short single pulse the resonant absorption is 25%, where as in case of double structured pulse (prepulse case) it is 12%. When resonant absorption decreases, less light tunnels through to the critical surface and the energy coupled to hot electrons decreases. This explains as to why we observe lower electron temperature for same intensity on target, when prepulse is introduced (figure V4). Lower energy in electrons means lower energy coupled to ions, a prediction consistent with the experimental observation, figure V8. For the same number of ions involved (figure V6), a decrease in "ion front" velocity is expected and observed (figure V10b).

In addition, we also varied the relative amplitude and timing of the prepulse to the main pulse. We did not measure the scale lengths

of the underdense plasma. But we believe and support the generally agreed upon understanding that, (a) prepulse causes the formation of long scale length plasma before the arrival of main pulse and, (b) the increased amplitude ratio and/or delay between prepulse and main pulse results in the creation of longer scale length underdense plasma. In computer simulations it is difficult to calculate the scale length of the underdense plasma based on amplitude ratios and delays. Authors in Ref. 8 have, therefore, used different scale length underdense plasma under the assumption that they simulate varied amplitude ratios and delays between prepulse and main pulse. This has been shown in figure V14. We will use these simulations to explain our results for varied prepulses. One should be cautioned here not to take the analogies too seriously for quantitative use. This is because we do not have scale length measurements. Qualitative arguments, however, are worth appreciation.

As one can see from figure V14, with the increasing scale length of underdense plasma, the fractional resonant absorption is going down. For example, it decreases from 20% to 10% when the scale length increases from 10 μm to 30 μm . In our case, an increase in contrast ratio will mean an increase in scale length of the underdense plasma. Furthermore, we varied the contrast ratios around the main pulse intensity of 2×10^{15} Watts/cm². Fortunately, the computer simulations were done at intensities of 3×10^{15} Watts/cm² and therefore, provide an excellent basis for comparison. As predicted, the decrease in fractional resonant absorption with increasing scale length (figure V14) results in lower hot electron temperature

(figure V5) and energy content in non-thermal ions (figure V9). As explained earlier, the number of ions involved, however, remains unaffected (figure V7). The decrease in energy content in ions is faster for 1100 psec prepulse compared to 300 psec prepulse, with increasing contrast ratio (figure V9). This, we believe, is because of the comparatively longer plasma scale lengths produced by the longer delay between prepulse and main pulse and the subsequent reduction in resonant absorption. Surprisingly, no effect of the difference in prepulse to main pulse delay is observed for hot electron temperature (figure V5). For complete understanding, a thorough theoretical scrutiny in this matter is recommended.

Another surprising observation is the fact that at high contrast ratios (10^{-2} in this case) the hot electron temperature (figure V4), ion energy (figure V8) and "ion front" velocity (figure V10b) become independent of laser intensity (energy). From theoretical simulations (figure V13), we find that the resonantly absorbed fraction is decreasing with increasing intensity. One can infer from this, that the amount of energy getting to the critical surface is not changing very much and therefore, the invariance of the parameters mentioned above should be expected. Furthermore, at very large scale lengths (which will be produced by high contrast ratio), the back-scatter and the interplay between different absorption mechanisms limits the amount of light going to the critical surface. This has been discussed in Chapter II. We believe, that this limited amount of light tunneling through to the critical surface produces a small change in the energy coupled to hot electrons. Therefore, the observations are consistent.

We conclude that it is the change in the fraction of resonant absorption, caused by various plasma conditions (particularly scale length of underdense plasma), that causes the change in hot electron temperature and therefore, non-thermal ion characteristics. This also implies that resonant absorption is in fact the dominant mechanism for the production of hot electrons.

Figure VII shows the ratio of "ion front" velocity (V_T) to ion sound speed ($C_s = \sqrt{Z_i T_e / M_i}$). Pearlman and Morse⁴ have suggested two schemes, equations (II-20) and (II-26) respectively, to theoretically estimate the maximum expansion velocity. The logarithm in equation (II-20) makes this ratio insensitive to changes in experimental parameters. Experimentally we find this ratio to change from 7 to 11 (figure VII), under different experimental conditions. Therefore, we believe, that the predictions leading to equation (II-20) fail to explain the experiments. The predictions leading to equation (II-26), however, are in good agreement with experimental observations. Equation (II-26) suggests that this ratio, for no-prepulse, is between 5-7, which is close to the experimental observations. It should be pointed out here that the major uncertainty is in estimating the density at which charge neutrality breaks down. This was required for the development of equation (II-26).

It is noteworthy that the ratio of "ion front" velocity to ion sound speed is higher when a prepulse is introduced. The escalation of this ratio, for the prepulse case, we believe is due to the reduction in ion sound speed from lower electron temperature. The "ion front" velocity is mostly governed by electron pressure, which is a function of electron density, density scale length and temperature. Therefore, "ion front" velocity probably does not vary as $(T_e^{0.5})$, as might be

expected, but depends on the interplay between these quantities.

The details of the interplay, however, are not well understood. As a matter of fact, experimentally we have found V_T to vary as $(T_e)^{0.8}$, where as C_s varies as $(T_e)^{0.5}$.

VI. COMMENTS AND SUMMARY

In conclusion, we have presented clear experimental evidence that the introduction of a prepulse causes the hot electron temperature and the energy contained in non-thermal ions ($> 10 \text{ Kev/Z}$) to be reduced. This will reduce the preheat of the target core. If more energy is coupled into thermal ions, more recoil momentum is available for efficient fuel compression. In addition, we have seen definite variations in the plasma parameters that depend on the nature of the prepulse. For example, the energy of non-thermal ions drops faster as the amplitude ratio is increased for an 1100 psec prepulse than for a 300 psec prepulse. In both cases the intensity of the main pulse is kept the same. From these observations we infer that a preformed plasma with long scale length existing before the main pulse intensity peaks may be favorable to the requirements of laser fusion. We believe that these conditions can also be achieved in long, shaped laser pulses ($> 1 \text{ nsec}$) duration, therefore, these pulses deserve further investigation.

Resonant absorption, believed to exist at high laser intensities ($> 10^{14} \text{ watts/cm}^2$), can account for the observed changes in hot electron temperature and ion energies. In the absence of absorption measurements, we are unable to test this idea quantitatively; qualitatively however, our results are quite consistent with theoretical models and numerical simulations. Also, experimental observations indicate that isothermal expansion of the plasma is a reasonable assumption.

Although we are able to explain most of our results with simplified

assumptions and one dimensional models, 2-D and 3-D models will definitely provide an improvement to the explanation. The invariance of the number of non-thermal ions with changing intensity may provide a fruitful guideline for planning experiments at higher intensities.

We have also proposed that the expanding plasma could be short wavelength ($\approx \lambda_D$) ion-ion two stream unstable. This may act as a source for long wavelength ion acoustic turbulence. A further investigation of this effect is required.

It is our conjecture, based on the reasons outlined earlier, that the hot electron temperature deduced from the ion density distribution is a much better representation of electron temperature than that deduced from x-ray measurements. Most laboratories use the latter method to derive the electron temperature. From our experimental observations, we suggest that they should exercise some care in their judgment.

These data suggest other experiments that might provide additional information regarding the production of energetic ions. First of all, our experiments should be repeated with a measurement of overall absorption, and with a determination of the partition of this absorption in different absorption mechanisms. This will quantify the effect of scale length on resonant absorption, and therefore on the hot electron temperature. Also the use of several "Thomson Parabolas" will provide a knowledge of the extent of asymmetry in the ion blow-off.

Most of the ion measurements presented in this work were obtained for short laser pulse lengths (50 psec), and for high irradiances ($> 10^{15}$ W/cm²). Another interesting regime for laser fusion is that

of 10^{13} - 10^{14} Watts/cm² intensities and longer pulse lengths (> 1 nsec). Ion measurements should therefore be performed at lower intensities to see how the energy content in energetic ions and the hot electron temperature scale. Also we suggest that measurements of density scale lengths should be made simultaneously in order to understand more clearly the dependence of scale length on electron temperature. In all cases presented here, the laser beams were focused on the surface of glass microballoons, it would be interesting to study non-thermal ions under other focusing schemes. It would also be interesting to extend these investigations to glass microballoons coated with high Z materials.

We expect that these observations of non-thermal ions (> 10 Kev/Z) will lead to a better understanding of their generation and propagation mechanisms. This will in turn aid in the efforts to minimize their generation, leading closer to the success of laser driven thermonuclear fusion.

REFERENCES

- I-1. J. Nuckolls, et. al., Nature 239, 139, 1972.
- I-2. J.S. Clarke, et. al., Phys. Rev. Lett. 30, 89, 1973.
- I-3. K.A. Bruckner and S. Jorna, Rev. Mod. Phys. 46, 235, 1974.
- I-4. D.G. Colombart and W. Manheimer, NRL Memorendum Report 4083 Oct. 1979.
- I-5. N. Krall and A. Trivelpiece, "Principles of Plasma Physics", McGraw-Hill, 390, 1973.
- II-1. J. Dawson and C. Oberman, Phys. Fluids 5, 517, 1962.
- II-2. V.L. Ginzburg, "The Properties of Electromagnetic Waves in Plasma", Pergamon, New York, 1964.
- II-3. V.P. Silin, Sov. Phys. JETP 21, 1127, 1965.
- II-4. D.F. Dubois, et. al., Phys. Rev. 164, 207, 1967.
- II-5. K. Nishikawn, J. Phys. Soc. Japan 24, 916, 1968.
- II-6. E.A. Jackson, Phys. Rev. 153, 235, 1967.
- II-7. J.M. Dawson and C. Oberman, Phys. Fluids 6, 394, 1963.
- II-8. C.S. Liu, et. al., Phys. Fluids 17, 1211, 1974; many references there in.
- II-9. B.W. Boreham and B. Luther-Davies, J. Appl. Phys. 50(4), 1979.
- II-10. R.J. Bickerton, Nuclear Fusion 13, 457, 1973.
- II-11. F. Chen, "Laser Interaction and Related Phenomena", Vol. 3, Plenum Press, 1974.
- II-12. P. Mulser and C. Van Kessel, Phys. Lett., 59A, 33, 1974.
- II-13. W. Manheimer, Phys. Fluids 20, 265, 1977.
- II-14. W. Kruer in, "Comments on Plasma Physics and Controlled Fusion", ed. Burton D. Fried, Gordon and Breach Publishers, 1979.

- II-15. P. Kaw, et. al., Phys. Fluids 16, 1522, 1973.
- II-16. J.J. Thomson, et. al., Phys. Fluids 21, 707, 1978.
- II-17. K.G. Estabrook, et. al., Phys. Fluids 18, 1151, 1975.
- II-18. J.P. Freidberg, et. al., Phys. Rev. Lett. 28, 795, 1972.
- II-19. D.W. Forslund, et. al., Phys. Rev. A11, 679, 1975.
- II-20. N.G. Danisov, Sov. Phys. JETP 4, 544, 1957.
- II-21. E.J. Valeo and Ira Bernstein, Phys. of Fluids 19, 1348, 1976.
- II-22. R. Turner, Ph.D. Thesis, University of Rochester, 1980.
- II-23. R. Fedosejevs, et. al., Phys. Rev. Lett. 39, 932, 1977.
- II-24. A.V. Gurevich, et. al., Sov. Phys. JETP 22, 449, 1966.
- II-25. J.E. Allen and J.G. Andrew, J. Plasma Phys. 4, 187, 1970.
- II-26. J.E. Crow, et. al., J. Plasma Phys. 14, 65, 1975.
- II-27. E.L. Lindman, Los Alamos Scientific Laboratory Report LA-UR-77-1007, 1977.
- II-28. B. Bezzerides, et. al., Phys. Fluids 21, 2179, 1978.
- II-29. Mike True, Laboratory for Laser Energetics, Private Comm.
- II-30. P. Prewett and J.E. Allen, J. Plasma Phys. 10, 451, 1973.
- II-31. J.S. Pearlman and R.E. Morse, Phys. Rev. Lett. 40, 1652, 1978.
- II-32. M. Widner, et. al., Phys. Fluids 14, 795, 1971.
- II-33. K. Estabrook and W. Kruer, Phys. Rev. Lett. 40, 42, 1978.
- II-34. D.W. Forslund, et. al., Phys. Rev. Lett. 39, 384, 1977.
- II-35. V.P. Silin, JETP Lett. 21, 152, 1975.
- II-36. R. Turner, Ph.D. Thesis, University of Rochester, 1980.
- II-37. B.H. Ripin and E.A. Mclean, Appl. Phys. Lett. 34, 11, 1979.
- II-38. B.H. Ripin, et. al., Phys. Rev. Lett. 39, 10, 1977.
- II-39. D.G. Colombart and W. Manheimer, NRL Report 4083, Oct. 1979.

- III-1. I.P. Shkarofsky, T. Johnson and M. Bachyuski, "The Particle Kinetics of Plasma", Addison-Wesley, 1966.
- III-2. T. Boyd and J. Sanderson, "Plasma Dynamics", Barnes and Nobles, 274, 1969.
- III-3. N. Krall and A. Trivelpiece, "Principles of Plasma Dynamics", McGraw-Hill, 454, 1973.
- III-4. R.C. Davidson, et. al., Phys. Rev. Lett. 24, 579, 1970.
- III-5. C.F. McKee, Phys. Rev. Lett. 24, 990, 1970.
- III-6. D. Forslund, et. al., Bulletin of American Physical Society, 20, 1377, 1975.
- III-7. Sanwal P. Sarraf and Leonard M. Goldman (to be published.)
- III-8. F. Chen, "Introduction to Plasma Physics", Plenum Press, 187, 1976.
- III-9. A.V. Gurevich, et. al., Sov. Phys. JETP 36, 277, 1973.
- III-10. N. Krall and A. Trivelpiece, "Principles of Plasma Physics", P390, McGraw-Hill, 1973.
- III-11. CRC Mathematical Handbook, Edition 51, P54.
- IV-1. John McAdoo, Laboratory for Laser Energetics, Private Comm.
- IV-2. W. Seka, et. al., Applied Optics 19, 409, 1980.
- IV-3. R. Turner, Ph.D. Thesis, University of Rochester, 1980.
- IV-4. E.J. Allen, Rev. Scientific Inst. 42, 1423, 1971.
- IV-5. M. Oron and Y. Paiss, Rev. Scientific Inst. 44, 1293, 1973.
- IV-6. H.J. Karr, Los Alamos Scientific Lab. Report, LAMS 2916, 1963.
- IV-7. D. Slater and F. Mayer, KMS Report U568, 1976.
- IV-8. J.J. Thomson, Philos. Mag.(6) 21, 225, 1911.
- IV-9. S.C. Brown, "Basic Data of Plasma Physics, Chap.3, MIT Press, Cambridge, 1966.

- IV-10. J. Pearlman and M. Matzen, Sandia Laboratories Report, SAND 78-0209, 1978.
- IV-11. C.M. Braams, Nuclear Instruments and Methods 26, 83, 1964.
- IV-12. W. Rogowski, Arch. f. Elektrotechnik, 12, 1, 1923.
- IV-13. K. Spangenberg, Vacuum Tubes, McGraw-Hill, 443, 1948.
- IV-14. Trade Mark of PPG Industries, Bull 45A: SGL Hamolite, 1975.
- IV-15. B. Cartwright, et. al., Nuclear Instruments and Methods 153, 1978.
- IV-16. R. Fleischer, et. al., Nuclear Tracks in Solids, University of California Press, 1975.
- IV-17. G.L. Payne, et. al., J. Appl. Phys. 49(9), 4688, 1978.
- IV-18. M.A. Gusinow, et. al., Appl. Phys. Lett. 33(9), 800, 1978.
- IV-19. M.A. Gusinow, et. al., Sandia Laboratory Report, SAND 78-0336, 1978.
- IV-20. C. Joshi, et. al., Appl. Phys. Lett., 34(10), 625, 1979.
- IV-21. R. Morton, Practical Considerations in Automatic Image Analysis, Analytical Systems Division, Bausch & Lomb, 1979.
- V-1. K. Estabrook and W. Kruer, Phys. Rev. Lett. 40, 42, 1978.
- V-2. D. W. Forslund, et. al., Phys. Rev. Lett. 39, 384, 1977.
- V-3. R. Morse and C. Nielsen, Phys. Fluids 16, 909, 1973.
- V-4. J. S. Pearlman and R. Morse, Phys. Rev. Lett. 40, 1652, 1978.
- V-5. John McAdoo, Laboratory for Laser Energetics, Private Comm.
- V-6. K.A. Bruckner, et. al., Nuclear Fusion 34, 277, 1980.
- V-7. V.P. Silin, Sov. Phys. JETP 21, 1127, 1965.
- V-8. D.G. Colombart and W. Manheimer, NRL Report 4083, Oct. 1979.
- V-9. B.H. Ripin and E.A. Mclean, Appl. Phys. Lett. 34, 11, 1979.
- V-10. I. Pelah, Phys. Lett. 59A(5), 348, 1976.

APPENDIX

A. FORTRAN PROGRAM USED FOR DATA REDUCTION

We present here the listing of the program used for the data reduction. First the raw data is stored in a data file in a manner shown (see listing under data file).

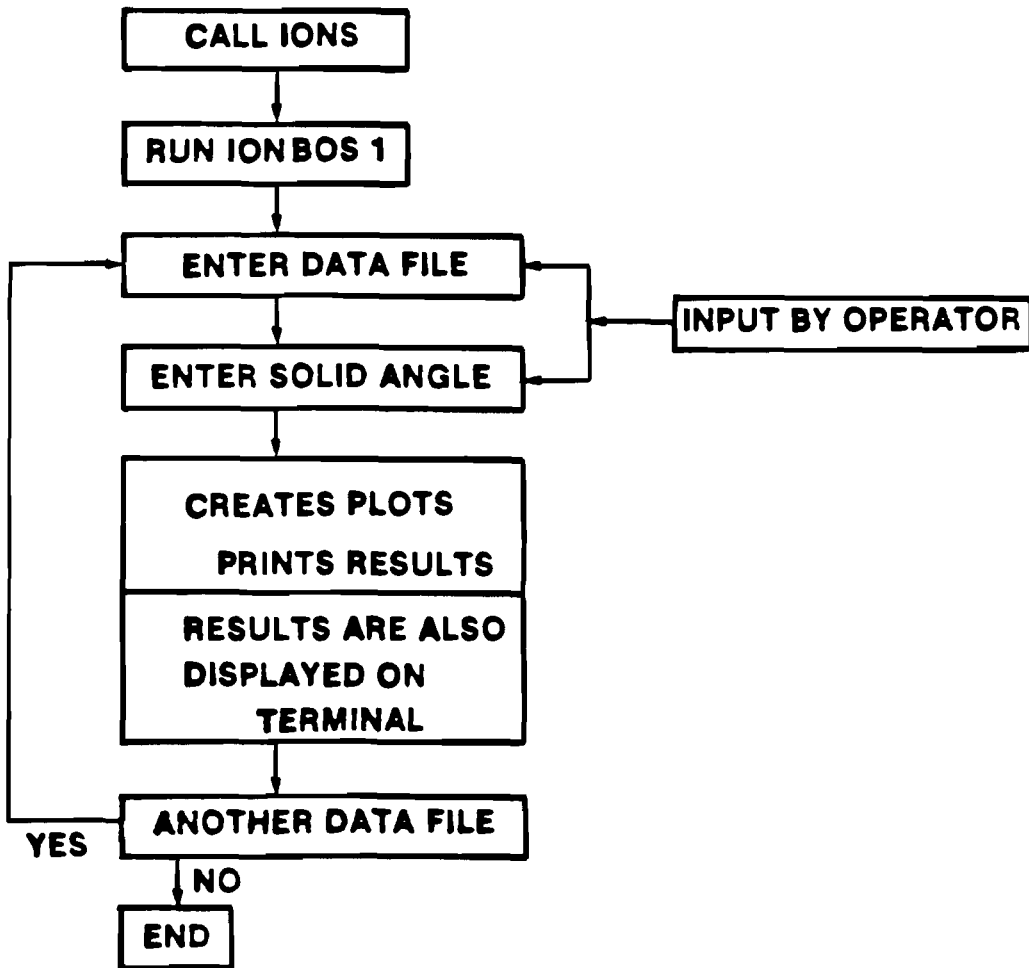
The procedure file 'IONS' is called to execute the data reduction program 'IONBOS1'. During the execution, 'IONBOS1' asks for the data file which is entered by the operator. Operator also enters the effective solid angle ' Ω ' during the execution of the program. This is a correction factor to account for the extent of asymmetry described in Chapter IV.

The program calculates and plots ion density distribution, total energy contained in ions, total number of ions, charge to mass ratio of species etc. as is explained in the listing. For plotting, Cyber 175 library plotting routine 'L PLOT' was used. This may be protected by the Copyright.

The program is written in 'FORTRAN' language for Cyber 175. To execute this program on other type of computers some modifications may be required.

FLOW CHART

UR
LLE



E1044

DATA FILE

C The numbers in the data file are read in sequence separated
C by commas. The format used is the 'General Format' for Cyber
C 175. The file is read from public Tape 5.
C This defines the reference axes.
XX(1),XX(2),YY(1),YY(2)
C Origin point X,Y (Axes origin)
XX(3),YY(3)
C Number of Parabolas
N
C Now the data corresponding to each parabola is entered in sequence
C Number of points in Parabola 1
IP(1)
C X Position, Y Position, # of Counts
X(1,1),Y(1,1),D(1,1)
X(1,2),Y(1,2),D(1,2)
: : :
: : :
C Number of points in Parabola 2
IP(2)
C X Position, Y Position, # of Counts
X(2,1),Y(2,1),D(2,1)
X(2,2),Y(2,2),D(2,2)
: : :
: : :
C This is repeated till all Parabolas are accomodated.

PROCEDURE FILE "IONS"

```
SETTL(1000)
ATTACH, FTNSUBS/UN=LIBRARY.
GET, IONBOS1
ATTACH, IMSLIB/UN=LIBRARY.
ATTACH, UNIPLOT/UN=LIBRARY.
ATTACH, LPLIB/UN=TCHCOO1.
GET, CALPLOT, UNICAL/UN=TCHCOO1.
GET(PGMLIB/UN=TCHCOO1.)
PURGE, NPFILE/NA.
RETURN, NPFILE, TAPE1, PRINT, LGO.
DEFINE, NPFILE.
FTN, I=IONBOS1, OPT=0, L=0.
LDSET, LIB=UNICAL/UNIPLOT/CALPLOT/FTNSUBS/IMSLIB/LPLIB/PGMLIB, PRESET=0.
LGO.
REWIND, TAPE1, PRINT.
COPY, TAPE1, PRINT.
REWIND, TAPE1.
REWIND, OUTPUT.
COPY, OUTPUT, PRINT.
REWIND, OUTPUT, PRINT.
DISPOSE, PRINT=PR.
ATTACH, UNIPOST/UN=LIBRARY.
UNIPOST, D=TEK.
```

PROGRAM "IONBOS1"

```

0001  C      PROGRAM IONBOS1
0002          PROGRAM IONBOS (INPUT,OUTPUT,TAPE5=INPUT,TAPE6,TAPE4,
0003          +TAPE1=OUTPUT)
0004          DIMENSION X(25,200),Y(25,200),D(25,200),Q(10),X1(25,200),
0005          +V(25,200),VV(25,200),V1(25,200),V2(25,200),VTEMP(25,200),
0006          +DFTEMP(200),XX(200),YY(200),DD(200),X3(2),Y3(2),X2(25,200),
0007          +DF(25,200),IP(25),B(50),QQ(25),Q1(25,200),M(10),E2(10),
0008          +E1(25,200),C1(25,200),C(200),T(200),Z(10)
0009          REAL L,MIN,MAX,M
0010          CALL SETUP
0011  C      BOTTOM LINE CALCULATES THE ELECTRIC FIELD
0012          E=244./1.75
0013          Q(1)=1.
0014          WRITE(1,*)"ENTER FILE NAME"
0015          READ(5,10) AFILE
0016  C      10  FORMAT(A6)
0017          THIS PORTION OF THE PROGRAM CALLS DATA FILE AND READS IT.
0018          CALL GETPF (4,AFILE)
0019          READ(4,*) XX(1),XX(2),YY(1),YY(2)
0020          READ(4,*) XX(3),YY(3)
0021          READ(4,*) N
0022          DO I=1,N
0023          READ(4,*) IP(I)
          IPTEMP=IP(I)

```

```

0024      DO 1 J=1,IPTEMP
0025      READ(4,*) X(I,J),Y(I,J),D(I,J)
0026      1  CONTINUE
0027      PHI= ATAN((YY(2)-YY(1))/(XX(2)-XX(1)))
C      THIS PORTION OF THE PROGRAM DOES AXIS TRANSFORMATION
0028      WRITE(1,149) PHI,AFILE
0029      149  FORMAT(F9.3,A6)
0030      DO 2 I=1,N
0031      ITEMP=IP(I)
0032      DO 2 J=1, ITEMP
0033      XTEMP=X(I,J)
0034      X(I,J)=((X(I,J)-XX(3))+(Y(I,J)-YY(3))*TAN(PHI))*COS(PHI)-10.
0035      Y(I,J)=((Y(I,J)-YY(3))-(XTEMP-XX(3))*TAN(PHI))*COS(PHI)-10.
0036      WRITE(1,*) X(I,J),Y(I,J)
0037      2  CONTINUE
0038      WRITE(1,*) "ENTER EFFECTIVE SOLID ANGLE"
0039      READ(5,11) OMEGA
0040      11  FORMAT(F10.5)
0041      ITEMP=IP(1)
C      AVERAGE MAGNETIC FIELD IS CALCULATED BELOW
0042      B1=0.
0042      DO 3 J=1,ITEMP
0043      B(J)=((X(1,J)**2)*150.5/Y(1,J))**.5
0044      B1=B(J)+B1
0045      3  CONTINUE
0046      BAV=B1/ITEMP
0047      DO 33 J=1,ITEMP
0048      WRITE(1,144) B(J),BAV

```

```
0049      144  FORMAT(2F8.3,F8.3,F8.3)
0050      33  CONTINUE
0051      DO 77 I=2,N
C      THIS PORTION OF THE PROGRAM CALCULATES (Z/M)
0052      77  QQ(I)=0.
0053      DO 66 I=2,N
0054      ITEMP=IP(I)
0055      DO 66 J=1,ITEMP
0056      Q1(I,J)=E*1.08*(X(I,J)**2)/(Y(I,J)*(BAV**2))
0057      QQ(I)=Q1(I,J)+QQ(I)
0058      WRITE(1,145) I,J,Q1(I,J)
0059      145  FORMAT(2I3,F9.3)
0060      66  CONTINUE
0061      DO 76 I=2,N
0062      Q(I)=QQ(I)/IP(I)
0063      WRITE(1,148) I,Q(I)
0064      148  FORMAT(I3,F9.3)
0065      76  CONTINUE
0066      C      LINE BELOW ASSIGNS ION MASS
0067      M(1)=16.
0068      M(2)=16.
0069      M(3)=16.
0070      M(4)=16.
0071      M(5)=16.
0072      M(6)=16.
0073      M(7)=12.
0074      M(8)=16.
```

```
C          THIS PORTION OF THE PROGRAM CALCULATES N, dV, dN/dV
0075      222 DO 88 I=1,N
0076          IPTEMP=IP(I)
0077          DO 88 J=1,IPTEMP
0078          V(I,J)=Q(I)*9.225*BAV*1E7/X(I,J)
0079          X1(I,J)=X(I,J)-0.300
0080          X2(I,J)=X(I,J)+0.300
0081          V1(I,J)=Q(I)*9.225*BAV*1E7/X1(I,J)
0082          V2(I,J)=Q(I)*9.225*BAV*1E7/X2(I,J)
0083          VV(I,J)=V1(I,J)-V2(I,J)
0084          DF(I,J)=D(I,J)*OMEGA /((VV(I,J)*3.87E-8)
0085          D(I,J)=D(I,J)*OMEGA/3.87E-8
0086          WRITE(1,146) I,J,V(I,J),DF(I,J),D(I,J)
0087      146 FORMAT(2I3,3E9.3)
0088      88 CONTINUE
C          THIS PORTION OF THE PROGRAM SUMS UP ION ENERGY AND NUMBER
0089      DO 101 I=1,N
0090          DO 101 J=1,200
0091          E2(I)=0.0
0092          DD(J)=0.0
0093          E1(I,J)=0.0
0094      101 CONTINUE
0095          DO 100 I=1,N
0096          DO 100 J=1,ITEMP
0097          ITEMP=IP(I)
0098          DD(I)=D(I,J)+DD(I)
0099      100 CONTINUE
0100          DO 99 I=1,N
```

```
0101      IPTEMP=IP(I)
0102      DO 99 J=1,ITEMP
0103      E1(I,J)=0.5*M(I)*1.67E-27*D(I,J)*1E-4*(V(I,J)**2)
0104      E2(I)=E2(I)+E1(I,J)
0105      99 CONTINUE
0106      DO 98 I=1,N
0107      WRITE(1,246) I,E2(I),DD(I)
0108      246 FORMAT(I3,2E9.3)
0109      98 CONTINUE
C      PROGRAM BELOW DOES THE PLOTTING
0110      X3(1)=1.E+8
0111      X3(2)=4.E+8
0112      Y3(1)=10.
0113      Y3(2)=1.0E+5
0114      CALL LPLOT(1,1,2,X3,Y3,-1,-2,"ION PLOT","VEL CM/SEC,"DN/DV")
0115      DO 6 I=1,N
0116      IPTEMP=IP(I)
0117      DO 22 J=1,IPTEMP
0118      DFTEMP(J)=DF(I,J)
0119      VTEMP(J)=V(I,J)
0120      22 CONTINUE
0121      CALL LPLOT(1,1,-IPTEMP,VTEMP,DFTEMP,1,2,"ION PLOT","VEL CM/SEC,
0122      +"DN/DV")
0123      6 CONTINUE
C      PROGRAM BELOW SUMS UP NUMBER OF IONS IN ALL PARABOLAS
0124      DO 40 I=1,N
0125      IPTEMP=IP(I)
0126      DO 40 J=1,IPTEMP
```

```
0127 C 40 CONTINUE
0128     ION NUMBERS IN ALL PARABOLAS SUMMED WITH SAME VEL. BASE
0129     NN=50.
0129     NN1=NN+1
0130     DO 30 I=1,N
0131     DO 30 K=1,NN1
0132     D(I,K)=0.0
0133     30 CONTINUE
0134     MAX=V(1,1)
0135     DO 18 I=2,N
0136     IF(V(I,1) .GT. MAX) MAX=V(I,1)
0137     18 CONTINUE
0138     DO 12 J=1,200
0139     12 XX(J)=0.0
0140     XX(1)=MAX
0141     MIN=V(1,IP(1))
0142     DO 13 I=3,N
0143     IF(V(I,IP(I)) .LT. MIN) MIN=V(I,IP(I))
0144     13 CONTINUE
0145     XX(NN1)=MIN
0146     DO 14 J=2,NN
0147     XX(J)=(XX(1)*NN-(J-1)+(J-1)*XX(NN1))/NN
0148     14 CONTINUE
0149     DO 15 I=1,N
0150     J=1
0151     K=1
0152     160 IF(V(I,J) .GE. XX(K)) GO TO 170
```

```
0153          K=K+1
0154          GO TO 160
0155      170  J=J+1
0156          IF(J .GT. IP(I)) GO TO 25
0157          IF(V(I,J) .GT. XX(K)) GO TO 170
0158          D(I,K)=DF(I,J-1)+(XX(K)-V(I,J-1))*(DF(I,J)-DF(I,J-1))
0159          +/(V(I,J)-V(I,J-1))
0160      27  K=K+1
0161          IF(K .GT. NN1) GO TO 25
0162          IF(XX(K) .LT. V(I,J)) GO TO 26
0163          D(I,K)=DF(I,J-1)+(XX(K)-V(I,J-1))*(DF(I,J)-DF(I,J-1))
0164          +/(V(I,J)-V(I,J-1))
0165          GO TO 27
0166      26  GO TO 160
0167      25  CONTINUE
0168      15  CONTINUE
0169          DO 16 K=1,NN1
0170      16  DD(K)=0.0
0171          DO 17 K=1,NN1
0172          DO 17 I=1,N
0173          DD(K)=D(I,K)+DD(K)
0174      17  CONTINUE
0175          DO 18 K=1,NN1
0176      18  WRITE(6,147) DD(K),XX(K)
0177      147  FORMAT(2E9.3)
0178          CALL LPLOT(1,1,2,X3,Y3,-1,-2,"ION SUM","VEL CM/SEC","DN/DV")
```

```
0179      CALL LPLOT(1,1,-NN1,XX,DD,1.2,"ION SUM",VEL CM/SEC,"DN/DV")
0180      CALL ENDPLT
0181      STOP
0182      END
```